Atomic-resolution studies of In_2O_3–ZnO compounds on aberration-corrected electron microscopes

Dissertation
zur
Erlangung des Doktorgrades (Dr. rer. nat.)
der
Mathematisch-Naturwissenschaftlichen Fakultät
der
Rheinischen Friedrich-Wilhelms-Universität Bonn

vorgelegt von
Wentao Yu

aus
V. R. China

Bonn, Juli 2009

Tag der Promotion: 23.10.2009

Angefertigt mit Genehmigung der Mathematisch-Naturwissenschaftlichen Fakultät der Rheinischen Friedrich-Wilhelms-Universität Bonn.

1. Gutachter: Prof. Dr. Werner Mader
2. Gutachter: Prof. Dr. Karl Maier

Contents

I. Electron microscopy and interaction of electrons with matter

Chapter 1 Transmission electron microscope

1.1 Introduction

The electron microscope (EM) is a scientific instrument that uses a high-energetic electron beam to examine objects on a very fine scale. The first EM was invented by Ernst Ruska and Max Knoll in 1931 [1]. Early EMs had a resolution somewhat better than that of a light microscope. Through decades of development, the EM has evolved to a complex and powerful instrument. At the end of last century, the resolution in a Conventional Transmission Electron Microscope (CTEM) could reach the Angstrom scale. At the beginning of the 21st century, with the availability of aberration-correctors, e.g. spherical-aberration correctors and monochromators, high spatial resolution at the sub-Angstrom scale was made possible. Fig.1-1 shows an evolution diagram of the microscope resolution over the decades (see reference in fig.1-1).

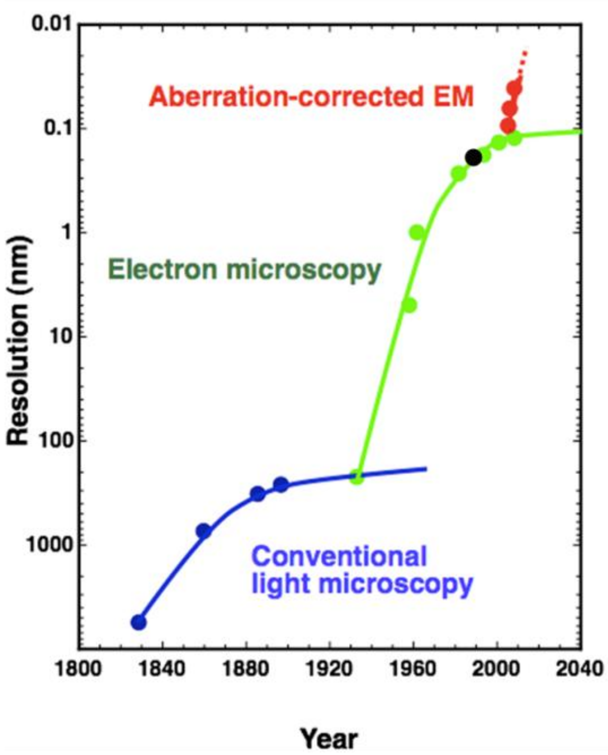

Fig.1-1. Evolution diagram of microscopes in resolution [2].

The curves in blue and in green represent the resolution of light microscopy and of conventional electron microscopy, respectively. The red dots represent the resolution of the electron microscopy with aberration correction. The resolution of the Philips CM300 UT with 1.6 Å is shown as black dot. Nowadays, the transmission electron microscopes have been vital instrument for spectroscopy and measuring atomic structures of solid matter at extremely high spatial and energy resolution.

1.2 Elements of the transmission electron microscope [3]

The principle function of the transmission electron microscope is similar to that of the light microscope. The cross-section of a high resolution (HR) electron microscope of the Philips CM series is shown in fig.1-2. To avoid scattering of the electrons with gas molecules, the microscope column is evacuated. A number of subsystems like cooling system and radiation shields are included. Generally, the transmission electron microscope is composed of five major components: electron gun, illumination system, specimen stage, imaging system and electron detectors.

1.2.1 Electron gun

The function of the electron gun is to provide a steady beam of electrons with constant kinetic energy. There are different types of cathodes based on the thermionic emission (single-crystal LaB_6), (cold) field emission, or Schottky field emission. The emitted electrons are then accelerated through the applied potential by the anode acquiring the determined kinetic energy.

1.2.2 Illumination system

The illumination system is composed of pre-specimen lenses, i.e. a 1st condenser lens and a 2nd condenser lens, tilt coils and condenser apertures. It serves to create an electron beam with defined property: either a nearly plane wave for illuminating a larger specimen area or a convergent beam to achieve a small electron probe. To form an even smaller probe, some electron microscopes are equipped with a 3rd condenser lens.

1.2.3 Specimen stage

In the specimen stage, the specimen is located within the magnetic field of the objective lens. The specimen holder is mounted to manipulate the specimen in five degrees of freedom: specimen position (*x*, *y* and *z*) and specimen tilts (*α* and *β*).

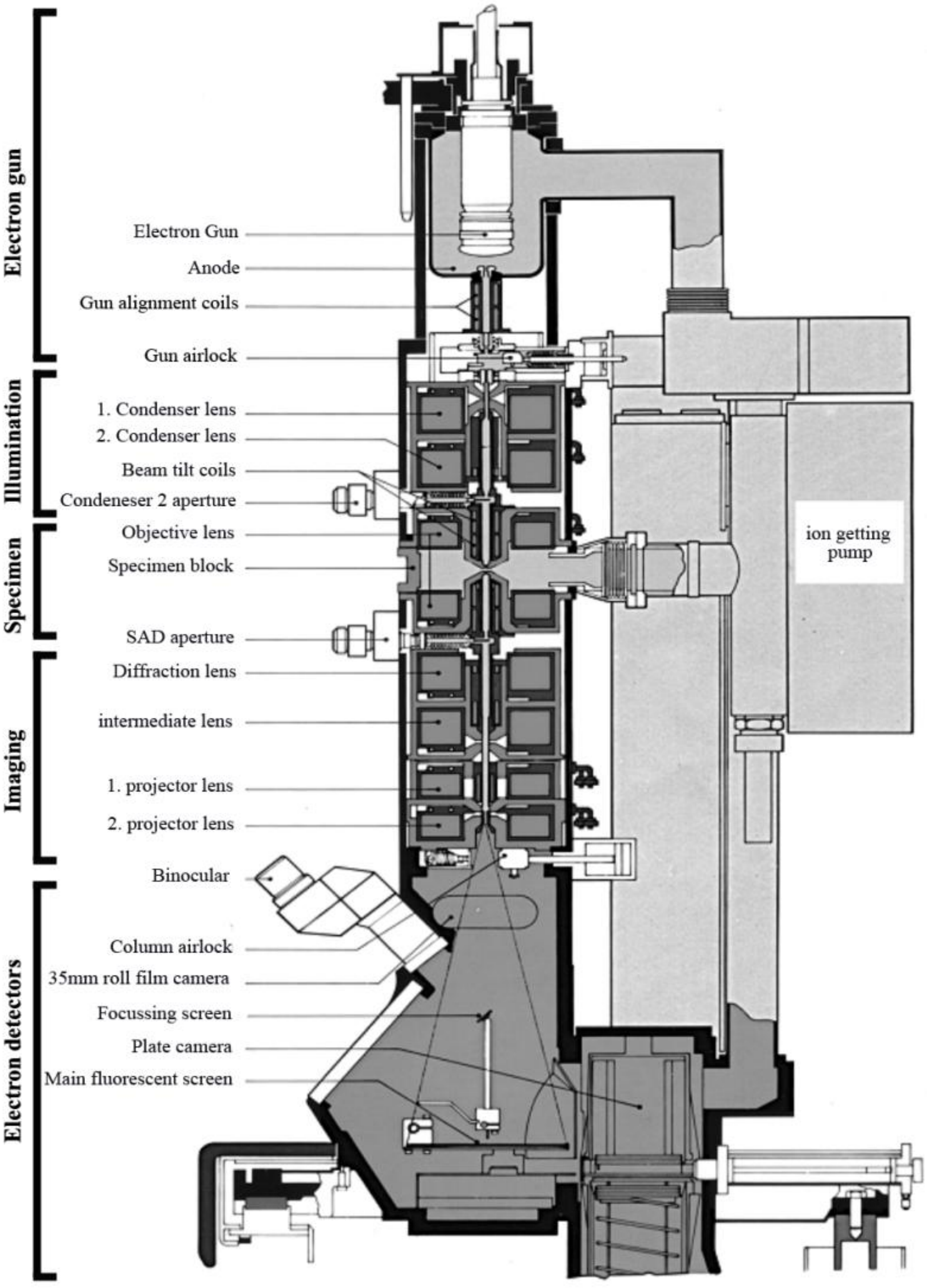

Fig.1-2. Cross-section of high resolution (HR) Philips CM series.

1.2.4 Imaging system

The imaging system is to magnify the electron distribution at the exit plane of the specimen. It is composed of the objective lens, the diffraction lens, the intermediate lens and the projector lens. The function of the objective lens is to bring the diffracted beams to a cross-over in its back focal plane and it is the most important lens among the other lenses of the imaging system, because it has to produce the first magnification step from an electron distribution at Angstrom dimension to an image with ca. 10 nm details. With different excitation of the diffraction lens, either the diffraction pattern or an image can be transferred via the projector lens onto the viewing screen or the detectors.

1.2.5 Electron detectors

Finally, the electron distribution of an image or a diffraction pattern has to be made visible, or to be recorded and stored, which can be achieved with a viewing screen, photographic emulsions or digital detectors such as CCD (Charge-Coupled device) cameras.

1.3 Lens aberrations

Due to imperfections of magnetic lenses and electron sources, aberrations are introduced to the electron wave, thus reducing the spatial resolution of the microscope.
The spherical aberration, defocus, axial astigmatism and chromatic aberration are the most important aberrations for CTEM (fig.1-3).

1.3.1 Spherical aberration (fig.1-3a)

The spherical aberration is caused by the in-homogeneity of the lens field affecting the off-axis rays, which reduces the focal length for electron rays passing the outer zones of the lens. As a result, electrons from a point object **P** crossing the optical axis at different angles is imaged as a disc with a minimum diameter of

$d = 0.5|C_s|(\lambda k_{\max})^3$ in the plane of least confusion and a larger disc in the Gaussian image plane with a diameter of $d_{Gauss} = 2|C_s|(\lambda k_{\max})^3$, with C_s spherical aberration coefficient, λ electron wavelength and $k_{\max}$ highest spatial frequency. The spherical aberration of the objective lens will influence the resolution of the microscope and it is important for the phase contrast imaging, which will be discussed in detail in sec.3.1.

1.3.2 Defocus

Changing the excitation of the objective lens, a point object **P** will be imaged above or below the Gaussian image plane. Fig.1-3b shows the over-focus condition. Changing the setting of the focus will affect the *PCTF* (phase contrast transfer function), see details in sec.3.1.2.

1.3.3 Axial astigmatism

Axial astigmatism occurs due to a non-uniform magnetic field of the lens. The result is that a cone of rays with the same semi-angle from the optic axis will have different foci, depending on the azimuthal angle **φ**, thus forming an ellipse in the Gaussian-image plane, which is shown in fig.1-3c. A circle of the least confusion is formed in the curved mean image plane.

1.3.4 Chromatic aberration

Chromatic aberration is caused by spread of the energy ΔE of the electron source, variations of accelerating voltage ΔV and the lens current ΔI, resulting in a variation of focal length d_c (fig.1-3d), which can be expressed as:

$d_c = C_c\sqrt{\left(\frac{\Delta E}{eV}\right)^2 + \left(\frac{\Delta V}{V}\right)^2 + \left(\frac{2\Delta I}{I}\right)^2}$, with C_c the chromatic aberration coefficient, E, V and I the electron energy, acceleration voltage and lens currents, respectively.

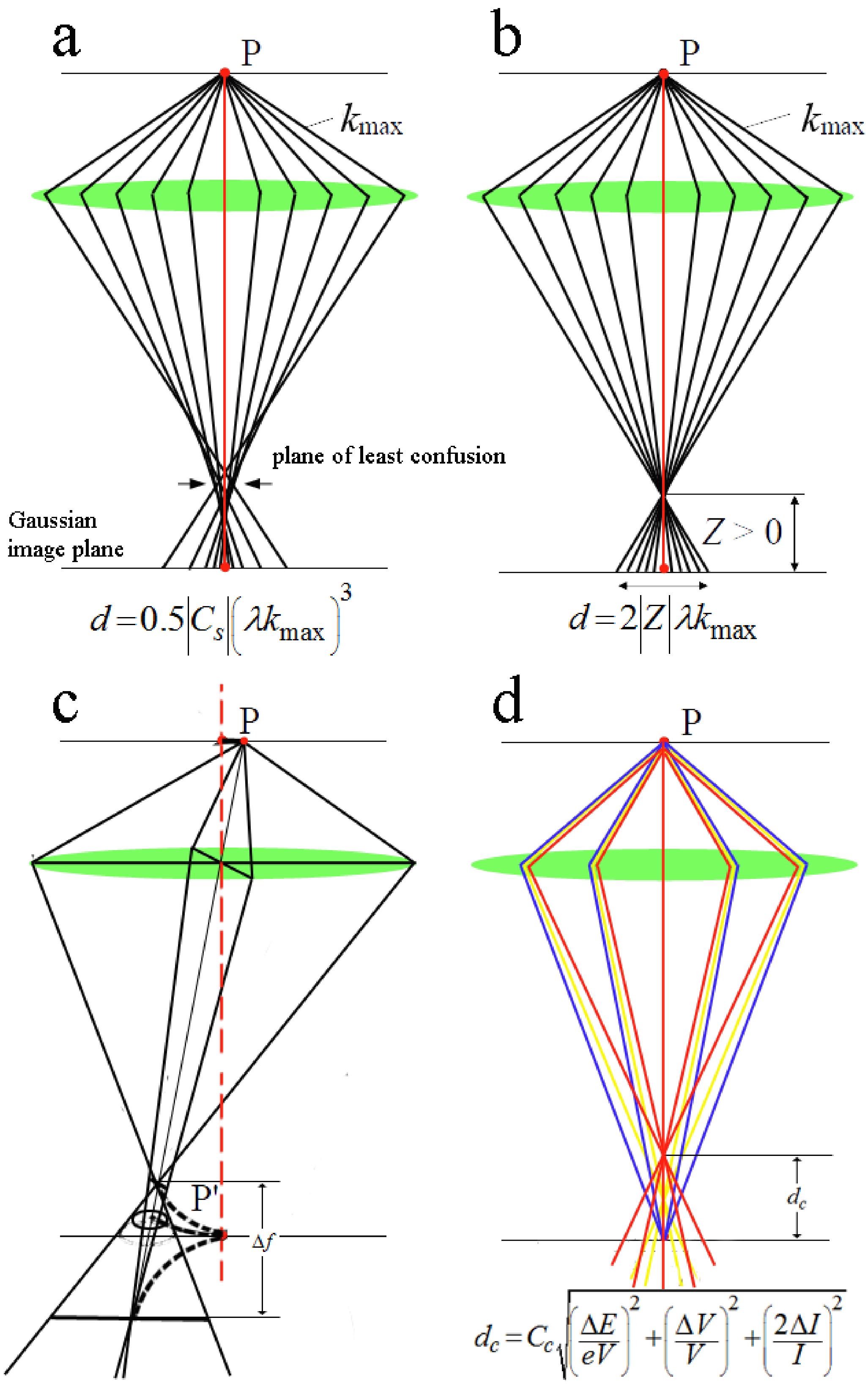

Fig.1-3. Illustration of aberrations: spherical aberration a), defocus b), axial astigmatism c) and chromatic aberration d), respectively.

1.4 Aberration correctors

The spherical aberration is one of the most prominent aberrations in TEM. Scherzer [4] first suggested the correction of the spherical aberration with a combination of quadrupole-octupole electro-magnetic lenses. The C_s corrector was later realized by Rose and coworkers with a design of hexapole E-M lenses [5,6], composed of two hexapole lenses and two transfer round-lens doublets (fig.1-4). It generates an additional spherical aberration with an opposite sign to compensate or eliminate the spherical aberration of the objective lens. Dedicated for STEM, a 2nd generation quadrupole-octupole C_s corrector was achieved by Krivanek et al. in 1999 [7].

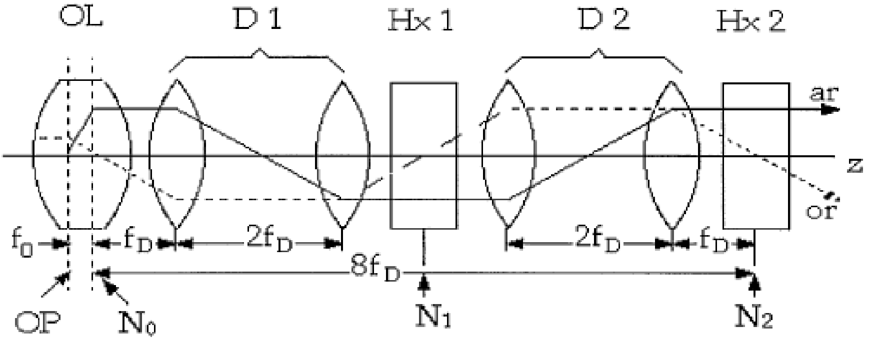

Fig.1-4. Scheme of hexapole type of aberration-corrected objective lens system [6].

Several efforts have been made to reduce the influences of instrumental vibrations and the electro-magnetic field variations of the lens during imaging processes. Moreover, with the usage of the monochromator, the energy spread can be reduced, resulting in an improvement of the coherence of the electron beam. Thus, a better resolution of the electron microscope can be achieved. [8-11].

1.5 Diffraction and imaging mode of CTEM

The electron microscopes can be operated in conventional imaging mode (CTEM) with a resting beam and in scanning (STEM) mode, respectively. The STEM mode will be discussed in chapter 6 in detail. In CTEM, the diffraction pattern is formed in the back focal plane or an image is produced by interference at the first image plane.

In the diffraction mode, the back focal plane of the objective lens acts as the object plane for the diffraction lens. Then the diffraction pattern is magnified and projected onto the viewing screen, by the intermediate and projector lens system (fig.1-5a). From electron diffraction patterns, a variety of information can be extracted: detection of crystalline or amorphous material, crystallographic characteristics (lattice parameters, crystal symmetry), crystal orientation, phase identification, etc.

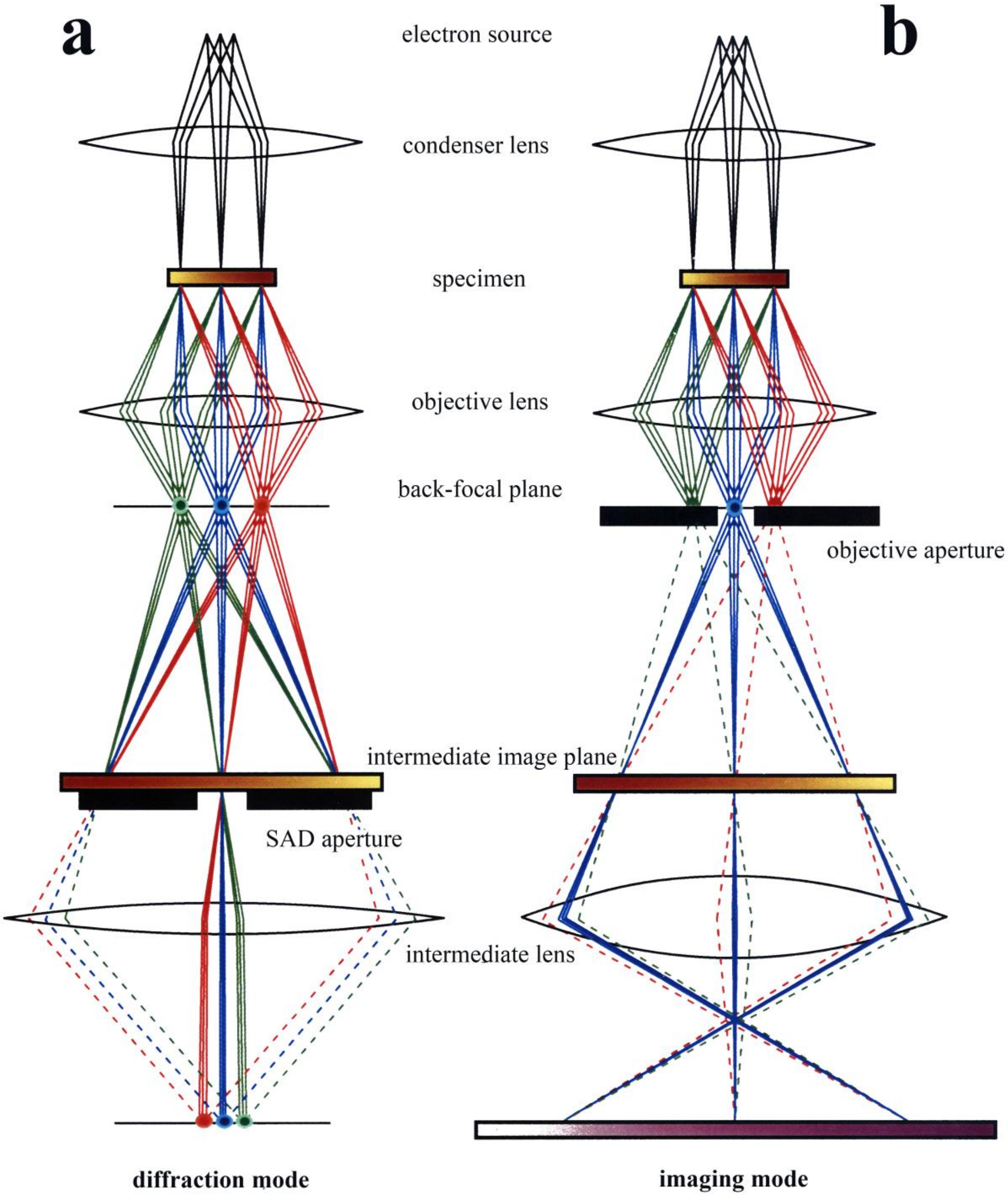

Fig.1-5. Two basic operations of the transmission electron microscope where either the diffraction pattern a) or the image b) is transferred to the viewing screen, respectively [12].

To form an image instead, the strength of the diffraction lens has to be adjusted so that the image plane of the objective lens is the object plane for the diffraction lens. The image of the specimen is then projected onto the viewing screen by the further lens systems (fig.1-5b).

Chapter 2 Kinematic and dynamic theory of electron diffraction

2.1 Kinematic theory of electron diffraction

In the framework of kinematic theory of electron diffraction [13-15], the amplitude $F(K)$ of an electron diffraction pattern results from the superposition of the partial waves scattered at a *N*-atom specimen. The resulting diffracted intensity is composed of the square of the structure factor *F* and the shape factor *G*:

$$I_g \propto \left| \sum_{i=1}^{N} f_i \exp\left[-2\pi i\vec{q}\cdot\left(\vec{r}_n+\vec{r}_k\right)\right]\right|^2 = F\left(\vec{q}\right)^2\cdot G\left(\vec{q}\right)^2. \tag{2.1}$$

- The structure factor is defined as:

  $$F\left(\vec{q}\right)=\sum_k f_k \exp\left[-2\pi i\left(\vec{k}-\vec{k}_0\right)\cdot\vec{r}_k\right].$$

  It is of interest only for the Bragg condition and cannot be altered by small deviations from the geometry of the Bragg condition. Thus,

  $$\begin{aligned} F\left(\vec{q}\right)&=\sum_k f_k \exp\left(-2\pi i\vec{g}\cdot\vec{r}_k\right)\\ &=\sum_k f_k \exp\left[-2\pi i\left(u_k h+v_k k+w_k l\right)\right]=F\left(\vec{g}\right). \end{aligned} \tag{2.2}$$

- The shape factor depends on the deviation vector $\vec{s}$ (small deviations from the exact Bragg condition):

  $$\begin{aligned} G\left(\vec{q}\right)&=\sum_m\sum_n\sum_o \exp\left[-2\pi i\left(\vec{g}+\vec{s}\right)\cdot\vec{r}_n\right]=\sum_m\sum_n\sum_o \exp\left(-2\pi i\vec{s}\cdot\vec{r}_n\right)^{1}\\ &=\left[\frac{\sin\left(\pi s_x M_x a_1\right)}{\pi s_x a_1}\cdot\frac{\sin\left(\pi s_y M_y a_2\right)}{\pi s_y a_2}\cdot\frac{\sin\left(\pi s_z M_z a_3\right)}{\pi s_z a_3}\right], \end{aligned} \tag{2.3}$$

where f_i is the atom form factor for the i^{th} atom, $\vec{r}_n$ lattice vectors, $\vec{r}_k$ base vectors of i^{th} atom in the unit cell; g reciprocal lattice vector; $\vec{s}$ deviation parameter (fig.2-1).

In high-energy electron diffraction, $\vec{s}$ is simply equal to $\vec{s}_z$ and $s_z M_z$ is the crystal thickness *t*. Neglecting the widths of diffracting columns along the transverse direc-

---

[1] : recall that $\vec{g}\cdot\vec{a}_i=n$ (integer) and $\exp\left(-2\pi in\right)=1$.

tions, the intensity for the diffraction can be written as:

$$I_g \propto \left|F(g)\right|^2 \cdot \frac{\sin^2(\pi st)}{(\pi s)^2}. \tag{2.4}$$

The kinematic theory of electron diffraction holds true for $I_g << I_0$ and for large values of $|\vec{s}|$.

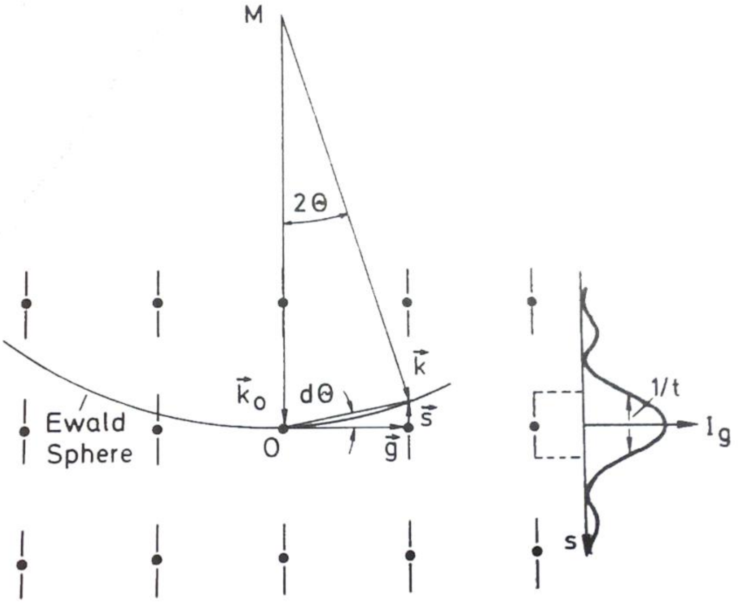

Fig.2-1. An extension of Ewald's 'representation' of electron diffraction, with the definition of vector $\vec{k} = \vec{k}_0 + \vec{g} + \vec{s}$, (adapted from [15] p.275).

2.2 Dynamic theory of electron diffraction

A detailed description for the intensities of the primary and diffracted beams must be based on the dynamical theory of electron diffraction by solving the Schrödinger equation for relativistic high-energy electrons. There are generally two major methods for calculating the exit-plane wave functions, the Bloch wave method and the multislice method.

2.2.1 Bloch wave formalism

The starting point of the Bethe-Bloch formalism [16,17] is the time-independent Schrödinger equation with the wave function $\psi(r)$ and lattice potential $V(r)$:

$$\Delta\psi(r)+\frac{2me}{\hbar^2}\left[E^*+V(r)\right]\psi(r)=0\,, \tag{2.5}$$

where $E^*=E\frac{2E_0+eE}{2(E_0+eE)}$ is the relativistic total energy of the incident electrons and m is the relativistic corrected electron mass $m=m_0\left(1+eE/E_0\right)$.

After expansion of the periodic lattice potential $V(\vec{r})$ in a Fourier series via reciprocal lattice vectors $\vec{h}$, $V(\vec{r})=\sum_h V_h\exp\left(2\pi i\vec{h}\cdot\vec{r}\right)$, the Ansatz for the wave function in eq.2.5 has the general form, known as Bloch wave function:

$$\psi(\vec{r})=C(\vec{r})\exp\left(2\pi i\vec{k}\cdot\vec{r}\right)=\sum_g C_g\exp\left[2\pi i\left(\vec{k}+\vec{g}\right)\cdot\vec{r}\right], \tag{2.6}$$

with constants $C(\vec{r})$ having lattice periodicity, which can be expanded as: $C(\vec{r})=\sum_g C_g\exp\left(2\pi i\vec{g}\cdot\vec{r}\right)$.

Substituting the modified potential $U_h=\frac{2me}{h^2}V_h$ and the wave vector of electrons in the crystal $K^2=\frac{2me}{h^2}\left(E^*+V_0\right)$, eq.2.5 leads to:

$$\sum_g\left\{\left[K^2-\left(\vec{k}+\vec{g}\right)^2\right]C_g+\sum_{h\neq g}U_{g-h}C_h\right\}\exp\left[2\pi i\left(\vec{k}+\vec{g}\right)\cdot\vec{r}\right]=0\,. \tag{2.7}$$

This system of equations must be valid for all position $\vec{r}$ in the crystal and for non-trivial solutions this results in:

$$\left[K^2-\left(\vec{k}+\vec{g}\right)^2\right]C_g+\sum_{h\neq g}U_{g-h}C_h=0\,. \tag{2.8}$$

This set of equations is exact, relating the wave vector K of the Bloch wave to the energy of the incident electrons via $\vec{k}$. The general solution for this wave function $\psi(\vec{r})$ can be described as a linear combination of n Bloch waves with different wave vectors $\vec{k}^{\,j}$.

$$\psi\left(\vec{r}\right)=\sum_{j=1}^{n}\alpha^{j}\psi^{j}\left(\vec{r}\right)=\sum_{j=1}^{n}\alpha^{j}\sum_{g=1}^{n}C_{g}^{j}\exp\left[2\pi i\left(\vec{k}^{j}+\vec{g}\right)\cdot\vec{r}\right]$$
$$=\sum_{g=1}\left[\sum_{j}\alpha^{j}C_{g}^{j}\exp\left(2\pi i\vec{k}^{j}\cdot\vec{r}\right)\right]\exp\left(2\pi i\vec{g}\cdot\vec{r}\right), \tag{2.9}$$

with α^j the excitation amplitude of the j^{th} Bloch wave.

The next step is to calculate the excitation coefficient C_g^j of the j^{th} Bloch waves. Due to the high-energy approximations ($|K|\approx\left|\vec{k}^{j}\right|$ and $|K|>>|\vec{g}|$ and $K\approx\left|\vec{k}+\vec{g}\right|$), eq.2.8 can be re-written in a matrix form:

$$\frac{1}{2K}\begin{pmatrix} -\vec{k}_t^2 & U_{-g} & U_{-h} & \cdots \\ U_g & -\left(\vec{k}_t+\vec{g}\right)^2 & U_{g-h} & \cdots \\ U_h & U_{h-g} & -\left(\vec{k}_t+\vec{h}\right)^2 & \cdots \\ \vdots & \vdots & \vdots & \ddots \end{pmatrix}\begin{pmatrix} C_0^j \\ C_g^j \\ C_h^j \\ \vdots \end{pmatrix}=\left(\vec{k}_z^j-K\right)\begin{pmatrix} C_0^j \\ C_g^j \\ C_h^j \\ \vdots \end{pmatrix}, \tag{2.10}$$

where $\vec{k}^j$ can be divided into two components: $\vec{k}_z^j$ and $\vec{k}_t^j$ (parallel and transverse to the incident electron direction, respectively).

Due to the continuity of the wave function when entering the surface of the crystal, $\psi\left(0\right)$ can be obtained with $\sum_{g}\alpha^{j}C_{0}^{j}=1$ and $C\vec{\alpha}=\vec{u}$ with vector $\vec{u}$ the first component 1 and the rest 0. If Є(t) defines a diagonal matrix $\exp\left(2\pi i k_z^j t\right)\delta_{ij}$, depending on the crystal thickness, with the use of the Bloch wave formalism, it enables the direct calculation of the scattering matrix, thus the wave function for arbitrary crystal thickness:

$$\psi\left(t\right)=C\text{Є}(t)C^{-1}\psi\left(0\right). \tag{2.11}$$

2.2.2 Multi-slice method [18,19]

The multi-slice approach also starts with the Schrödinger equation for the full wave function expression: $\psi_f\left(\vec{r}\right)=\psi\left(\vec{r}\right)\cdot\exp\left(2\pi iz/\lambda\right)$.

Eq.2.5 then becomes $-\frac{\hbar^2}{2m}\left(\nabla_{xy}^2+\frac{\partial^2}{\partial z^2}+\frac{4\pi i}{\lambda}\frac{\partial}{\partial z}+\frac{2meV}{\hbar^2}\right)\psi\left(r\right)=0$ (2.12)

For high-energy electrons, ψ changes slowly with thickness z and the wavelength of the electrons λ is small, therefore:

$$\left|\frac{\partial^2\psi}{\partial z^2}\right| << \left|\frac{1}{\lambda}\frac{\partial\psi}{\partial z}\right|.$$

Neglecting the second derivative with respect to z, eq.2.12 can be written as:

$$\frac{\partial\psi(\vec{r})}{\partial z} = \left[\frac{\lambda i}{4\pi i}\nabla_{xy}^2 + i\sigma V(\vec{r})\right]\psi(\vec{r}), \tag{2.13}$$

with $\sigma = 2\pi me\lambda / h^2$.

The general formal operator solution with an integration over a slice of thickness Δz yields:

$$\begin{aligned}\psi(x,y,z+\Delta z) &= \exp\left[\left(\frac{\lambda i}{4\pi}\Delta z\nabla_{xy}^2 + i\sigma V_{\Delta z}(x,y,z)\right)\right]\psi(x,y,z) + O\left(\Delta z^2\right)\\ &= \exp\left(\frac{\lambda i\Delta z}{4\pi}\nabla_{xy}^2\right)t(x,y,z)\psi(x,y,z) + O\left(\Delta z^2\right),\end{aligned} \tag{2.14}$$

with the projected potential $V_{\Delta z}(x,y,z) = \int\limits_{z}^{z+\Delta z} dz' \cdot V(x,y,z')$, the transmission function $t(x,y,z) = \exp\left[i\sigma V_{\Delta z}(x,y,z)\right]$ and the error term $O\left(\Delta z^2\right)$, which can be neglected later. The transmission function at depth z acts as a phase shift of the wave function due to the projected potential.

The term $\exp\left(\frac{\lambda i\Delta z}{4\pi}\nabla_{xy}^2\right)$ is the Fresnel propagator function, which acts as a 2D convolution in real space for a distance Δz: $\exp\left(\frac{\lambda i\Delta z}{4\pi}\nabla_{xy}^2\right) = p(x,y,\Delta z)\otimes$, (2.15)

with $p(x,y,\Delta z) = FT^{-1}\left[P(k,\Delta z)\right] = \frac{1}{i\lambda\Delta z}\exp\left[\frac{i\pi}{\lambda\Delta z}\left(x^2+y^2\right)\right]$.

For the multi-slice calculation of the exit-plane wave function, the specimen is first divided into thin slices. If the initial value of the electron wave function at the entrance of the specimen is given, the electron wave function experiences a phase shift from the scattering at the projected potential, which is trivial and propagates then along z for slice thickness Δz_n. Finally, the wave function at slice *n+1* is calculated from the function at slice *n* by:

$$\psi_{n+1}(x,y) = p_n(x,y,\Delta z_n) \otimes \left[t_n(x,y)\psi_n(x,y)\right] + O\left(\Delta z^2\right). \tag{2.16}$$

Thus, the wave function at any depth *z* in the specimen can be calculated, provided the potential inside the specimen is known.

2.2.3 Dynamic calculation with absorption and specimen or beam tilt

High-energy electrons interact with the specimen either in-elastically or elastically, resulting in scattering into high angles, which will be retained by an aperture of the microscope. Such processes cause a decrease of electron intensity. To treat the absorption semi-quantitatively, a complex lattice potential is taken into account:
$V_p \Rightarrow V_p + iV_p'$.

The absorption potential V_p' may be approximately by $V_p' = \alpha V_p$, with a constant factor α, usually being between 0.1 and 0.05, depending on the element under consideration.

In the TEM experiment, small tilt of the specimen off the low-order zone axis or beam tilt off the optical axis may exist. The specimen tilt is not the same as a beam tilt, because the beam direction has a strong interaction with the aberrations of the objective lens.

- small specimen tilts in the multi-slice calculation can be taken into account by a shift of the wave function between slices and propagator function can then be modified: $\tilde{p}\left(\vec{k},\Delta z\right) = \exp\left[-2\pi i \Delta z\left(\frac{1}{2}\lambda \vec{k}^2 + \vec{k}\cdot\vec{\tau}\right)\right]$, (2.17)

  with specimen tilts $\vec{\tau} = \left(\vec{\tau}_x, \vec{\tau}_y\right)$. Only small tilts of the specimen (<1 degree) are valid [20].
- For situations with beam tilts, the multi-slice formula was discussed in detail by Ishizuka [21] and Chen et al. [22], based on the integral form of the Schrödinger equation, together with the modifications of the propagator and phase-grating functions.
- For dealing with large beam tilts condition (e.g. STEM mode for HAADF imaging), the alternative is generation of a 3*D* lattice potential and the slices are cho-

sen always perpendicular to the incident beam direction. Thus, a modification of the propagator function is not needed [23].

Chapter 3 Wave-optical theory of imaging

3.1 Contrast transfer theory

3.1.1 PCTF and delocalization

The function of an objective lens can be described as a contrast-transfer function, independent of the specimen structure. The image intensity consists of contributions of CTF for amplitude and phase structures, however, only the *PCTF* (CTF for phase structures) is more important, which can be written as:

$$PCTF = \sin\left[2\pi\chi(k)\right] = \sin\left[2\pi\left(\frac{1}{2}Z\lambda k^2 + \frac{1}{4}Cs\lambda^3 k^4\right)\right] \tag{3.1}$$

with $\chi(k) = 0.5Z\lambda k^2 + 0.25Cs\lambda^3 k^4$ aberration function.

The *PCTF* is modulated by three parameters: the wavelength λ of the incident electrons, the defocus *Z* and the spherical aberration coefficient *Cs*, respectively. A plot of the *PCTF* with spatial frequencies is shown in fig.3-2. The wide region with virtually constant phase change in the transfer function is denoted as 'passband'.

The delocalization of a point in the image is given by the relation:

$$R(k) = \max\left|\nabla\chi(k)\right| = \max\left|Z\lambda k + Cs\lambda^3 k^3\right| \text{ with } k \in \left[0, k_{\max}\right]. \tag{3.2}$$

3.1.2 Conventional settings of defocus of the objective lens

In TEM with electrons of a wavelength λ and a fixed spherical aberration coefficient *Cs*, three settings of defocus Z are important for the modes of *PCTF*.

- **Scherzer defocus [**24**]:** $Z_{Sch} = -\left(\frac{4}{3}Cs\lambda\right)^{1/2}$ (Appendix A)
- **Lichte defocus [**25,26**]:** $Z_{Lichte} = -0.75Cs\lambda^2 k_{\max}^2$ (Appendix B).
- **Minimum phase-contrast defocus [**27,28**]:** $Z_{\min} = -\left(1/4\, Cs\lambda\right)^{1/2}$

At **Scherzer defocus**, the widest passband exists and ranges almost constant at low spatial frequencies to a maximum spatial frequency, given by $k_{Sch} = \left(\frac{3}{16}Cs\lambda^3\right)^{-1/4}$, however, at a cost of the point resolution lower than the information limit $k_{\max}$, which is the highest spatial frequency that can be transferred by the electron microscope. The point resolution is defined by the k value with 10% phase contrast in the Scherzer passband.

At **Lichte defocus** of least confusion, there is the smallest contrast delocalization, given by $R_{Lichte,\min} = \frac{1}{4}Cs\lambda^3k_{\max}^3$, accompanied with rapid oscillations of *PCTF* at medium spatial frequencies, making the images difficult to interpret.

At **Minimum phase-contrast defocus**, also known as the maximum amplitude-contrast defocus, the amplitude of contrast is maximized up to a spatial frequency, given by $k_{\min} = \left(Cs\lambda^3\right)^{-1/4}$. However, the defocus aberration and the spherical aberration do not cancel properly at higher spatial frequencies, well below the point resolution.

3.1.3 Dark-atom and bright-atom contrast conditions [29,30]

The new generation of TEM instrument offers a new degree of freedom with the adjustable spherical aberration of the objective lens.

With the reduction of the spherical aberration coefficient, the point resolution k_{Sch} at the Scherzer defocus can be extended up to the information limit k_{max}, however, at the cost of contrast delocalization.

For a 300 keV microscope with an information limit $k_{max} = 12.5\ \mathrm{nm}^{-1}$, fig.3-1a and fig.3-1b are simulated contour plots of the amount of phase contrast and the delocalization versus spherical aberration and defocus, respectively. Three defocus conditions are indicated by the dashed curves. The curve for Scherzer defocus condition sits at the ridge of the integrated *PCTF* contour, while the minimum delocalization contour follows the Lichte defocus condition of least confusion.

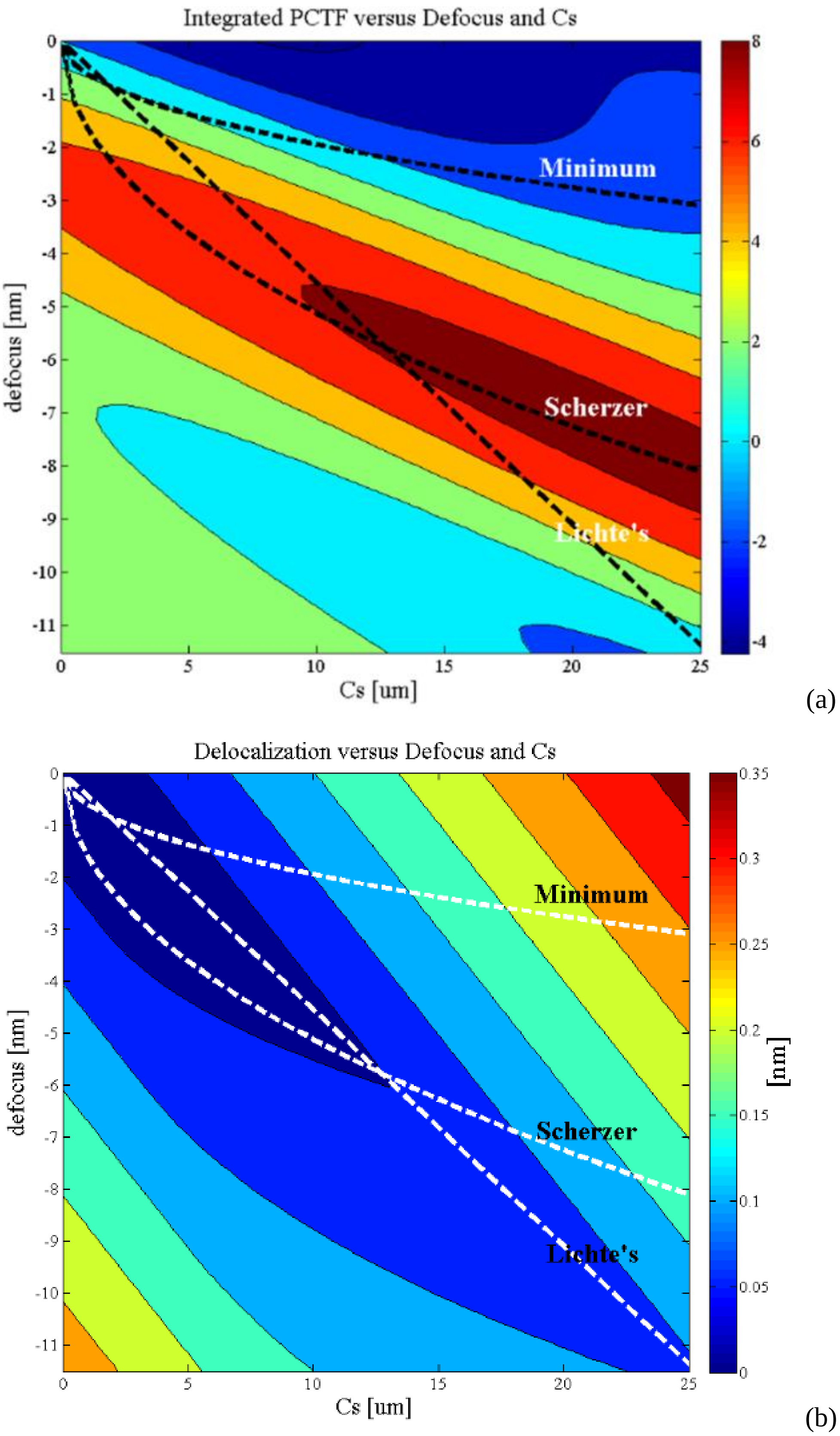

Fig.3-1. Contour plots of the amount of phase contrast (a) and the delocalization (b) versus spherical aberration coefficient *Cs* and defocus *Z*.

The modulation of the phase contrast by defocus and spherical aberration is always accompanied by introducing a delocalization. In principle, there doesn't exist an optimum condition with both maximum phase contrast and minimum delocalization at the same time. A good compromise might be equating the Scherzer defocus and the Lichte defocus, thus the C_s and defocus Z yield: $C_{S,opt} = \frac{64}{27}\frac{1}{\lambda^3 k_{\max}^4}$ and $Z_{opt} = -\frac{16}{9}\frac{1}{\lambda k_{\max}^2}$, respectively.

The delocalization is then given by: $R_{opt} = \frac{16}{27} k_{\max}^{-1}$. Such setting with the combined positive C_s and negative defocus Z is nominated as the optimum defocus condition at 'dark-atom' contrast.

By choosing a negative spherical aberration coefficient $C_{S,opt} = -\frac{64}{27}\frac{1}{\lambda^3 k_{\max}^4}$ and an over-focus $Z_{opt} = \frac{16}{9}\frac{1}{\lambda k_{\max}^2}$, the *PCTF* is now positive up to the information limit g_{max} (fig.3-3). The delocalization *R*, given by $R_{opt} = \frac{16}{27} k_{\max}^{-1}$, remains the same as that for the positive setting of *Cs*. Such setting of the combined *Cs* and *Z* is known as the 'bright-atom' contrast condition.

3.2 Image formation theory

3.2.1 Weak phase object approximation (WPOA) in BF-TEM

If the specimen is thin enough, the interaction with the specimen can be described with a transmission function *t*(*x*). In the WPOA [31,32], the main effect of the specimen is to produce spatially varying phase shift to the electron wave as it passes through the specimen. The transmission function can then be expanded to the first order of $v_z(x)$:

$$t(x) \sim \exp\left[i\sigma_e v_z(x)\right] \approx 1 + i\sigma_e v_z(x) + \cdots, \tag{3.4}$$

with $v_z(x)$ the projected atomic potential of the specimen and σ_e a scaling factor.

In the Fourier space, the recorded image intensity with a linear image approximation is: $I(k) = FT\left\{1 + 2\sigma_e v_z(x) \otimes h_{wp}(x) + \mathrm{O}\left(v_z^2\right)\right\} \approx \delta(k) + 2\sigma_e V_z(k) H_{WP}(k)$, (3.5)

with $V_z(k)$ the projected atomic potential and $H_{WP}(k)$ the transfer function in Fourier space.

3.2.2 Image formation theory

A detailed expression for the Fourier transform of the image intensity was given by Ishizuka [33]:

$$I\left(\vec{k};Z\right) = \int T\left(\vec{k}' + \vec{k}, \vec{k}'; Z\right) F\left(\vec{k}' + \vec{k}\right) F^*\left(\vec{k}'\right) d\vec{k}', \tag{3.6}$$

with $F\left(\vec{k}\right) = \int \hat{o}(\vec{r}) \exp\left\{2\pi i \vec{k} \cdot \vec{r}\right\} d\vec{r}$ the Fourier transform of the object transmission function $\hat{o}(\vec{r})$; $T\left(\vec{k}' + \vec{k}, \vec{k}'; Z\right)$ the transmission cross-coefficient, indicating the interference of the transmitted and diffracted beams, given by:

$$T\left(\vec{k}' + \vec{k}, \vec{k}'; Z\right) = \iint s\left(\vec{k}\right) f(Z) t\left(\vec{k} + \vec{k}''; Z + Z'\right) \times t^*\left(\vec{k} + \vec{k}'; Z + Z'\right) d\vec{k} dZ, \tag{3.7}$$

with $s\left(\vec{k}\right)$ normalized intensity distribution of the effective source;

$f\left(\vec{k}\right)$ normalized chromatic defocus spread;

$t\left(\vec{k};Z\right)$ pupil function of objective lens: $t\left(\vec{k};Z\right) = a\left(\vec{k}\right) \exp\left\{-2\pi i \chi\left(\vec{k};Z\right)\right\}$,

where $a(k)$ the aperture function $a\left(\vec{k}\right) = \begin{cases} 1 & \left|\vec{k}\right| \le k_0 \\ 0 & \left|\vec{k}\right| > k_0 \end{cases}$

In the WPOA, the object transmission function $\hat{o}(r)$ and its Fourier transform are given by: $\hat{o}(\vec{r}) = 1 + o(\vec{r})$ and $F\left(\vec{k}\right) = \delta\left(\vec{k}\right) + O\left(\vec{k}\right)$, respectively.

Finally, the Fourier transform of the image intensity is composed of three terms:

$$I\left(\vec{k};Z\right) = I_0\left(\vec{k};Z\right) + I_1\left(\vec{k};Z\right) + I_2\left(\vec{k};Z\right), \tag{3.8}$$

with $I_0\left(\vec{k};Z\right) = T\left(\vec{k},0;Z\right)\delta\left(\vec{k}\right)$, (3.9)

$$I_1\left(\vec{k};Z\right) = T\left(\vec{k},0;Z\right) O\left(\vec{k}\right) + T^*(\vec{k},0;Z) O^*\left(-\vec{k}\right), \tag{3.10}$$

$$I_2\left(\vec{k};Z\right)=\int T\left(\vec{k}'+\vec{k},\vec{k}';Z\right)O\left(\vec{k}'+\vec{k}\right)O^*\left(\vec{k}'\right)d\vec{k}'. \tag{3.11}$$

- $I_0\left(\vec{k};Z\right)$ describes the contribution of the mean image intensity.
- $I_1\left(\vec{k};Z\right)$ describes the contribution of the interference of the transmitted beam with the diffracted ones.
- $I_2\left(\vec{k};Z\right)$ describes the contribution of the interference between the diffracted beams.

The explicit forms of the normalized chromatic defocus spread $f\left(\vec{k}\right)$ and the normalized intensity distribution of the effective source $s\left(\vec{k}\right)$ can be represented by the normalized *1D* and *2D* Gaussians by considering the partial coherence. If the aperture size is much larger than that of the source, the aberration function $\chi\left(\vec{k};Z\right)$ can be expanded in terms of $\vec{k}$ and Z around $\vec{k}'$, $\vec{k}''$ and Z', respectively. Then, a general form of the transmission cross-coefficient can be directly divided into the coherent part and the partial coherent part (Appendix C):

$$T\left(\vec{k}'+\vec{k},\vec{k}';Z\right)=\underbrace{a\left(\vec{k}''\right)a\left(\vec{k}'\right)\exp\left\{-2\pi i\left[\chi\left(\vec{k}'',Z\right)-\chi\left(\vec{k}',Z\right)\right]\right\}}_{coherent}\cdot$$
$$\underbrace{P\left(\vec{k}'',\vec{k}',Z\right)\cdot E_s\left(\vec{k}'',\vec{k}',Z\right)\cdot E_f\left(\vec{k}'',\vec{k}'\right)\cdot E_x\left(\vec{k}'',\vec{k}'\right)}_{partally\quad coherent}, \tag{3.12}$$

with $P\left(\vec{k}'',\vec{k}',Z\right)$ phase factor; $E_s\left(\vec{k}'',\vec{k}',Z\right)$ envelope function of the partial spatial coherence; $E_f\left(\vec{k}'',\vec{k}'\right)$ envelope function of the partial temporal coherence; $E_x\left(\vec{k}'',\vec{k}'\right)$ cross-term envelope function.

The envelope function $E_s\left(\vec{k}'',\vec{k}',Z\right)$ describes the partially spatial coherence of the electron source. The envelope function $E_f\left(\vec{k}'',\vec{k}'\right)$ describes the partially temporal coherence. Both envelopes cause a damping of the contrast transfer.

3.2.3 Linear image approximation

In the linear image formation approximation, only the interference of diffracted beams *k* with the transmitted beam is considered. The phase factor $P\left(\vec{k}'',\vec{k}',Z\right)$ and cross-term envelope function $E_x\left(\vec{k}'',\vec{k}'\right)$ are usually close to 1 and can be neglected. The envelope functions of the partially spatial coherence $E_s\left(\vec{k}'',\vec{k}',Z\right)$ and the partially temporal coherence $E_f\left(\vec{k}'',\vec{k}'\right)$ are then given by

$$E_s\left(\vec{k}'',\vec{k}',Z\right)=E_s\left(\vec{k},Z\right)=\exp\left[-\left(\pi q_0\right)^2\left[\left(C_s\lambda^2k^2-Z\right)\lambda\vec{k}\right]^2/u\right], \tag{3.13}$$

$$E_f\left(\vec{k}'',\vec{k}'\right)=E_f\left(\vec{k}\right)=\exp\left[-\left(\pi\lambda\Delta/2\right)^2k^4/u\right], \tag{3.14}$$

with $u=1+\left(\pi\lambda q_0\Delta\right)^2k^2$, q_0 and Δ the *1/e* half-width values of the source spread and the defocus spread functions [34,35] by the normalized 1*D* and 2*D* Gaussians, respectively.

The damping of **spatial coherence envelope** $E_s\left(\vec{k},Z\right)$ depends on the source spread q_0 and the gradient of the aberration function $\partial\chi\left(\vec{k},Z\right)/\partial\vec{k}$. It attenuates the transfer of information where the *PCTF* oscillates rapidly.

The damping of **temporal coherence envelope** $E_f\left(\vec{k}\right)$ depends on the defocus spread Δ and the spatial frequencies *k*. It dominates the damping of contrast transfer at higher spatial frequencies and limits the information limit of the microscope.

Ignoring the mean image intensity $I_0\left(\vec{k};Z\right)$, the image intensity is then given by

$$I\left(\vec{k};Z\right)\approx I_1\left(\vec{k};Z\right)=\phi\left(\vec{k}\right)\cdot\left\{\sin\left[2\pi\cdot\chi\left(\vec{k},Z\right)\right]E_s\left(\vec{k},Z\right)E_f\left(\vec{k}\right)\right\}, \tag{3.15}$$

with $\phi\left(\vec{k}\right)=2\sigma_eV_z\left(\vec{k}\right)$.

Thus, the transfer function (second term of eq.3.15 on the right-side; also referred as effective *PCTF* yields:

$$PCTF_{eff}=\sin\left[2\pi\cdot\chi\left(\vec{k}\right)\right]E_s\left(\vec{k},Z\right)E_f\left(\vec{k}\right). \tag{3.16}$$

The *PCTF*, envelope functions $E_s\left(\vec{k},Z\right)$ and $E_f\left(\vec{k}\right)$ and $PCTF_{eff}$ at Scherzer defocus condition are shown in fig.3-2, with the parameters of the Philips CM300 UT. At Scherzer defocus condition, the *PCTF* shows a wide passband and starts to oscillate at higher spatial frequencies, where both envelope functions $E_s\left(\vec{k},Z\right)$ and $E_f\left(\vec{k}\right)$ exhibit a damping.

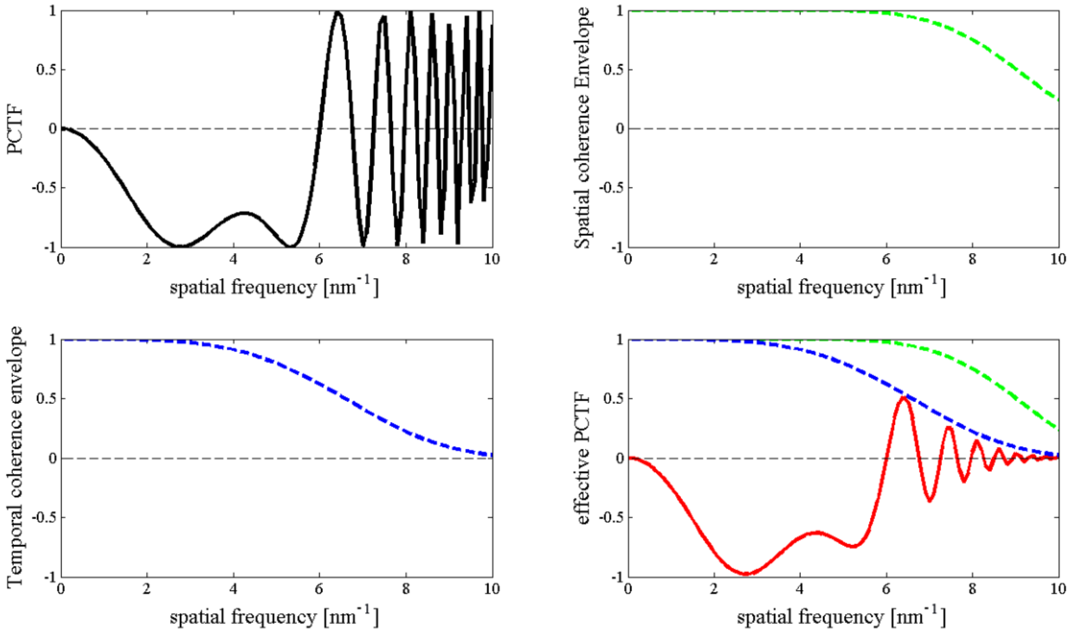

Fig.3-2. *PCTF*, envelope functions of spatial coherence $E_s\left(\vec{k},Z\right)$ and temporal coherence $E_f\left(\vec{k}\right)$, and effective *PCTF* of Philips CM300UT with Cs = 0.6 mm, Z = -42 nm, $\theta_c = 0.2\text{mrad}$, $\lambda = 1.97\text{pm}$, $\Delta = 6.2\text{nm}$ (obtained with the information limit of the object by $d_i = \left(\pi^2\Delta^2\lambda^2/8\right)^{1/4}$) and k_{max} = 6.5 nm^{-1}.

Similarly, the envelope functions for the image-side aberration corrected FEI Titan 80-300 electron microscopes at 'bright-atom' contrast condition are shown in fig.3-3. The envelope function *PCTF* shows an extended point resolution and more smoothened feature than that of the Philips CM300 UT over a large range of spatial frequencies. Especially at higher spatial frequencies (up to 15 nm^{-1}), no oscillation of *PCTF* is observed. Due to the reduced focus spread, the spatial coherence envelope $E_s\left(\vec{k},Z\right)$ remains nearly constant (≈ 1) and it does not affect the $PCTF_{eff}$. The $PCTF_{eff}$ is mainly modulated by the temporal coherence envelope $E_f\left(\vec{k}\right)$ at higher spatial frequencies.

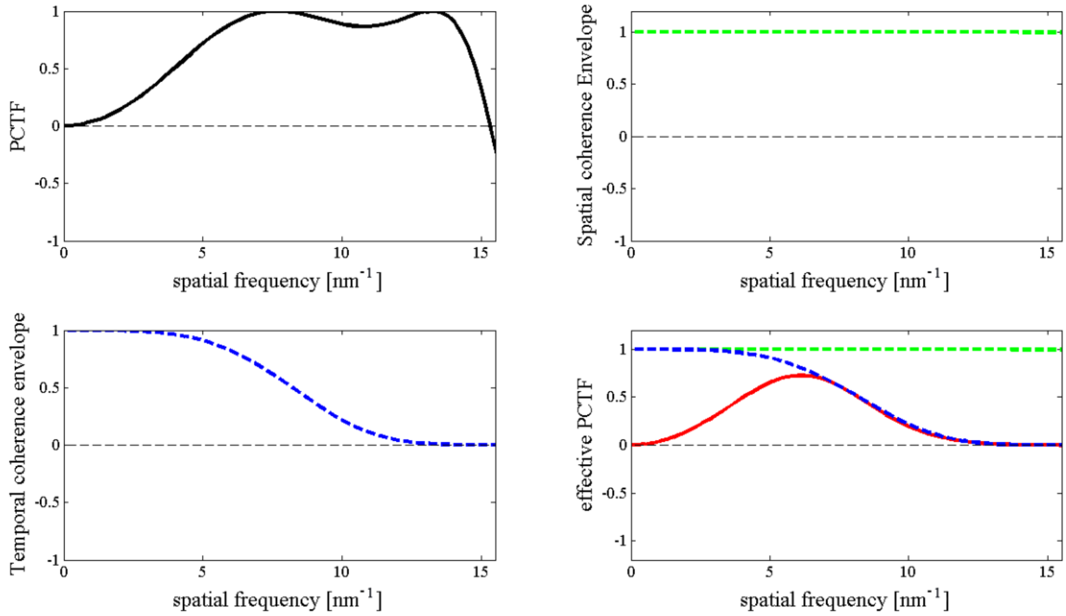

Fig.3-3. *PCTF*, envelope functions of spatial coherence $E_s(\vec{k},Z)$ and temporal coherence $E_f(\vec{k})$, and effective *PCTF* according to the parameters of FEI Titan80-300 image-side aberration corrected electron microscope with Cs = -12.7 µm, Z = 5.7 nm, $\theta_c = 0.2\text{mrad}$, $\lambda = 1.97\text{pm}$, $\Delta \approx 3.5\text{nm}$ and k_{max} = 12.5 nm^{-1}.

3.2.4 Non-linear image formation

The non-linear image formation includes the interference of the diffracted beams, which take three envelope functions ($E_s(\vec{k}'',\vec{k}',Z)$, $E_f(\vec{k}'',\vec{k}')$ and $E_x(\vec{k}'',\vec{k}')$) and one phase factor $P(\vec{k}'',\vec{k}',Z)$ into account.

From the linear image approximation (sec.3.2.3), both positive and negative C_s settings of the optimum defocus conditions are nearly ‘equivalent’: the same point resolution extending to the information limit and the same amount of reduced contrast delocalization. However, from the view of the full non-linear image theory, which also includes the interference terms between the diffracted beams, the ‘dark-atom’ and ‘bright-atom’ contrast conditions are then different. Using the *WPOA*, the image intensities can be roughly written as [36]:

$$I(\vec{r}) \approx 1 \mp 2\pi\lambda U(\vec{r})t + \left(\pi\lambda U(\vec{r})t\right)^2, \tag{3.17}$$

with ‘-’ sign for the setting of positive C_S and ‘+’ sign for the negative C_S; thickness t and projected potential $U\left(\vec{r}\right)$. The setting of ‘bright-atom’ contrast with negative C_S value yields a higher image contrast than that with positive C_S.

For crystalline specimens, the integration of the transmission function in Fourier space reduces to a summation of Bragg reflections $\vec{k}_j$:

$$I\left(\vec{k};Z\right)=\sum T\left(\vec{k}+\vec{k}_j,\vec{k}_j;Z\right)F\left(\vec{k}+\vec{k}_j\right)F^*\left(\vec{k}_j\right)=I_0\left(\vec{k};Z\right)+I_1\left(\vec{k};Z\right)+I_2\left(\vec{k};Z\right), \quad (3.18)$$

with $I_0\left(\vec{k};Z\right)$ and $I_1\left(\vec{k};Z\right)$ defined by eq.3.9 and eq.3.10, respectively; and

$$I_2\left(\vec{k};Z\right)=\sum T\left(\vec{k}+\vec{k}_j;Z\right)O\left(\vec{k}+\vec{k}_j\right)O\left(\vec{k}_j\right). \quad (3.19)$$

3.3 2*D* displacement field and strain measurements

By measuring the local displacement field and hence the strain from HRTEM images at atomic resolution, the structural properties of materials can be revealed, such as lattice translations, dislocations and rotations. However, the positions of the lattice fringes in the HR-TEM image do not necessarily correspond to the actual atom positions, which can be affected by many influences: the crystal structures, specimen thickness, crystal orientations, illumination conditions and so on. To determine the actual atom positions, it normally needs dedicated image simulations in comparison with the experimental HRTEM images. Equipped with the aberration correctors, the resolution of the microscope is much improved. The image contrast can be peaked at atom column positions with moderate delocalization at the ‘bright-atom’ contrast condition. Thus, the local displacement fields and the strain fields can be directly analyzed from atomic resolution TEM images without image simulations.

In general, there are two kinds of methods for analyzing atom column positions, and thus the local displacement fields and the strain fields: the ‘peak-finding’ method in real space [37] and the Geometric phase-image analysis (GPA) in Fourier space [38]. Recently, additional algorithm in real space called the ‘Peak Pairs Analysis’ was introduced by Galindo [39].

3.3.1 ‘Peak-finding’ method

To enhance signal to noise ratio, noise reduction to HRTEM images is necessary. The noise-reduced images present smoothened features around the peaks, which can improve detection precision of the intensity maxima. Several algorithms for the image filtering are available, such as Bragg filtering, low-pass filter and Wiener filters. A Wiener type filter was integrated in the Digital Analysis of Lattice Images (DALI) algorithm by the estimation of the local noise level in the FFT image before maximum localization [37,40].

Normally, the image contrast of atom columns is recorded over more than one pixel. The contrast maxima of the atom columns can be determined, hence, the peaks can be located. With two chosen base vectors, $\vec{x}_1$ and $\vec{x}_2$, metal atom columns are assigned with coordinates. A 2D reference region should be defined, which is assumed to contain no lattice distortion. Subsequently, the 2D displacement field $\vec{u}\left(u_1, u_2\right)$ is measured as differences between positions of local atom columns $\vec{r}\left(x_1, x_2\right)$ and the extrapolation of the chosen reference lattice $\vec{r}_0\left(x_1^0, x_2^0\right)$. The ‘peak-finding’ method has already been used successfully to analyze materials containing epitaxial strain layers and of semiconductors [41-44].

3.3.2 Geometric phase analysis (GPA)

The GPA makes use of the spatial frequency components for analyzing the lattice variations of HR-TEM images [38,45]. Because the variations in lattice spacing are of interest, only the relative lattice spacing is measured.

- Bragg-filtered images can be obtained of amplitude and phase of the lattice fringes as a function of positions in the image:

  $$B_g\left(\vec{r}\right) = 2A_g\left(r\right)\cos\left\{2\pi\vec{g}\cdot\vec{r} + P_g\left(\vec{r}\right)\right\},$$

  with $P_g\left(r\right)$ the phase image for the chosen Bragg reflections *g*, which is related to the displacement field distorting the fringes with respect to the reference lattice.

- In reciprocal space, assuming the difference of the reciprocal lattice vectors between the image and the reference lattice is $\vec{g} \rightarrow \vec{g} + \Delta\vec{g}$, thus the phase as a function of positions is given by: $P_g\left(\vec{r}\right) = 2\pi \cdot \Delta\vec{g} \cdot \vec{r}$.
- In real space, due to the presence of a displacement field, $\vec{u}$, with a relation $\vec{r} \rightarrow \vec{r} - \vec{u}$. The phase as a function of positions can be written as: $P_{gi}\left(\vec{r}\right) = -2\pi \cdot \vec{g}_i \cdot \vec{u}\left(\vec{r}\right)$. By choosing two non-collinear sets of lattice fringes, the two-dimensional displacement field $\vec{u}\left(\vec{r}\right)$ can be calculated.

In general, the GPA algorithm provides a rapid and quantitative way to measure displacement fields from HR-TEM images.

3.3.3 Strain measurement

The 2D strain field consists of four components. e_{11}, e_{12}, e_{21} and e_{22}, which is gradient of the 2D displacement field. It can be described as a 2 ×2 matrix:

$$e = \begin{pmatrix} e_{11} & e_{12} \\ e_{21} & e_{22} \end{pmatrix} = \begin{pmatrix} \partial u_x / \partial x & \partial u_x / \partial y \\ \partial u_y / \partial x & \partial u_y / \partial y \end{pmatrix}. \tag{3.20}$$

A complete description of the strain field can be separated into two terms: the symmetric term ε and the anti-symmetric term ω, with:

$$\varepsilon = \tfrac{1}{2}\left\{e + e^T\right\}, \tag{3.21}$$

$$\omega = \tfrac{1}{2}\left\{e - e^T\right\}, \tag{3.22}$$

where T is the transpose of the matrix.

The diagonal elements of the symmetric term ε, ε_{11} and ε_{22}, describe the strength of the relative lattice distortion, while the off-diagonal elements of the anti-symmetric term ω, ω_{12} $\left(\omega_{12} = \tfrac{1}{2}\left(e_{12} - e_{21}\right)\right)$ and ω_{21} $\left(\omega_{21} = \tfrac{1}{2}\left(e_{21} - e_{12}\right)\right)$, indicate a rotation of the lattice. For small values of the off-diagonal elements, the rotation angle of the lattice α in radians can be directly obtained as $\tan\alpha \approx \alpha$.

Chapter 4 Wave aberrations in HRTEM

4.1 Wave aberrations by lens system

The objective lens system is crucial to the imaging properties of the electron microscope. Fig.4-1 depicts the image formation in a lens system. A point object P_0 (co-ordinate $\vec{u}$) follows a ray with angular coordinate $\vec{g}$ and is imaged into P_{iG} (coordinate $\vec{w}_i$) in the image plane. Due to the presence of aberrations, they cause wave aberrations, W, which is the distance between the real and the ideal wavefront [46]. In the image plane, P_0 will be imaged into P_i then, causing a displacement Δw_i.

The wave aberration $W\left(\vec{u},\vec{u}*,\vec{g},\vec{g}*\right)$ is a function of the positional and angular coordinates of rays, with $\vec{u}$ and $\vec{g}$ the positional and angular coordinates, respectively; the '$*$' indicates the complex conjugate. For HRTEM, the imaged region of the object is so small that the wave aberration of the positional dependence $\vec{u}$ can be neglected. The wave aberration W can thus be approximated by axial wave aberration only, hence, W is a function of angular co-ordinates $W\left(\vec{g},\vec{g}*\right)$. The wave aberration W causes a phase shift χ to the wave, which is usually nominated as the aberration function:

$$\chi = \frac{2\pi W}{\lambda}. \tag{4.1}$$

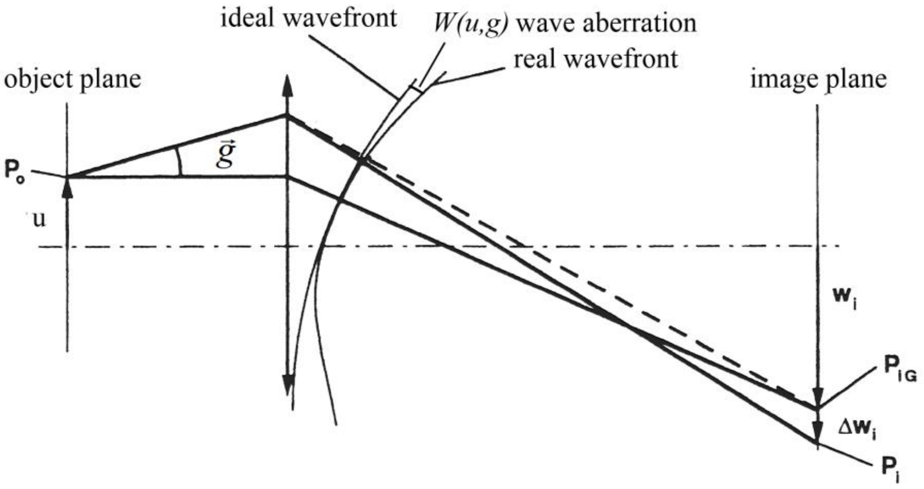

Fig.4-1. Scheme of the wave aberrations in a lens system.

4.2 Description of wave aberrations including higher order aberrations

If the microscope is well aligned, the main wave aberration is induced by the low order aberrations (sec.1.3) of the objective lens. For CTEM, i.e. Philips CM300 UT with its highest resolution of 1.6 Å, a description up to the 3rd order aberrations is sufficient. However, with the increase of the resolution of microscopes, especially the achievement of a sub-Angstrom resolution, the description of low order wave aberrations of the objective lens alone is not sufficient, because highly resolved image details rely on transfer of high spatial frequencies. Higher order aberrations also affect the imaging. Thus, it is necessary to describe the aberration function including a large number of aberrations with higher orders and higher rotational symmetries. A new construction of the nomenclature for the individual aberration coefficients was proposed [47] with each aberration coefficient symbolized as c_{mn}: m the power-law dependence of the spatial frequency g and n the foldness of the rotational symmetry.

The angular co-ordinate is usually written in a complex form [48-51]:

$$\vec{g} = g_x + i g_y \,. \tag{4.2}$$

Ignoring the term with constant phase offset c_{00}, the aberration function is then:

$$\chi = \sum_{m,n} \chi_{mn}\left(\vec{g}, \vec{g}^{\,*}\right) = \sum_{m,n,m+n=2l} \frac{2\pi}{\lambda} \cdot \frac{\lambda^m}{m} \mathrm{Re}\left[c_{mn} \cdot \vec{g}^{\,*\frac{m+n}{2}} \cdot \vec{g}^{\frac{m-n}{2}} \right]. \tag{4.3}$$

for $m > 0$, $l \in \mathbb{N}_0$ and Re[] the real part.

Eq.4.3 can be expanded up to the 6th order in $\vec{g}$:

$$\begin{aligned}\chi = \sum_{m,n,m+n=2l} \frac{2\pi}{\lambda} \cdot \mathrm{Re}\Bigg\{ & c_{00} + \lambda c_{11} \cdot \vec{g} + \frac{\lambda^2}{2}\left[c_{20}\vec{g}^{\,*} \cdot \vec{g} + c_{22}\vec{g}^{\,*2} \right] + \frac{\lambda^3}{3}\left[c_{31}\vec{g}^{\,*2} \cdot \vec{g} + c_{33}\vec{g}^{\,*3} \right] + \\ & \frac{\lambda^4}{4}\left[c_{40}\vec{g}^{\,*2} \cdot \vec{g}^{2} + c_{42}\vec{g}^{\,*3} \cdot \vec{g} + c_{40}\vec{g}^{\,*4} \right] + \\ & \frac{\lambda^5}{5}\left[c_{53}\vec{g}^{\,*3} \cdot \vec{g}^{2} + c_{53}\vec{g}^{\,*4} \cdot \vec{g} + c_{55}\vec{g}^{\,*5} \right] + \\ & \frac{\lambda^6}{6}\left[c_{60}\vec{g}^{\,*3} \cdot \vec{g}^{3} + c_{62}\vec{g}^{\,*4} \cdot \vec{g}^{2} + c_{64}\vec{g}^{\,*5} \cdot \vec{g} + c_{66}\vec{g}^{\,*6} \right] + \cdots \Bigg\}.\end{aligned} \tag{4.4}$$

The aberration function can be written in the polar form with $\vec{g} = |\vec{g}|\exp(i \cdot \varphi)$ and $\vec{c}_{mn} = |c_{mn}|\exp(i \cdot n\varphi_{mn})$, presenting explicitly the relation of the rotational symmetry:

$$\chi(\vec{g},\varphi) = \sum_{m,n} \chi_{mn}(|\vec{g}|,\varphi) = \sum_{m,n,m+n=2l} \frac{2\pi}{\lambda} \cdot \frac{|c_{mn}|}{m} (\lambda|\vec{g}|)^m \cdot \cos\left[n \cdot (\varphi - \varphi_{mn})\right]. \qquad (4.5)$$

The displacement Δw_i is related to wave aberration χ, defined as: $\Delta w_i = \frac{1}{\pi}\frac{\partial \chi}{\partial \vec{g}^*}$, (4.6)

which can be expressed up to the 6th order in $\vec{g}$:

$$\begin{aligned}\Delta w = {} & c_{11} + \lambda(\vec{g} \cdot c_{20} + \vec{g}^* \cdot c_{22}) + \frac{1}{3}\lambda^2\left[\left(\vec{g}^2 \cdot c_{31}^* + 2\vec{g}\vec{g}^* \cdot c_{31}\right) + 3\vec{g}^{*2} \cdot c_{33}\right] + \\ & \frac{1}{4}\lambda^3\left[4\vec{g}^2\vec{g}^* \cdot c_{40} + \left(\vec{g}^3 \cdot c_{42}^* + 3\vec{g}\vec{g}^{*2} \cdot c_{42}\right) + 4\vec{g}^{*3} \cdot c_{44}\right] + \\ & \frac{1}{5}\lambda^4\left[\left(2\vec{g}^3\vec{g}^* \cdot c_{51}^* + 3\vec{g}^2\vec{g}^{*2} \cdot c_{51}\right) + \left(2\vec{g}^4 \cdot c_{53}^* + 4\vec{g}\vec{g}^{*3} \cdot c_{53}\right) + 5\vec{g}^4 \cdot c_{55}\right] + \\ & \frac{1}{6}\lambda^5\left[6\vec{g}^3\vec{g}^{*2} \cdot c_{60} + \left(2\vec{g}^4\vec{g}^* \cdot c_{62}^* + 4\vec{g}^2\vec{g}^{*3} \cdot c_{62}\right) + \left(\vec{g}^5 \cdot c_{64}^* + 5\vec{g}\vec{g}^{*4} \cdot c_{64}\right) + 6\vec{g}^{*5} \cdot c_{66}\right].\end{aligned} \qquad (4.7)$$

The nomenclature of the aberration coefficients up to 6th order is listed in table 4-1, together with the nomenclature of Uhlemann & Haider [48].

A criterion of the tolerance limit in HRTEM was proposed as a maximum parasitic phase shift of π/4 for the individual aberration within the information limit k_{max} [48,52]. The allowed magnitude for each aberration coefficient is calculated and listed in col.(5) of table 4-1 with 300 keV accelerating voltage and $k_{max} = 12.5\ \text{nm}^{-1}$. The values of defocus and spherical aberration at 'bright-atom' contrast condition are given with a '*' notation. In reality, each individual aberration contributes to the phase shift of the aberration function at the specific spatial frequencies. Thus, a new criterion of the tolerance limit in phase shift is needed by taking all of the aberrations into account. Furthermore, because of different rotational symmetries of the individual aberrations, the azimuthal effects should also be considered.

The specific features for the individual aberrations can thus be presented in the form of the phase plate (fig.4-2) up to the 6th order in *g*. They are calculated according to the π/4-limit for individual aberrations with the azimuthal angle set to be zero.

Aberration coefficient	**Symbol** [47]	**Symbol** [48]	**π/4 limit**	**Allowed magnitude**
Constant phase offset	c_{00}			
Image displacement	c_{11}	A_0		
Defocus	c_{20}	C_1	$\frac{1}{4}\left(\lambda g_{\max}^2\right)^{-1}$	0.81 nm
‘Bright-atom’ contrast condition:	$-\frac{16}{9}\left(\lambda g_{\max}^2\right)^{-1}*$			**-5.77 nm***
2-fold astigmatism	c_{22}	A_1	$\frac{1}{4}\left(\lambda g_{\max}^2\right)^{-1}$	0.81 nm
Axial coma	c_{31}	$3B_2$	$\frac{3}{8}\left(\lambda^2 g_{\max}^3\right)^{-1}$	49.47 nm
3-fold astigmatism	c_{33}	A_2	$\frac{3}{8}\left(\lambda^2 g_{\max}^3\right)^{-1}$	49.47 nm
Spherical aberration	c_{40}	C_3	$\frac{1}{2}\left(\lambda^3 g_{\max}^4\right)^{-1}$	2.68 μm
‘Bright-atom’ contrast condition:	$\frac{64}{27}\left(\lambda^3 g_{\max}^4\right)^{-1}*$			**-12.70 μm***
Star aberration	c_{42}	$4S_3$	$\frac{1}{2}\left(\lambda^3 g_{\max}^4\right)^{-1}$	2.68 μm
4-fold astigmatism	c_{44}	A_3	$\frac{1}{2}\left(\lambda^3 g_{\max}^4\right)^{-1}$	2.68 μm
5th-order axial coma	c_{51}	$5B_4$	$\frac{5}{8}\left(\lambda^4 g_{\max}^5\right)^{-1}$	135.98 μm
3-lobe aberration	c_{53}	$5D_4$	$\frac{5}{8}\left(\lambda^4 g_{\max}^5\right)^{-1}$	135.98 μm
5-fold astigmatism	c_{55}	A_4	$\frac{5}{8}\left(\lambda^4 g_{\max}^5\right)^{-1}$	135.98 μm
6th-order spherical aberration	c_{60}	C_5	$\frac{3}{4}\left(\lambda^5 g_{\max}^6\right)^{-1}$	6.63mm
6th-order star aberration	c_{62}	$6S_5$	$\frac{3}{4}\left(\lambda^5 g_{\max}^6\right)^{-1}$	6.63 mm
Rosette aberration	c_{64}	$6R_5$	$\frac{3}{4}\left(\lambda^5 g_{\max}^6\right)^{-1}$	6.63 mm
6-fold astigmatism	c_{66}	A_5	$\frac{3}{4}\left(\lambda^5 g_{\max}^6\right)^{-1}$	6.63 mm

Table 4-1. Lists of aberration coefficients up to the 6th order. Symbols for different nomenclatures are listed in col.(2) and col.(3), respectively. The π/4 limit and the allowed magnitude of aberration coefficients for 300 keV and $g_{max} = 12.5\ \text{nm}^{-1}$ are listed in col.(4) and col.(5), respectively.

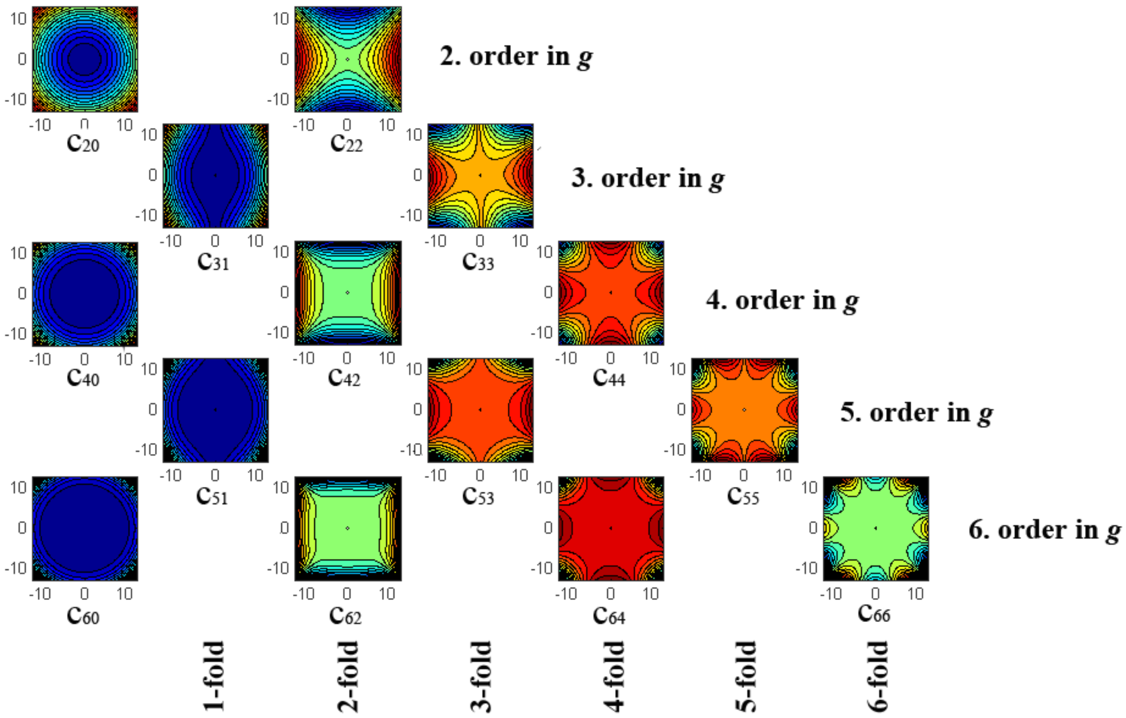

Fig.4-2. Phase plates of the individual aberrations arranged with the orders in g and the rotational symmetries, which are calculated with 300 keV accelerating voltage and $g_{max} = 12.5\ nm^{-1}$.

4.3 Aberration corrections

The wave aberrations can be corrected directly on the microscope. On the other hand, the retrieved exit-plane wave can be corrected by means of appropriate software.

- If the microscope is well aligned at the near aberration-free state, using the hexapole spherical aberration corrector offered by CEOS GmbH [53], the wave aberrations up to the 6th order spherical aberration can be determined and corrected by the means of beam-tilted diffractogram series.
- The wave aberration correction by software is indirect. Because from the recorded images the phase information of the wave function is lost. The exit-plane waves should first be retrieved from focal-series of images with the use of the Philips/Brite-Euram software ‘TrueImage’ [54]. The ‘aberration-free’ exit-plane wave can be obtained by the aberration corrections mathematically. Both steps require numerical calculations [55-57].

Chapter 5 Analytical electron microscopy [58]

5.1 Inelastic scattering processes

High energy electrons undergo mainly elastic scattering processes due to the large cross sections. However, several inelastic scattering processes, e.g. phonon creation, Plasmon excitation and core electron excitation, take place as well [15].

5.1.1 Phonon creation

Due to vibrations of crystal lattice, electrons take energy losses quantified by phonons, with an energy loss $\Delta E \sim 10^{-2}$ eV. It cannot be detected or separated from the elastically scattered electrons.

5.1.2 Plasmon excitation

Plasmon is oscillations of valence electrons in solids, stimulated by the transverse of high-energy electrons through the sample, with an energy loss of tens of eV. The energy of Plasmon increases with the density of bonding electrons. It can be used to estimate the density of valence electrons in Electron Energy-Loss Spectrometry (EELS). By measuring the intensities of Plasmon peaks in EELS, the thicknesses of a TEM sample can also be estimated. The thicker the sample is, the more Plasmon is excited.

5.1.3 Core electron excitation

High-energy electrons may lose energy by exciting electron(s) of an atom in materials from a core state to a free state or to the continuum of free electrons beyond the Fermi level, with a typical energy loss of $10^2 \sim 10^4$ eV. The EELS spectra represent the ‘absorption edges’ of the elements in materials, showing jumps in intensities at the threshold energies for core electron excitations. After the excitations of a core electron, it decays accompanied with an emission of a characteristic x-ray, which can be used for micro-chemical analysis by energy dispersive x-ray spectrometry (EDS).

Both EELS and EDS in analytical TEM can be used for elements identifications, therefore, their concentrations and spatial distributions in specimens. With the advantage of the high energy resolution, electron energy loss near-edge spectroscopy (ELNES) in EELS spectra can provide additional information on the chemical and structural environment around an atom.

5.2 X-ray microanalysis by Energy-dispersive spectrometer (EDS)

Fig.5-1 shows the assembly of the EDS detector at the objective lens of the microscope. The excited x-ray photons from the TEM specimen are collected by the Si(Li) detector. After subtraction of the background in the measured x-ray spectrum, the peaks can be integrated or fitted by functions, such as by Gaussian functions. Sometimes, overlap of peaks occurs. It had better work with multiple peaks, such as $K\alpha$, $K\beta$, L-series and so on. Such sets of intensities ($\boldsymbol{I_i}$) can then be converted into elemental concentrations ($\boldsymbol{c_i}$) with so- called ‘Cliff-Lorimer’ factor [59], which is independent of specimen thickness and chemical composition, given by:

$$\frac{c_a}{c_b} = k_{ab}\frac{I_a}{I_b} \tag{6.1}$$

The Cliff-Lorimer factor remains constant for a given accelerating voltage and the determined EDS spectrometer.

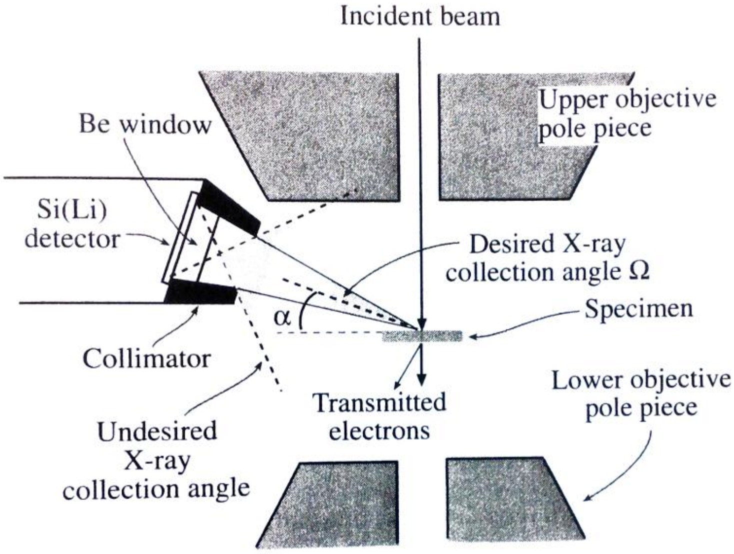

Fig.5-1. Cross-section of the EDS detector.

Caution should be taken, however, due to the effects of the condenser apertures and the misalignment of the microscope. Some artificial signals may originate either from the condenser aperture or the neighbouring area of interest, which might be included in the measured EDS spectrum. Thus, for the quantification of element concentrations by EDS, it is strongly recommended to eliminate those effects by subtracting with an EDS spectrum, which was obtained with the incident electron beam in the vacuum near the area of interest for the identical parameters of acquisition.

5.3 Energy-Loss spectroscopy and Energy-Selecting imaging

Because the energies of absorption edges in EELS are reliable indicators of the elements in materials, an EELS spectrometer is used to detect the EELS, which is mounted after the projector lens of a TEM. Fig.5-2 shows the assembly of the Gatan post-column imaging filter (GIF), which is composed of the entrance aperture, alignment coils, magnetic prism, a number of quadrupole and sextupole magnetic lenses and the CCD detector.

The GIF can be operated in spectroscopic mode and in image mode.

- In the spectroscopic mode, a highly-focused electron probe incident on the specimen and the EELS spectra are formed on the CCD detector, which can be used for the element identifications and therefore the elements concentrations and the local structural environment. The spatially resolved EELS spectroscopy was first applied by Reimer et al. [60]. Using a 2D camera detector, it is possible to record spectrum images which contain a series of EELS spectra acquired simultaneously as a function of a spatial coordinate [61].

- Unlike the spectroscopic mode with highly-focused electron beam, in the image mode, it uses a nearly parallel electron beam to incident on the surface of specimen, which reduces the risk of the beam damage to the specimen. With the chosen energy loss and the selected energy window offered by GIF, such energy selected images (ESI) are formed. 2D elemental maps can be obtained from the increase of intensity at an absorption edge of the chosen elements in EELS spectra [62] and there are generally two types of elemental maps.

a) ‘Jump-ratio image’, where the post-edge image is divided by a pre-edge image. By division, variations in specimen thickness and diffraction contrast are cancelled.

b) ‘Three-window image’, where the post-edge image are subtracted by the intensities which is extrapolated by fitting the background of two pre-edge images to the energy window of the post-edge image. Though it requires longer integration time and it might be noisier compared with ‘jump-ratio images’, however, it provides better elemental quantifications.

To fit the background more precisely, more than two pre-edge images are recorded, which can be used to extrapolate a better background to the energy window of the post-edge images.

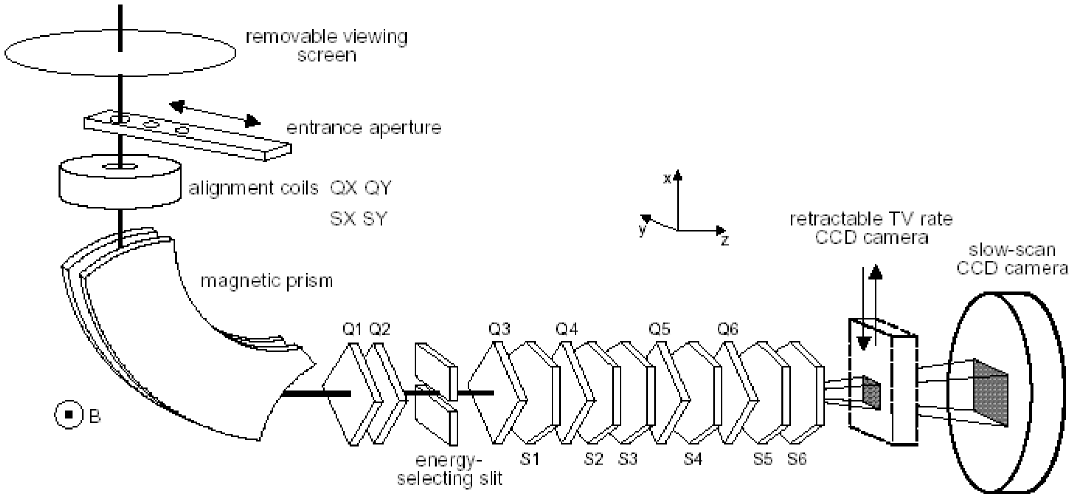

Fig.5-2. Cross-section of the Gatan post-column imaging filter (GIF).

Chapter 6 HAADF /STEM Imaging

6.1 Introduction

Since its ability of single heavy atom detection [63] with a HR-STEM, the annular dark field (ADF) imaging has been recognized as a powerful tool for analyzing the micro-structure. The spatial resolution in ADF-STEM can be equal or can even overcome the CTEM information limit of the microscope, if both sample and specimen holder are sufficiently stable against drift [64-66]. With the advances of C_s correctors [67] in the new generation (S)TEM instrumentation, where a probe size below 1 Å can be reached, it allows the imaging of specimens at atomic resolution.

6.2 Optical system of ADF /STEM

The ray path in the optical system of the STEM (fig.6-1) is reversed to that of the CTEM system (fig.1-3). The incident electrons are assumed to be moving in the positive z direction and the image plane on an x-y plane. For STEM, the objective lens is positioned before the specimen and forms a focused probe on to the specimen. A set of scan coils is positioned before the objective lens. For the new generation of STEM instrumentation, the C_s corrector is positioned at the probe-side of the specimen, which can ‘correct’ the aberrations caused by the objective lens and forms a nearly aberration-free probe with a size of less than 1 Å (FEI Titan80-300 probe-side aberration corrected electron microscope). The STEM may have two different types of detectors:

- ADF detector, collecting electrons scattered to high angles.
- BF detector, detecting electrons passing through the specimen at or very close to the optical axis.

Using the advances of HR-STEM imaging with nearly the same gain, the BF detector can also be replaced by GIF for EELS analysis, in particular for elemental mapping of complex non-periodic structures [68-70].

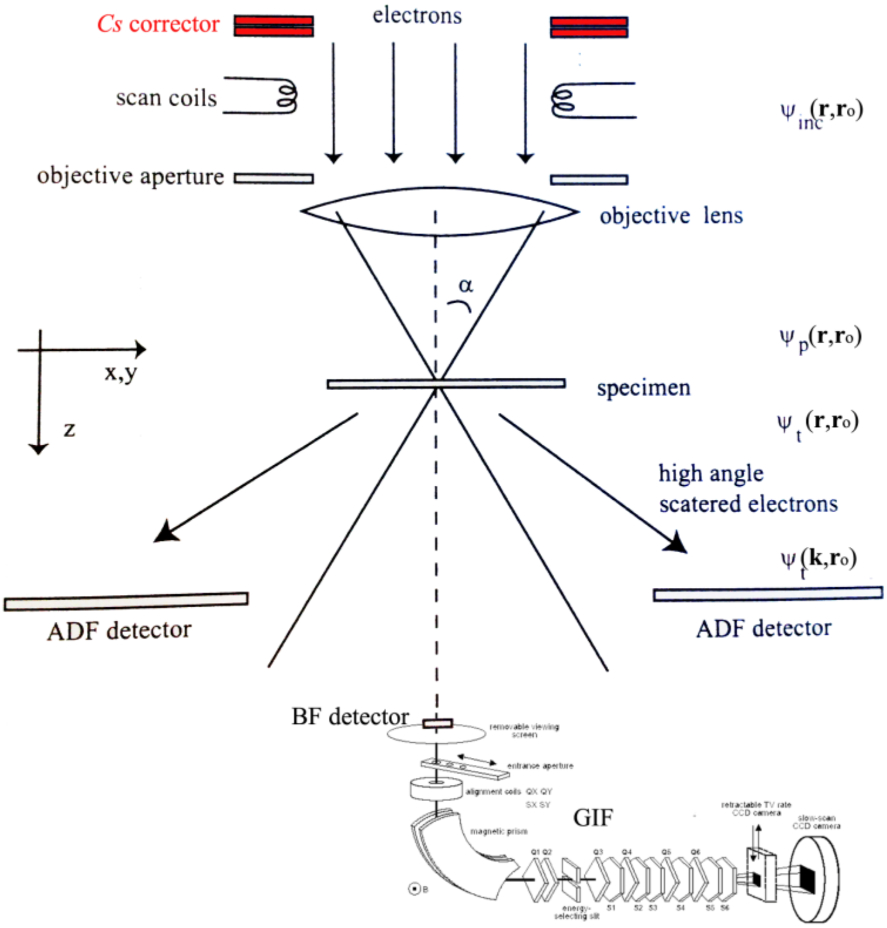

Fig.6-1. Simplified model of a HAADF /STEM, with the placement of the electron wave functions ψ. The condenser lens and projected lens systems are ignored. The C_s corrector is positioned at the probe-side in red. The BF detector can be retracted when GIF is utilized.

6.3 HAADF /STEM image contrast

Whereas CTEM images are partially coherent interference patterns of the electron wave, the image formation in STEM can be considered as practically incoherent [71,72], which suffers less contrast reversals from varying sample thickness and defocus compared to CTEM images. The intensity of HAADF image increases roughly with the square of average atomic number $\bar{Z}$ of the atom column, due to the scattering close to Rutherford scattering. Therefore, qualitative chemical information can be extracted directly from the HAADF image contrast, without time-consuming and delicate image simulations [73].

However, the origin of HAADF image contrast is not simple, because both elastic and inelastic scattering contribute to the intensities at high angles [74-79]. Furthermore, the incoherent contributions of the thermal diffuse scattering (TDS) should be incorporated with HAADF image contrast [72,75].

6.3.1 Effects that influence the contrast of HAADF imaging

There are several effects that can influence the HAADF image contrast.

1. Influence of probe parameters, size of objective aperture and defocus of a probe-forming lens, C_s and convergence angle [80-83].
2. Collecting angle for HAADF detector [81,84-87].
3. Occupancy of the atomic columns, such as their averaged atomic number [74,75,88-97].
4. Coherence along the atom columns of the incident electron beam [75,76,98].
5. Channelling effect [89,91,93,99-102]: the probe focusing properties of the atom columns with one atom type might be different for columns with different atoms [74,93].
6. Occurrence of ‘cross-talk’, e.g. a transfer of probe intensity from one column to another or from the channels to the columns [74,75,93,99].
7. Introduction of artefacts when the setting of black level is big enough in the aberration-corrected ADF-STEM imaging [103].
8. Effects of orientation, tilt and amorphous layers of sample in HR-STEM imaging, respectively [104-106].
9. Static atom displacement [107].

To interpret the contrast of the experimental HAADF images quantitatively, it requires comparison with the HAADF/STEM image simulations.

6.4 HAADF image simulations

For HAADF/STEM imaging, a convergent illumination condition is used and the wave function of an incident probe, centred at r_0 at the up-surface of the specimen, can be written as:

$$\psi_{inc}(r,r_0)=\int_{all\ k} A(k)\exp\left[-2\pi ik\cdot(r-r_0)-2\pi i\chi(k)\right]dk\,, \tag{6.1}$$

with $\chi(k)$ the objective-lens aberration function, $A(k)$ aperture function.

There are several approaches already developed to simulate HAADF images [23,75,79,88,91-95,97,108-114], including the Bloch-wave method (sec.3.2.1) and the multi-slice method (sec.3.2.2). The method of Wang and Cowley [77,79] takes both elastic and inelastic scattering into account. Using the Bloch-wave method, the images can be calculated by dynamic elastic scattering or with the assumption of the atoms as independent incoherent scatterers. The multi-slice method, however, can be applied to calculations for various objects. Using the wave function of the incident probe, it is then propagated through the specimen by eq.3.16. After passing the specimen, the wave function $\psi_t(k,r_0)$ is propagated to the HAADF detector in the far field and the resulting image intensity $I_{\det}$ is incoherently integrated over the detector:

$$I_{\det}(\vec{r}_0)=\int_{k_{in}\le|\vec{k}|\le k_{out}} \left|\psi_t\left(\vec{k},\vec{r}_0\right)\right|^2 D\left(\vec{k}\right)d\vec{k}\,. \tag{6.2}$$

with $D(\vec{k})$ the detector function. It requires enormous computing time for the integrations of scattering intensities over the HAADF detector at each probe position.

Since the information on the absolute intensity of the incident electron beam is missing, LeBeau et al. [80] suggested a new method allowing the measurement of normalized intensity.

6.4.1 TDS approaches

The major signal source of the HAADF images is from thermal diffuse scattering (TDS) by electron-phonon interaction. There are several approaches quantifying the TDS contribution for HAADF images.

The effect of TDS for HAADF images can be treated as an absorptive potential for high-angles [110,115-117]. The total absorptive potential for high angles is given by:

$$V''^{HA}_{\vec{g}} = \frac{2\pi\hbar^2}{m_0}\frac{1}{\Omega}\sum_k f_k^{HA}\left(s,M_k\right)\exp\left(-M_k s^2\right)\exp\left(-2\pi i\vec{g}\cdot\vec{r}_k\right), \tag{6.3}$$

where $\vec{r}_k$ and M_k describe the position and Debye-Waller factor of the atom k, respectively; m_0 the electron rest mass and Ω unit cell volume.

Using the Einstein model, the absorption form factor for high angles is derived as:

$$f_k^{HA}\left(s,M_k\right) = \frac{4\pi\hbar}{m_0 v}\int_{\det ector} f_k\left(\left|s'\right|\right) f_k\left(\left|s-s'\right|\right)\left[1-\exp\left\{-2M_k\left(s'^2-s\cdot s'\right)\right\}\right]d^2s', \tag{6.4}$$

with the integration over the detector area [72].

The effect of TDS can also be taken into account by averaging the scattered intensity for the random atom displacement, commonly referred to as the frozen lattice or frozen phonon approximation [94,96]. The ‘frozen phonon’ model agrees well with the mixed dynamic form factor (absorptive potential method) approach in Bloch-wave calculations [118].

6.4.2 ‘qSTEM’ (quantitative STEM) package

Several programs are available for HAADF image simulations, such as E. J. Kirkland [111], who published a source code for STEM image calculations. However, that program is inefficient and difficult to make dedicated HAADF image simulations. The qSTEM’ package source code by Koch [23], however, is used for the HAADF image simulations of my Ph.D. work. The reasons for choosing the ‘qSTEM’ package for STEM image simulations are as follows:

1. Inclusion of the ‘frozen phonon’ approximation for TDS simulation.
2. Generation of a true 3*D* crystal potential for extremely thin slicing. Thus, it allows large illumination condition, with electron propagation normal to potential slices.
3. Inclusion of chromatic aberration and the size effect of the electron source.
4. Efficiency with FFTW (Fast Fourier Transform of the West) algorithm [119].
5. Friendly graphic user interface (GUI) by Matlab [120].

6.5 Extraction of information with the intensity line profile

To extract information from the raw HAADF images, the intensity line profiles are integrated over certain widths including at least one sub-lattice. The integrated intensities from the line profiles can be considered as the contribution from one atom column. Caution must be taken, however, with the introduction of additional error. Assuming the intensity of an atom is of a 2*D* Gaussian shape, shown in fig.6-2. With the operation of the intensity line profile over certain widths, in principle, we have reduced the 2*D* information to 1*D* information, resulting in the redistribution of the intensities. For example, using Digital Micrograph (DM), each pixel of the line profile is the averaged value for certain position of the image over the integrated widths.

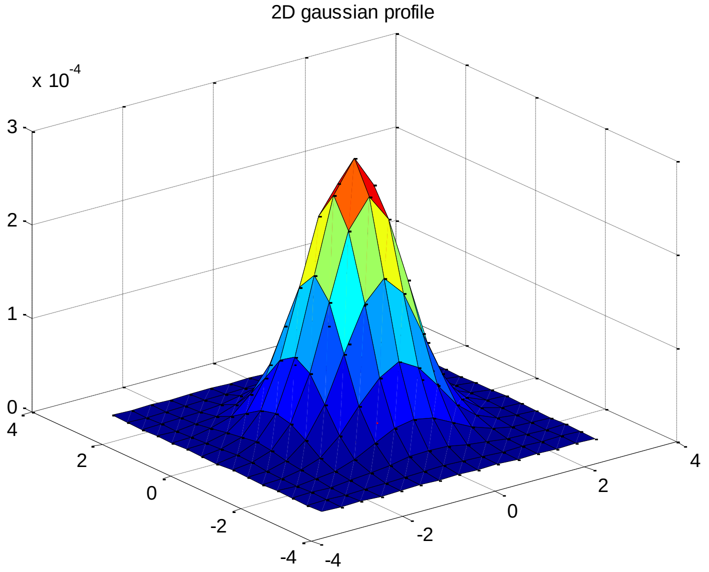

Fig.6-2. 2D Gaussian profile of an atom column.

Moreover, with different sampling rate, the intensity line profile with the same integration widths is different. (Appendix D). Neither the maximum value of the intensity nor the integrated intensity with the averaged value over certain integration widths represents the contribution from the atom columns precisely. The contribution of the atom columns from the atomic resolution HAADF images should be the sum of the intensity value with the corresponding atom columns.

II. Experimental part

Chapter 7 Indium doped Zinc Oxide compounds ($In_2O_3(ZnO)_m$)

7.1 Introduction

Due to its unique optical, electric and piezoelectric properties, zinc oxide (ZnO) is widely used for various device applications [121]. In order to tailor its physical and chemical properties, ZnO is usually doped with other oxides, such as In_2O_3, Ga_2O_3, Fe_2O_3 and so on. In_2O_3 is the basic material of the transparent conducting oxide semiconductor, used for transparent electrodes [122]. Sintering of ZnO with additions of trivalent In^{3+} ions form homologous compounds of the type $In_2O_3(ZnO)_m$ (with m integer), which were first synthesized and studied by Kasper in 1967 [123]. At the same time, the homologous compounds of $In_2O_3(ZnO)_m$ have a polytypoid structure with characteristic layer structures and domain structures.

The In_2O_3-ZnO system has drawn much attention and was studied intensively by x-ray diffraction and methods of Transmission Electron Microscopy (TEM) such as electron diffraction, EELS and high-resolution (HR) electron microscopy [124-147]. Through x-ray diffraction and HR electron microscopy studies, Cannard and Tilley proved the presence of the new intergrowth phases in the ZnO-In_2O_3 system proposed by Kasper, consisting of ZnO slabs with wurtzite type of structure, which are separated by In_2O_3 thin layers [124]. The crystal structure of $In_2O_3(ZnO)_m$ (m = 2-5,7) was refined by x-ray diffraction studies, having the space group $R\bar{3}m$ for m equal odd or $P6_3/mmc$ for m equal even. The In^{3+} ions occupy layers of edge sharing $\left[\mathrm{InO}_{6/3}^{-}\right]_2^{\infty}$ octahedrons and the wurtzite type of structure $\left[(\mathrm{In,Zn})\mathrm{O}_{4/4}^{+}\right]_3^{\infty}$ consisting of $(\mathrm{InZn}_m)\mathrm{O}_{m+1}^{+}$ tetrahedrons. The octahedral InO_2^- layers were proven by atomic-resolution Z-contrast electron microscopy [127] as well. The structures of $In_2O_3(ZnO)_m$ with m = 3 and m = 5 were determined by powder x-ray diffraction and are displayed in fig.7-1a and fig.7-1b, respectively [128,129]. They exhibit two types of inversion domain boundaries (IDBs) alternatively. Half of the indium atoms are ordered in the close-packed octahedral InO_2^- layers. The $(\mathrm{In,Zn})\mathrm{O}_4$ tetrahedrons are connected via corners to the octahedral layers. Thereby, it forms a planar IDB with two blocks of wurtzite type structure facing 'head-to-head' to the octahedral monolayer. Between the two neighbouring InO_2^- layers are $(InZn_m)O_{m+1}^+$ layers, consisting 4 and 6 $(In, Zn)O_4$ tetrahedral layers for *m* = 3 and *m* = 5, respectively. A second type of inversion of the domain structure must exist within the blocks of wurtzite type $(In, Zn)O_4$ tetrahedrons facing 'tail-to-tail' to each other, which is of a planar form and bounded by the van der Waals force. The second half In atoms are randomly distributed in the $(In, Zn)O_4$ tetrahedrons.

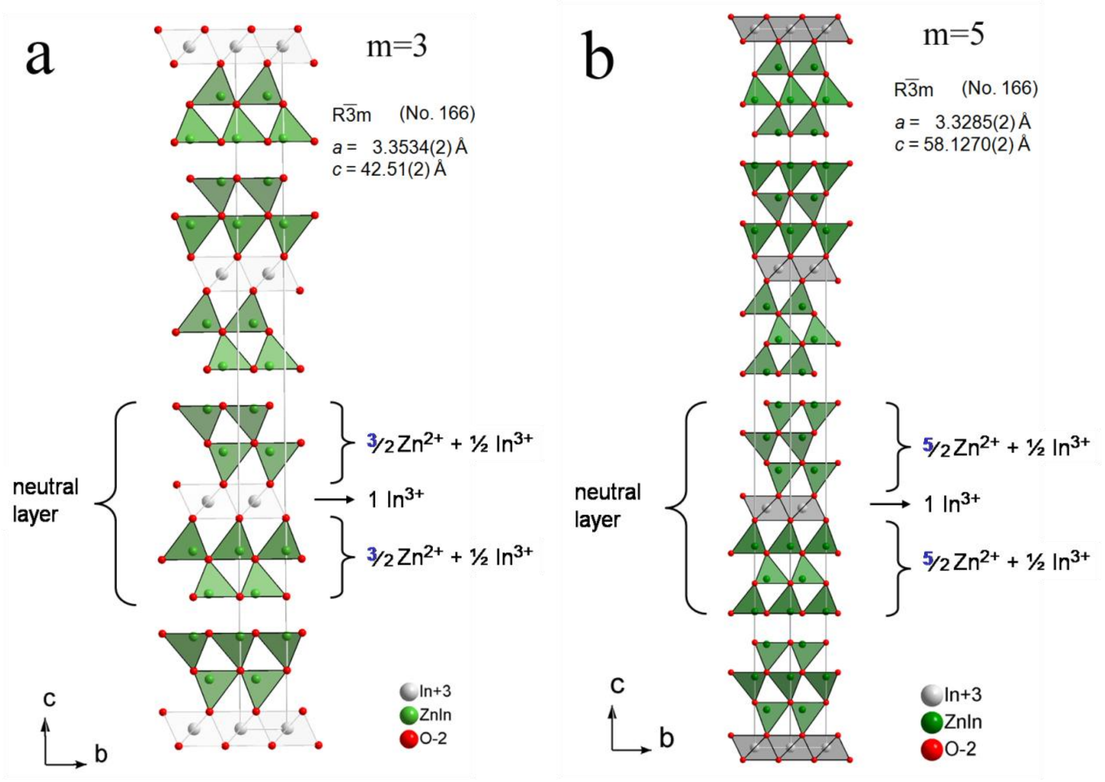

Fig.7-1. Structure of $In_2O_3(ZnO)_3$ a) and $In_2O_3(ZnO)_5$ b) with (In/Zn) atoms in tetrahedral co-ordination and In atoms in octahedral co-ordination.

7.2 Appearance of the pyramidal IDBs for $m \geq 7$

Due to existence of In atoms with relatively larger atom radii inside the $(In, Zn)O_4$ tetrahedrons, it causes local lattice distortions. For $m \geq 7$, with relatively lower In content, there is more spacing for lattice relaxations of the $(InZn_m)O_{m+1}^+$ layers. Instead of a planar form with $m < 7$, such type of the 'tail-to-tail' IDBs now have a zig-zag shaped structure in the blocks of the wurtzite type $(\mathrm{In,Zn})\mathrm{O}_4$ tetrahedrons and the In atoms are supposed on the pyramidal (In,Zn)O slabs [125-128,130,132]. Additionally, by first-principles density-functional theory for the atomic structure of the $In_2O_3(ZnO)_6$ compound, the modulated structure at the 'tail-to-tail' IDBs has a lower total energy than that in a planar form. [140].

Fig.7-2 is a bright-field TEM image of $In_2O_3(ZnO)_m$ system ($m \geq 7$) in $[1\bar{1}00]$ zone axis of ZnO. The variation of the local mean intensity results from the inversion of the polar c-axis of ZnO in the domain structures. Two types of IDBs are visible: the planar IDBs (denoted as basal IDBs) and zig-zag shaped IDBs (pyramidal IDBs). The arrows indicate the polar c-axis of the ZnO domains.

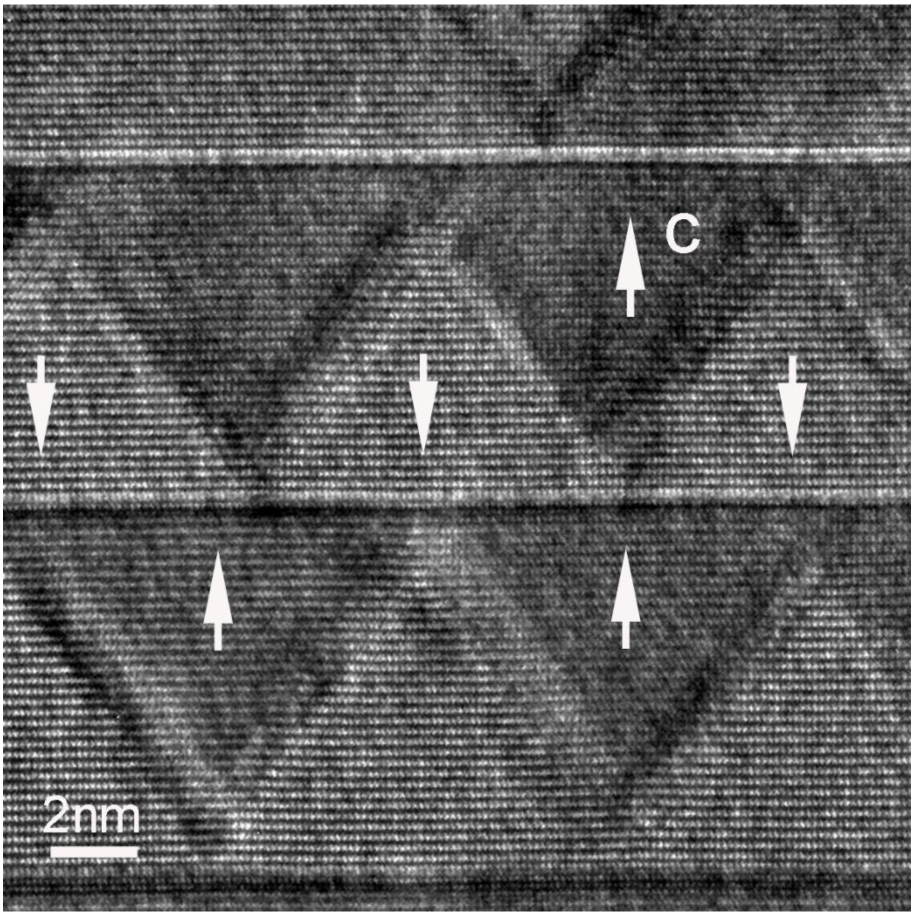

Fig.7-2. TEM lattice image of $In_2O_3(ZnO)_{38}$ in the $[1\bar{1}00]$ zone axis. Arrows indicate c-axis orientation in the ZnO domains.

Unlike the basal IDBs, which can be observed in low-indexed zone axes normal to the polar c-axis of ZnO, contrast variations originated from the pyramidal IDBs depends on the viewing directions and cannot be always observed [131] (fig.7-3). In $[1\bar{1}00]$ zone axis, the contrast of the pyramidal IDBs is quite clear forming zig-zag patterns. However, in $[1\bar{2}10]$ or $[2\bar{1}\bar{1}0]$ zone axis, which is 30 °away from $[1\bar{1}00]$ around c-axis, the pyramidal IDBs appear to be inclined layers with a diffuse contrast. In the other zone axes, the contrast of the pyramidal IDBs can hardly be seen.

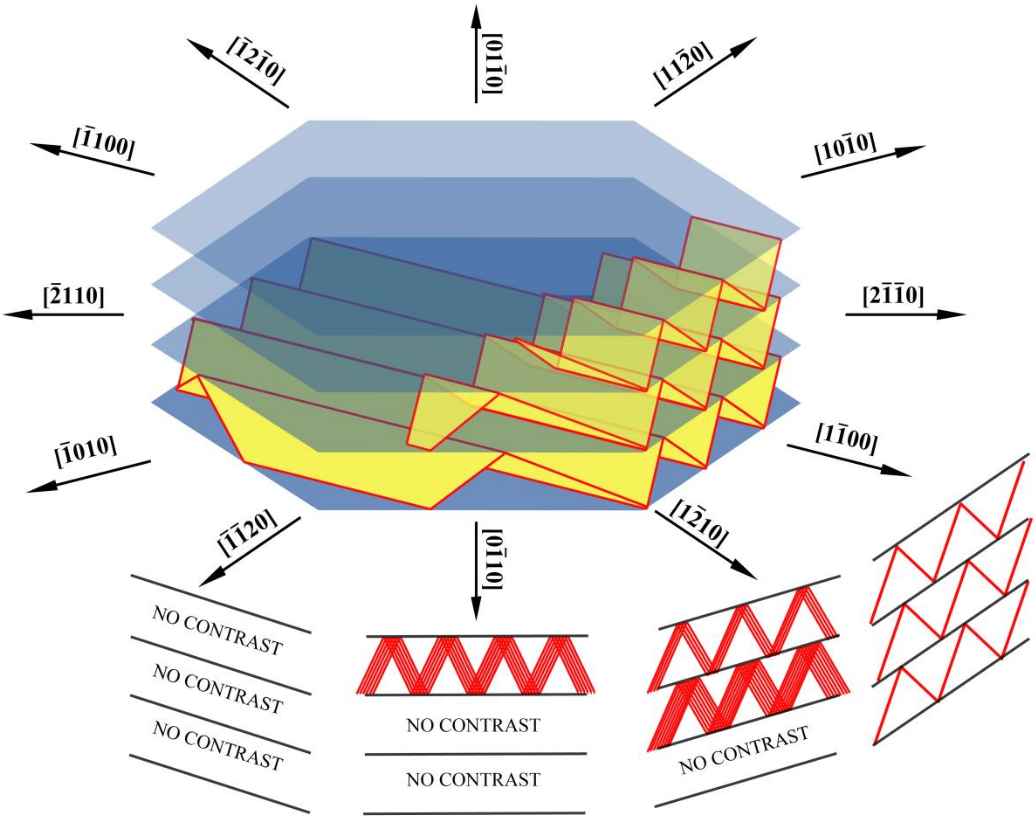

Fig.7-3. Diagram of the 3D structure model of the pyramidal IDB, showing the observed results of the pyramidal IDBs from different viewing directions.

Though the homologous $In_2O_3(ZnO)_m$ compounds ($m \geq 7$) has been studied since 1967 and several local structure models with large unit cells were proposed, the detailed structure of this type of $In_2O_3(ZnO)_m$ compound is still under debate, especially the co-ordination of the In ions, hence the atomic structure of the pyramidal IDBs with precise positions of atoms is more or less unknown. X-ray diffraction cannot be used to determine the local structure of $In_2O_3(ZnO)_m$ compounds with $m \geq 7$: (i) The variations of the inter-atomic distances in these phases between the InO_2^- layers will lead to diffuse intensities; and (ii) pure large crystals have not yet been succeeded to grow. As a powerful tool for the structure studies at the nano-scale, TEM is now the only way to solve the atomic structure of the $In_2O_3(ZnO)_m$ compounds with $m \geq 7$, however, due to the limitation of the resolution, information on these boundaries via TEM hitherto was restricted to imaging in $[2\bar{1}\bar{1}0]$ of ZnO, where the Zn atoms are separated by more than 2.8 Å.

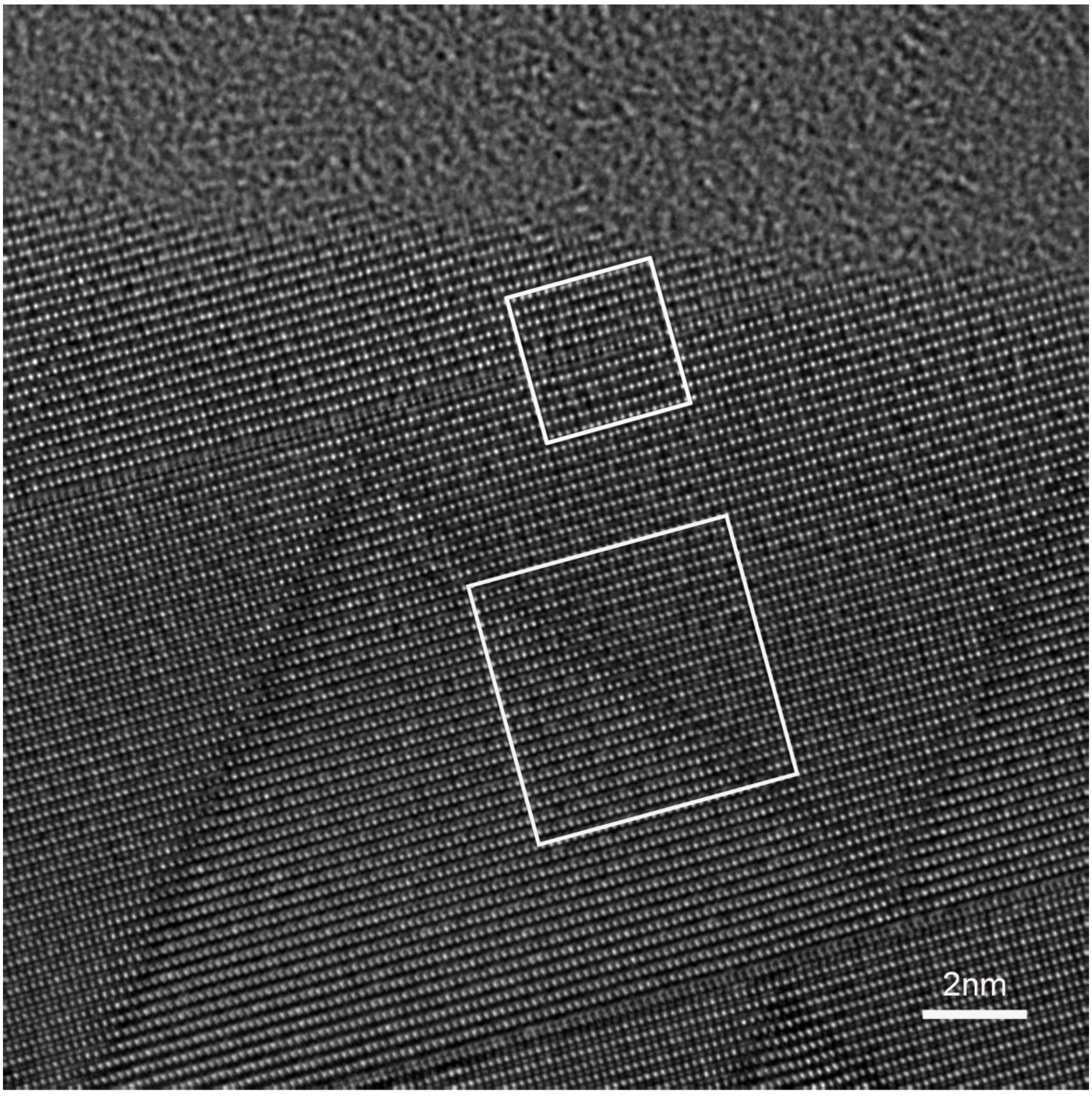

Fig.7-4. C_s-corrected TEM phase-contrast image of $In_2O_3(ZnO)_m$ ($m = 47$) at bright-atom contrast condition in $[1\bar{1}00]$ direction. Two regions of interest at the basal IDB and the pyramidal IDB are marked by boxes, respectively.

With the appearance of the aberration corrector to the electron microscopy, the main lens aberrations of the objective lens like the spherical aberration up to the 5th order can be corrected by insertion of concave lens. The resolution of the new TEM instrumentation now available is much improved up to ca. 0.78 Å with image delocalization as low as 47 pm [148,149]. Thus, it enables phase contrast and Z-contrast imaging also in the $[1\bar{1}00]$ orientation of ZnO, where metal atom columns with spacing of ca. 1.62 Å can be resolved (fig.7-4).

7.3 Goals of the structure studies of $In_2O_3(ZnO)_m$ compounds for $m \geq 7$

The present work is focused on the atomic structures of homologous compounds $In_2O_3(ZnO)_m$ containing both types of IDBs (selected in fig.7-4). For this purpose, a diluted system of $In_2O_3(ZnO)_m$ compounds with low In content, e.g. $m = 30$, were synthesized. Systematic TEM studies on such crystal were conducted by using two types of high resolution contrast in the transmission electron microscopy: the phase contrast and Z-contrast electron microscopy in two low-indexed zone axes of ZnO, together with the dedicate image simulations (HR-TEM image simulations and HAADF image simulations). After the determinations of atom positions, local lattice displacement and the strain fields, the atomic structure and its local chemical composition of $In_2O_3(ZnO)_m$ compounds at both types of IDBs could be retrieved.

Chapter 8 Experimental procedures and methods

8.1 Sample preparation

The $In_2O_3(ZnO)_m$ compounds were prepared through solid state reaction. ZnO and In_2O_3 powders (both of 99.999% purity, Sigma-Aldrich Co.) were mixed thoroughly in molar ratios of $ZnO : In_2O_3 = 30:1$, dried, pressed into pellets and sintered at 1350 °C for 48 hours in sealed platinum tubes to prevent evaporation of the volatile ZnO.

The sample was then prepared by standard TEM specimen preparation procedures, including mechanical grinding, dimpling, polishing and Ar^+ ion beam thinning (RES100, Bal-Tec AG.). For HR-(s)TEM studies, low-voltage ion milling (Gentle Mill, Linda Tec.) with 1 keV Ar^+ ions was utilized for the final step.

8.2 HR-TEM and image simulations

HR-TEM studies of $In_2O_3(ZnO)_{30}$ compounds were first conducted on a Philips CM300UT/FEG equipped with a field-emission electron source. Good TEM specimens were chosen for investigations at the image-side spherical aberration corrected FEI Titan 80-300 electron microscope operated with an accelerating voltage of 300 keV at the Ernst Ruska-Center at Forschungszentrum Jülich. Thin amorphous regions close to the region of interest were used for the adjustment of the C_s corrector with Zemlin tableaus [48]. The spherical aberration coefficient C_s was set at optimum negative value with $C_{S,opt} = -\frac{64}{27}\frac{1}{\lambda^3 g_{max}^4} \approx -13\mu m$, which extends the point resolution up to the instrument's information limit $g_{max} = 12.5\ nm^{-1}$, corresponding to 0.08 nm in real space. A sampling rate of 0.01024 nm / pixel was chosen. In general, single images of a sufficiently thin sample are directly interpretable [149], where the negative C_s setting produces bright-atom contrast condition at over-focus. The displacement fields and the strain fields in the materials can be analyzed by two methods: the 'peak-finding' method and the 'GPA' method (see detailed in sec.3.3). Thus, a complete description of the strain tensor at both IDBs is achieved. Focal series images with constant focus increment of 0.9 nm and 1.9 nm, respectively, were acquired with a 2k×2k CCD camera. The optimum defocus $Z_{opt} = \frac{16}{9}\lambda g_{max}^{-2} \approx 6$ nm for 'bright-atom' contrast conditions was included within the focus range of the series. The electron exit wave was retrieved with the Philips/Brite-Euram software 'TrueImage' from the focal series [150].

Orthorhombic supercells for computer image simulations were constructed on the basis of known structural information in the literature as well as on own lattice images. Lattice images and exit-plane waves were simulated with multi-slice algorithm by using the EMS package [151]. The reconstructed and the simulated exit-plane waves were compared for the interpretation of the details of structure.

8.3 Z-contrast imaging and HAADF image simulations

The local chemical composition of both types of IDBs was investigated by HAADF/STEM imaging at atomic resolution. The experiments were conducted on the probe-side aberration-corrected FEI Titan 80-300 electron microscope equipped with a HAADF detector (Model3000, E.A. Fischione Instr., Inc.). A probe size of < 1 Å was formed at a convergence angle of 25 mrad. The electrons scattered to high angles between 70 mrad and 200 mrad were collected by the high angle annular dark-field (HAADF) detector.

HAADF images with varying In concentration were simulated with the software package 'qSTEM' [23], where the frozen lattice model for the thermal diffuse scattering (TDS) is implanted in the multi-slice algorithm. Comparison of experimentally obtained and computer simulated HAADF images allows the quantification of the In content in the boundary region of the pyramidal IDBs.

Chapter 9 Displacement field and strain field mapping in TEM

Fig.9-1 is an atomic resolution TEM image of $In_2O_3(ZnO)_m$ compounds ($m = 47$) in $[1\bar{1}00]$ zone axis, which is taken at the 'bright-atom' contrast condition. The imaged region contains both types of IDBs: the basal IDB and the pyramidal IDBs. The basal IDB is aligned horizontally. The right-up inset is the powder spectrum of the lattice image, including two 'reflections' $g_{\bar{1}\bar{1}20}$ and g_{0002}. In real space, they correspond to

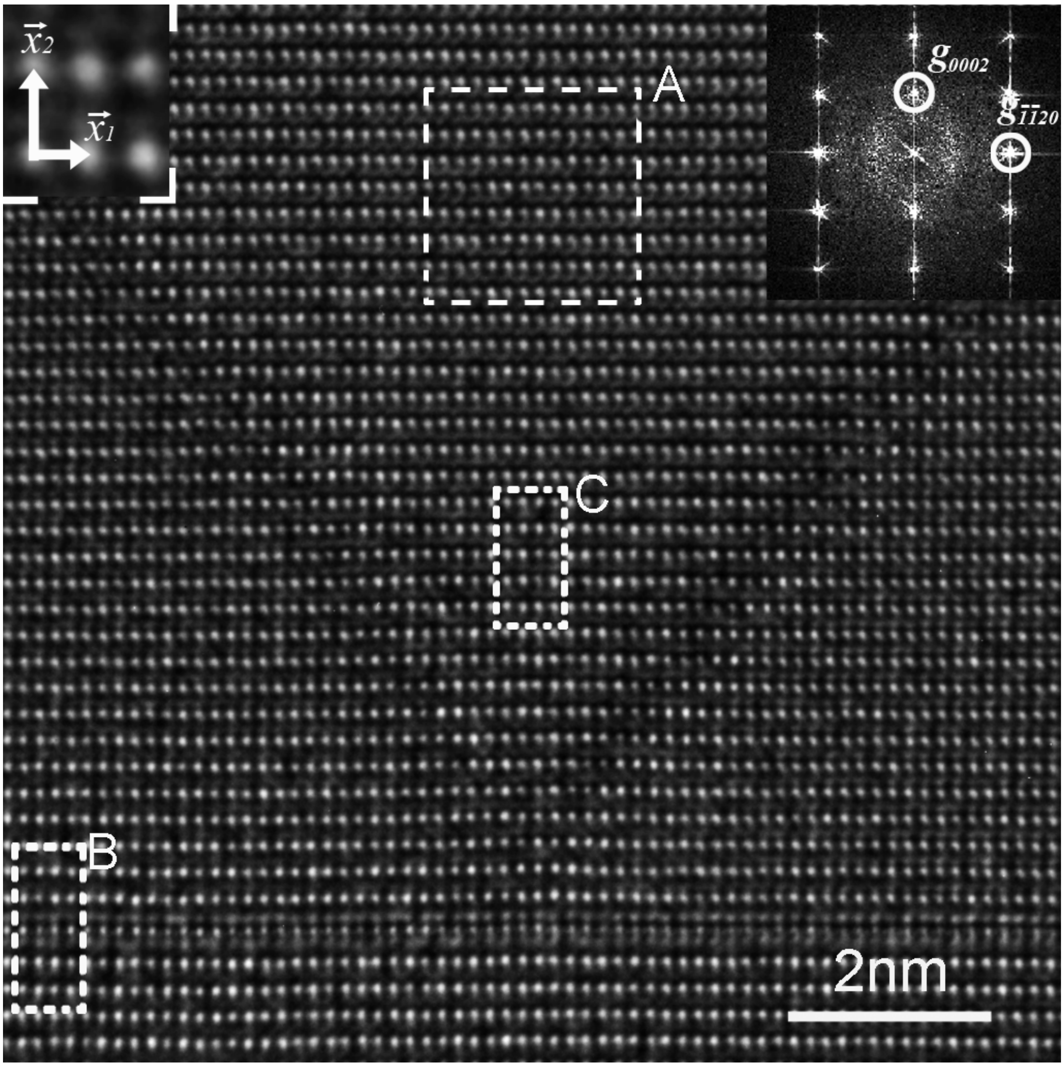

Fig.9-1. HR-TEM image of a $In_2O_3(ZnO)_{47}$ crystal at bright-atom contrast condition in $[1\bar{1}00]$ direction. Left-up inset is the magnified lattice image with base vectors $(\vec{x}_1, \vec{x}_2)$. The right inset is the Fourier transform of the image. Region A is chosen as the reference lattice. Region B and C are used for determination of specimen thicknesses, respectively.

two non-collinear base vectors, $\vec{x}_1$ (horizontally) and $\vec{x}_2$ (vertically), which are shown in the left-up inset with $|\vec{x}_1| = d_{\bar{1}\bar{1}20}$=1.62 Å and $|\vec{x}_2| = d_{0002} = 2.60$ Å, respectively.

Comparing the reconstructed exit-plane electron wave with the simulated wave of the region B at the basal IDB, specimen thickness and crystal tilt are determined with $t = 3.4 \pm 0.25$ nm and $\tau = (-0.5 \pm 0.1°, -1.0 \pm 0.1°)$, respectively (see details in sec.10.1).

Using 'peak-finding' method in real space or geometric phase analysis (GPA) in Fourier space offered by the Digital Analysis of Lattice Images (DALI) algorithm [40], two dimensional (2D) lattice displacement and the strain of the $In_2O_3(ZnO)_{47}$ compounds in $[1\bar{1}00]$ zone axis can be measured.

9.1 Displacement field measurement by the 'peak finding' method

For a sufficiently thin sample, at bright-atom contrast condition, bright contrast of TEM images are directly interpretable as projected potentials of the atom columns. The 'peak-finding' method from 'DALI' algorithm [40] is now used for precise determination of the atom positions, hence, the displacement fields and the strain fields. This is a unique method to obtain the local structural properties of materials at atomic resolution.

To enhance signal to noise ratio, noise reduction to HR-TEM images is necessary. In the mean time, the noise reduction should prevent subtraction of information from small lattice distorted regions which produce small signals near Bragg reflections in Fourier space. An adaptive Wiener type filter was used by the estimation of the local noise level in the FFT image before maximum localization [37,40,152]. Fig.9-2 is the noise-reduced image, which exhibits smoothened feature around the maximum positions of the metal atom columns with bright contrast.

Applying polynomial fitting along four different directions offered by the 'DALI' algorithm, the maxima positions of the atom columns of a noise-reduced image are detected, with a typical accuracy of 0.03 Å. With two chosen base vectors, $\vec{x}_1$ (horizontally) and $\vec{x}_2$ (vertically), metal atom columns are assigned with coordinates.

The selected region A (fig.9-1) acts as the reference lattice (with reference grid $\vec{r}_0\left(x_1^0, x_2^0\right)$). The region is chosen in the centre of one ZnO domain, far away from the pyramidal IDBs and the basal IDBs, which can therefore be assumed to have virtually no lattice distortions.

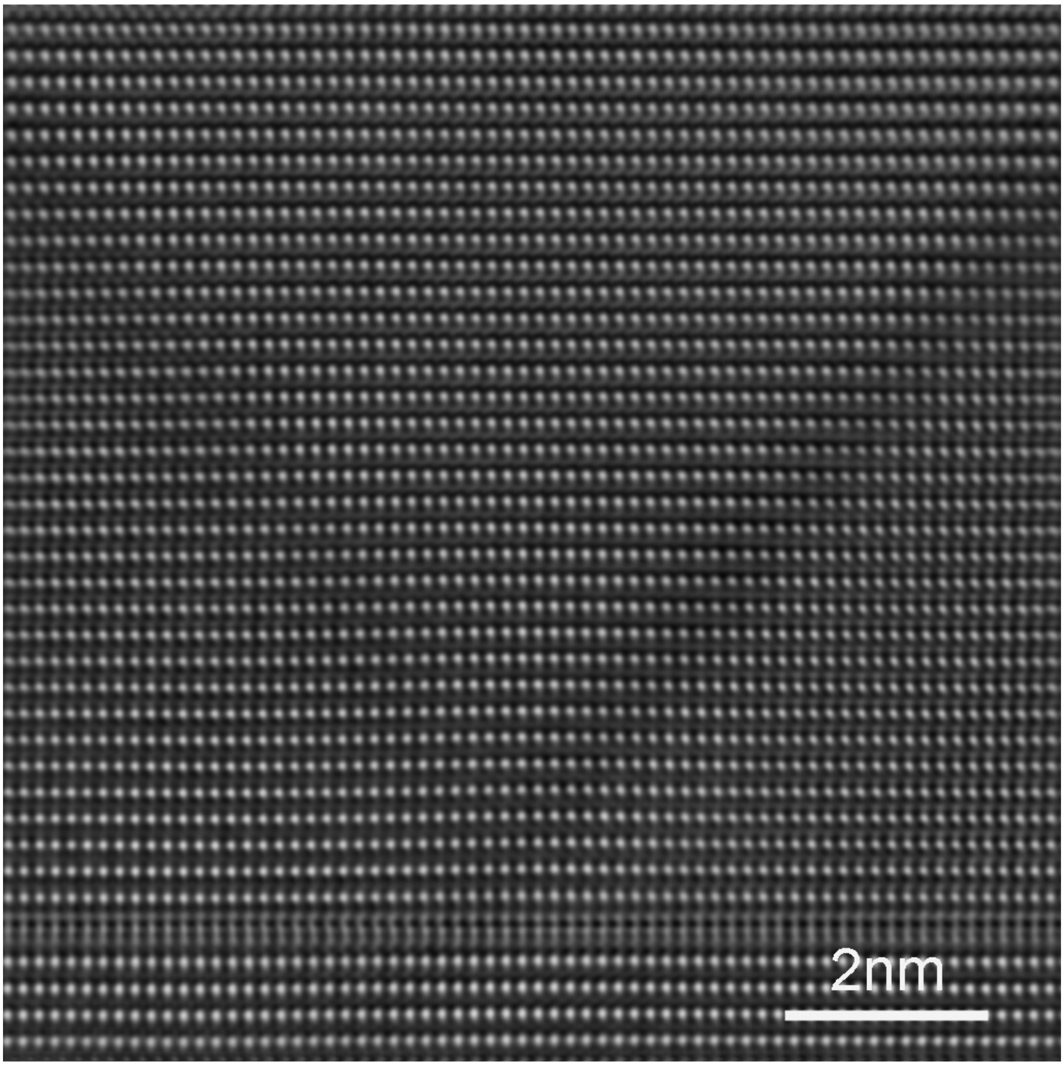

Fig.9-2. Noise-reduced HR-TEM image of a $In_2O_3(ZnO)_{47}$ crystal (fig.9-1) by Wiener filter.

The 2D displacement field $\vec{u}\left(u_1, u_2\right)$ is measured as differences between positions of local atom columns $\vec{r}\left(x_1, x_2\right)$ and the modes of the reference grid $\vec{r}_0\left(x_1^0, x_2^0\right)$. Two components u_1 and u_2 of the displacement field $\vec{u}$ are shown as colour-coded maps in fig.9-3a and fig.9-3b, respectively.

Because there is a structure change of the basal IDB, which is composed of In monolayer in octahedral co-ordinates, it causes virtually a jump (~ 0.5 $|\vec{x}_2|$) of large lattice displacement. Thus, it is meaningless to measure the displacements at the basal IDB and the focus is concentrated on the pyramidal IDBs and ZnO domains.

The displacement component u_1 is displayed in fig.9-3a. It shows clearly that the ZnO domains are displaced and that the displacement is located at the pyramidal IDBs. For the displacement component u_2, small lattice displacement (< 0.05 $|\vec{x}_2|$) at the pyramidal IDBs is observed (fig.9-3b). Though the displacement is close to zero inside ZnO domains, there are residual relaxations of lattice distortion, especially at the region of the joint point of two pyramidal IDBs.

To further quantify the displacement field, two regions (*region1* and *region2*) are chosen to extract displacement profiles shown as dashed boxes fig.9-3a and fig.9-3b, respectively. Profiles of the displacement component u_1, are shown in fig.9-3c and fig.9-3e along direction 1 and 2, respectively. The displacement is mainly concentrated at the regions of the pyramidal IDBs, showing a ‘jump-like’ lattice distortion over 4 atom columns. The displacement at the pyramidal IDB can be estimated to be: $(0.34 \pm 0.04) \cdot |\vec{x}_1|$. Inside ZnO domains, however, relaxation of lattice of component u_1 is observed along direction 2. Fig.9-3d and fig.9-3f are profiles of the displacement component u_2 along direction 1 and 2, respectively. Only small displacement at the pyramidal IDB is found along $\vec{x}_2$, given by $(0.06 \pm 0.02) \cdot |\vec{x}_2|$. Thus, the displacement field at the right pyramidal IDB can be estimated to be: $\vec{u} = (0.34 \pm 0.04) \cdot \vec{x}_1 + (0.06 \pm 0.02) \cdot \vec{x}_2$. Substituting the absolute value of the base vectors, the displacement at the right pyramidal IDB can be quantified with: $\vec{u} \approx (0.55 \pm 0.06)_{horizontal} + (0.16 \pm 0.06)_{vertical}$ Å.

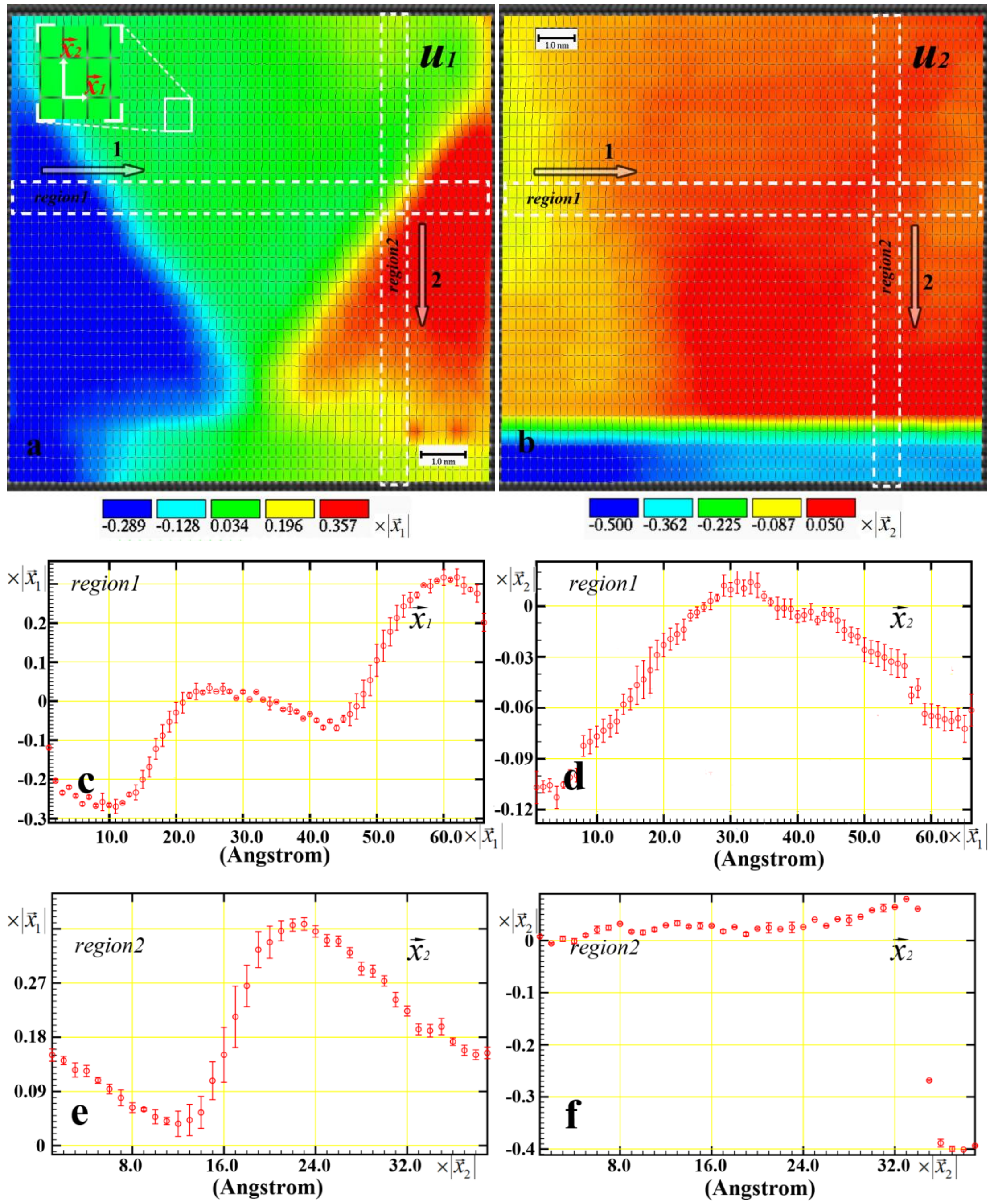

Fig.9-3. Displacement field component u_1 (a), profiles along direction 1 (c) and direction 2 (e). Displacement field component u_2 (b), profiles along direction 1 (d) and direction 2 (f).

9.1.1 Error analysis

From the focal series reconstruction, the specimen thickness t and the tilts τ of region C (selected in fig.9-1) at the basal IDB are estimated with $t = 3.4 \pm 0.25$ nm and $\tau = (-0.5 \pm 0.1°, -1.0 \pm 0.1°)$. The mean value of defocus of the imaged region is estimated to be Z = 5.9 nm. Properties of the lattice displacement might be influenced by specimen thickness variations, crystal tilts and defocus From the observed result that the displacement component u_1 is prominent with a value of ca. 0.55 Å at the pyramidal IDBs, the position change of contrast maxima only along the direction of $\vec{x}_1$ needs to be investigated and is described in the following.

9.1.1.1 Specimen thickness

For HR-TEM studies, the field of view is sufficiently small that the thin imaged region can be assumed to have the same crystal tilt $\tau = (-0.5\pm0.1°, -1.0\pm0.1°)$, however, there are thickness variations.

To study atomic shifts as a function of specimen thickness t in high resolution images of ZnO in $[1\bar{1}00]$ zone axis, images are simulated at the bright-atom contrast condition (fig.9-4). No contrast reversal is observed within the thickness range of $1.1 \le t \le 7.3$ nm. Comparison with the projected potential shows that the bright contrast of the simulated images is exclusively produced by Zn atom columns.

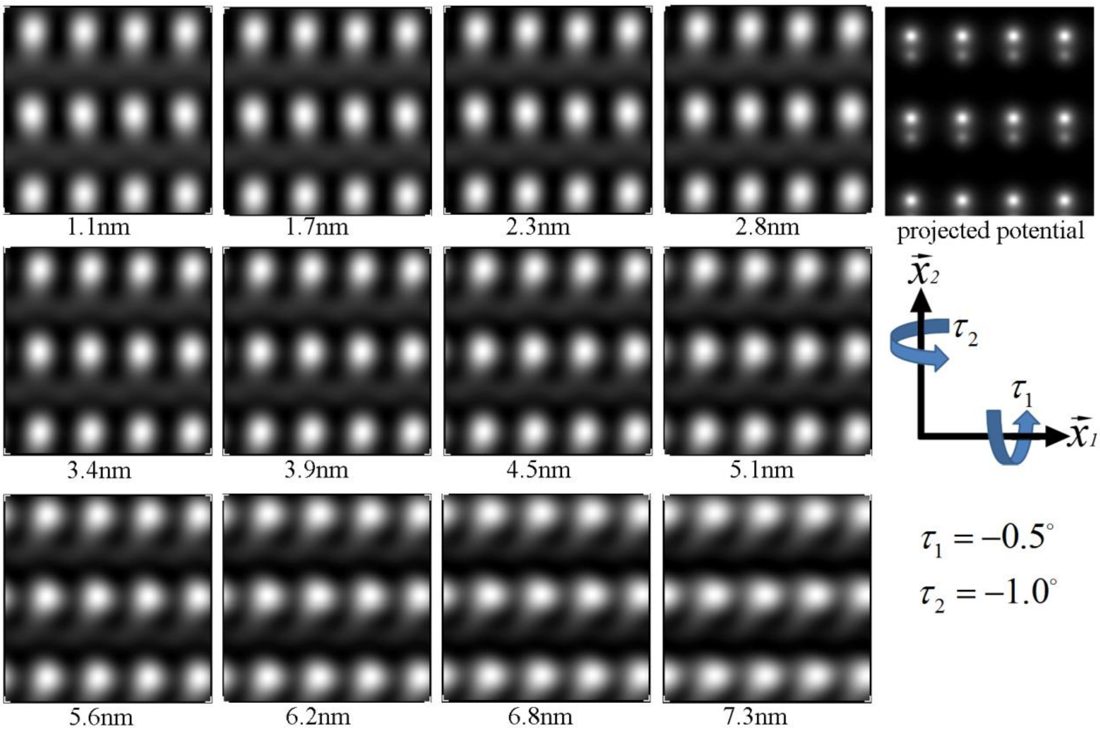

Fig.9-4. Simulated images of ZnO in $[1\bar{1}00]$ zone axis with different specimen thicknesses. The projected potential of ZnO is shown on the right.

From the selected regions (region B and region C) in fig.9-2, specimen thicknesses are estimated to be $t_1 = (3.4 \pm 0.25)$ nm and $t_2 = (4.5 \pm 0.5)$ nm, respectively. From the simulated images, the thickness variation of (1.1 ± 0.5) nm causes a positional change of contrast maxima of about $d_1 = (0.102 \pm 0.061)$ Å along $\vec{x}_1$.

9.1.1.2 Defocus

Though the mean value of defocus is estimated (fig.9-1), there might exist small defocus variations within the imaged region. Assuming the entrance plane of the wedge shaped specimen is normal to the electron beam, it causes defocus variation of ca. (1.1 ± 0.55) nm from the determined thicknesses of the two selected regions in fig.9-1 (region B and region C). From the measured projected distance $l = 6.1$ nm between region B and region C, additional defocus variation of ca. 0.2 nm is obtained by considering the tilt of specimen holder of max. 2°. Compared to the defocus variation caused by different thicknesses, the effect by specimen tilt can be neglected.

At specimen thickness t of 4.5 nm, images of ZnO were simulated with variations of defocus ($4.8 \leq Z \leq 7.0$ nm). The results (fig.9-5) show that there is only a shift of atom columns of (0.041 ± 0.020) Å along $\vec{x}_1$.

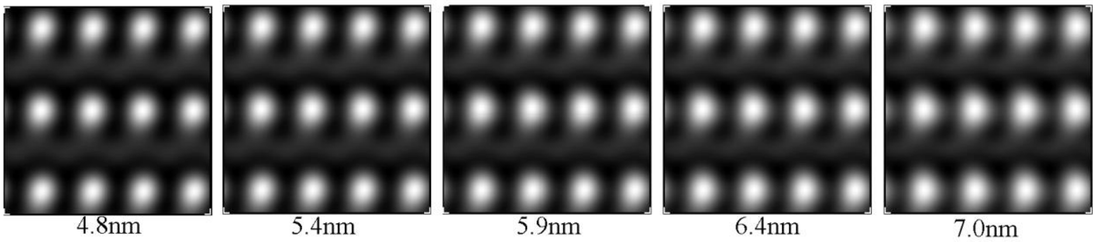

Fig.9-5. Simulated images of ZnO with different defocus ($4.8 \leq Z \leq 7.0$ nm) in $[1\bar{1}00]$ zone axis at thickness $t = 4.5$ nm.

9.1.1.3 Crystal tilt

Furthermore, contrast maxima might also be altered by bending of the crystal. Images of ZnO in $[1\bar{1}00]$ zone axis, at specimen thickness t of 4.5 nm, are simulated with a range of crystal tilts, given by: $\tau = (-0.4^\circ/-0.6^\circ,\ -0.9^\circ/-1.1^\circ)$ (fig.9-6). Positional change of contrast maxima are extracted from the simulated images, which amount to only ca. (0.061 $\pm$0.020) Å along $\vec{x}_1$.

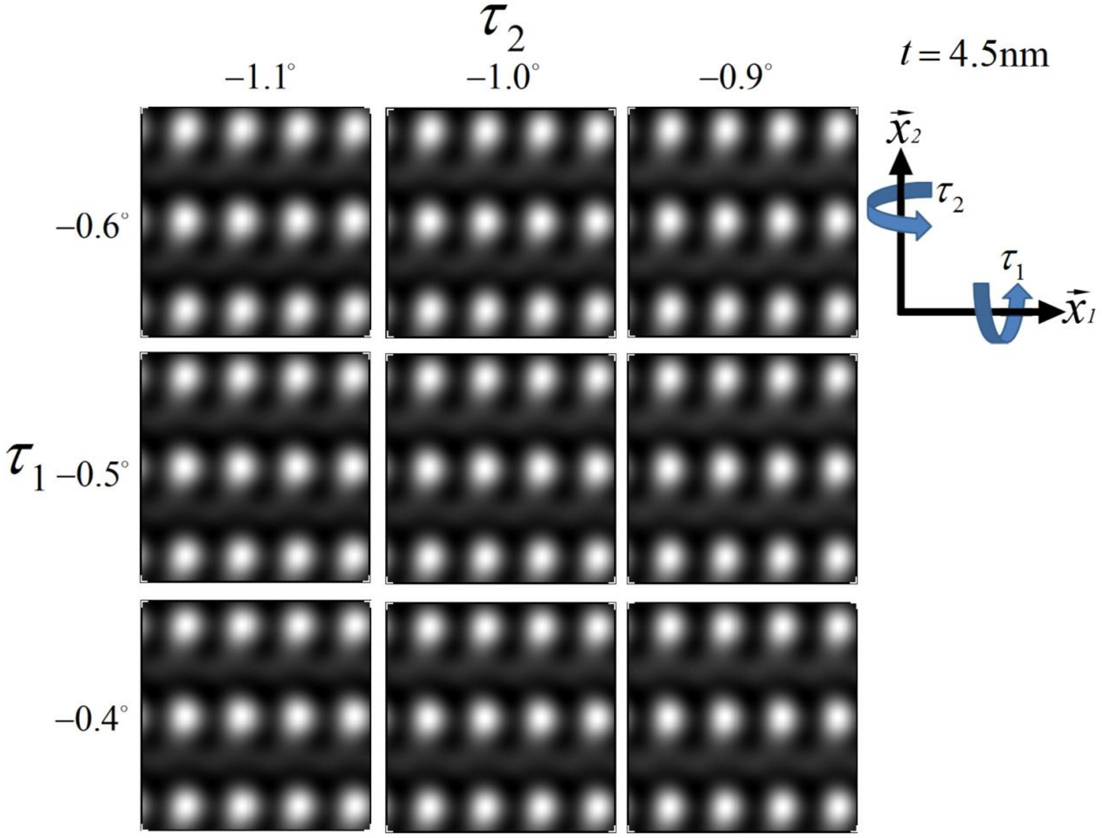

Fig.9-6. Simulated images of ZnO with different tilts τ $(-0.4^\circ/-0.6^\circ,\ -0.9^\circ/-1.1^\circ)$ in $[1\bar{1}00]$ zone axis.

Through image simulations, positional changes of contrast maxima caused by variations of specimen thickness, defocus and crystal tilt are discussed. They might induce an additional error of maximum (0.126 $\pm$0.067) Å along $\vec{x}_1$, which is comparable to the pixel size about of 0.1024 Å of the recorded TEM image (fig.9-1). Finally, the lattice displacement component u_1 can be estimated as (0.55 $\pm$0.13) Å.

9.2 The strain field

The strain is a tensor, which is the gradient of the 2D displacement field $\vec{u}$, consisting of four components: the diagonal components (e_{11} and e_{22}) and the off-diagonal components (e_{12} and e_{21}), representing as a 2×2 matrix: $e=\begin{pmatrix} e_{11} & e_{12} \\ e_{21} & e_{22} \end{pmatrix}$.

A complete description of the 2D strain can be separated into two terms: the symmetric term ε (eq.3.21a) and the anti-symmetric term ω (eq.3.21b), which indicate local tetragonality and rotation of the lattice with respect to the un-distorted lattice. These two terms of the strain field are displayed in fig.9-7 and fig.9-9, respectively.

The symmetric term of the strain is displayed in fig.9-7. In order to see the strain at the pyramidal IDBs more explicitly, its scaling is chosen within a range of lattice distortion about ±5%. Due to structural change of the basal IDB with lattice distortion over 30% along $\vec{x}_2$, the strain component ε_{22} at the basal IDB is not displaced. The four components of the strain are close to zero inside the ZnO domains, which are displayed in green. The diagonal element ε_{11} (fig.9-7a) presents a dilatation of the lattice mainly at the pyramidal IDBs along $\vec{x}_1$. Its line profiles (fig.9-8a and fig.9-8c) within the *region1* and the *region2*, respectively, exhibit max. $(4\pm0.8)\%$ lattice distortion along $\vec{x}_1$. However, lattice distortion along $\vec{x}_2$ is close to zero, which are shown in fig.9-8b and fig.9-8d, within the *region1* and the *region2* (fig.9-7d), respectively.

The off-diagonal elements, ε_{12} and ε_{21}, correspond to a shear of the lattice and their values are quite small (less than 1%) on average. However, they display opposite signs at both sides of the pyramidal IDBs.

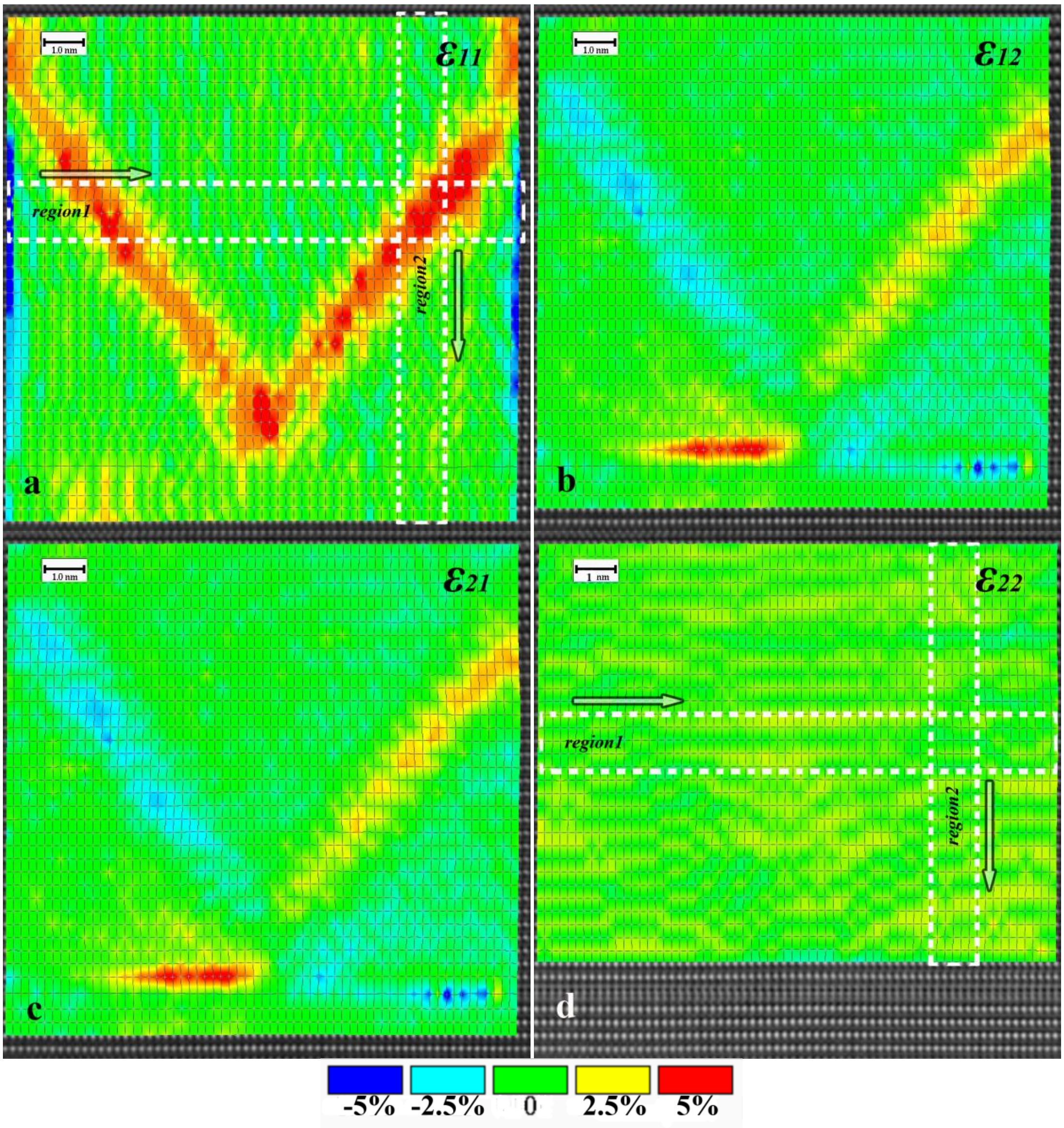

Fig.9-7. Symmetric term of the strain with four components shown in (a) – (d), respectively. The diagonal components ε_{11} and ε_{22} represent the dilatation/compression of the lattice in $\vec{x}_1$ and $\vec{x}_2$, respectively. The off-diagonal elements ε_{12} and ε_{21} correspond to a shear of the lattice.

The anti-symmetric term of the strain is shown in fig.9-9. The diagonal elements (ω_{11} and ω_{22}) are defined to be zero. The off-diagonal elements (ω_{12} and ω_{21}) correspond to a rotation of the lattice. For small values, the rotation angle α in radians can be approximated to be the value of the off-diagonal element, ω_{12}, $(\boldsymbol{\tan\alpha \approx \alpha})$, with a lattice rotation of $(1.9 \pm 0.3)^{\circ}$ at the pyramidal IDB from the left ZnO domain to the middle one. The lattice rotates with an opposite sign across the right pyramidal IDB, resulting in the mirror symmetry at the pyramidal IDBs.

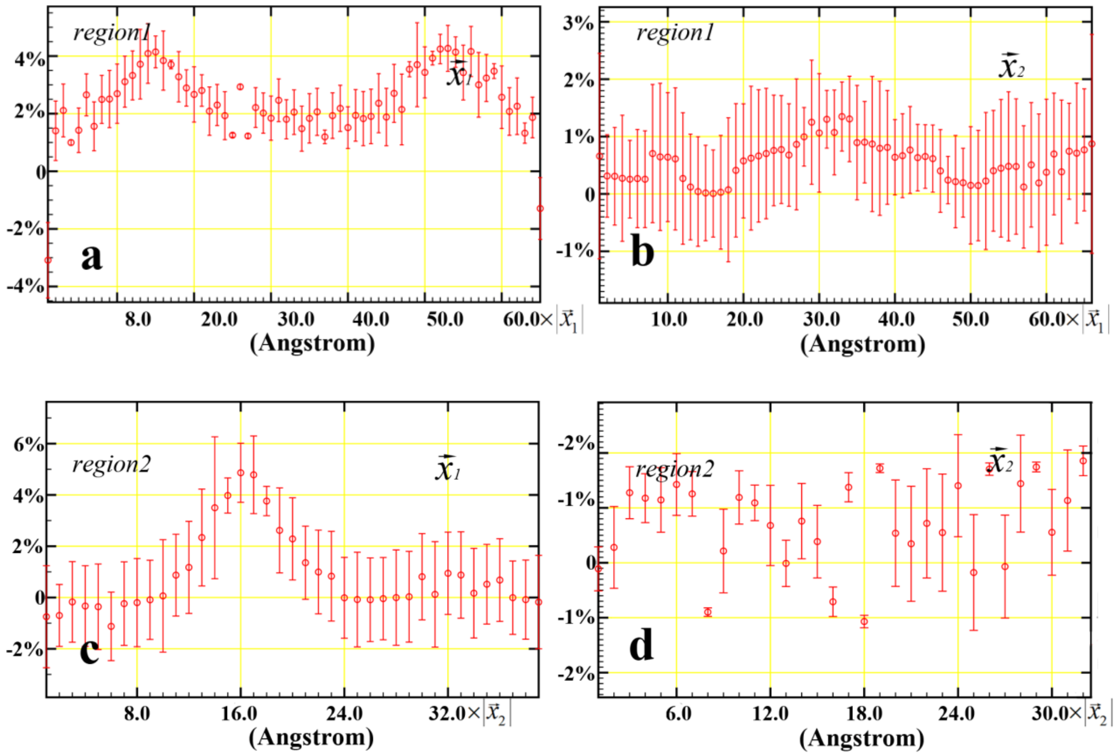

Fig.9-8. Strain profiles in the two regions, *1* and *2* (selected in fig.9-7), showing lattice dilatation/ compression along $\vec{x}_1$ (a+c), and, along $\vec{x}_2$ (b+d), respectively.

Additionally, small crystal tilt variations at the basal IDB are observed. Possible reasons might be the bending of the specimen at extremely thin thickness, which will be discussed in details in sec.10.1.4, or incorrect determination of atom positions due to low contrast of atom columns.

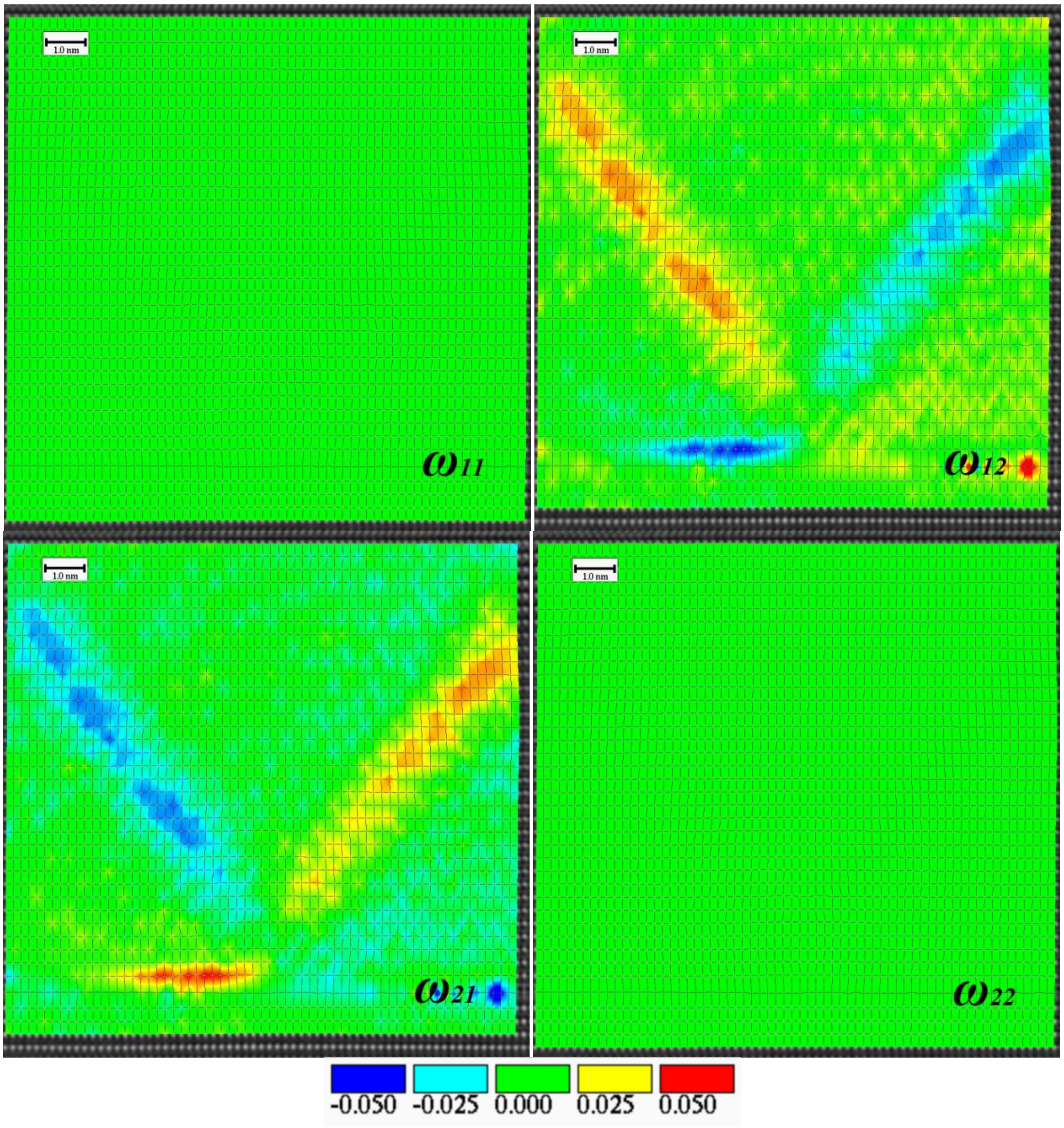

Fig.9-9. Anti-symmetric term of the strain. The diagonal elements (ω_{11} and ω_{22}) are equal to zero shown in green. The off-diagonal elements (ω_{12} and ω_{21}) represent rotation of the lattice at the pyramidal IDBs, respectively.

9.3 Determination of the local lattice distortion by GPA

The diagonal components of the strain field, e_{11} and e_{22}, can also be quantified by the GPA method. Contrary to the 'peak finding' method, the GPA method analyzes local lattice distortion in the HR-TEM images from the spatial frequency components in Fourier space.

A 2D power spectrum is first calculated by Fourier transformation. In the resulting Fourier image (corresponds to diffraction pattern), two Bragg reflections: $g_{\bar{1}\bar{1}20}$ and g_{0002} are chosen. For each of them, small region around the chosen Brag reflection is selected and then Fourier transformed to real space. The resulting images are shown in fig.9-10a and fig.9-10b, respectively. The lattice distortions can be observed of the Bragg-filtered images by naked eye, which are mainly at the pyramidal IDBs.

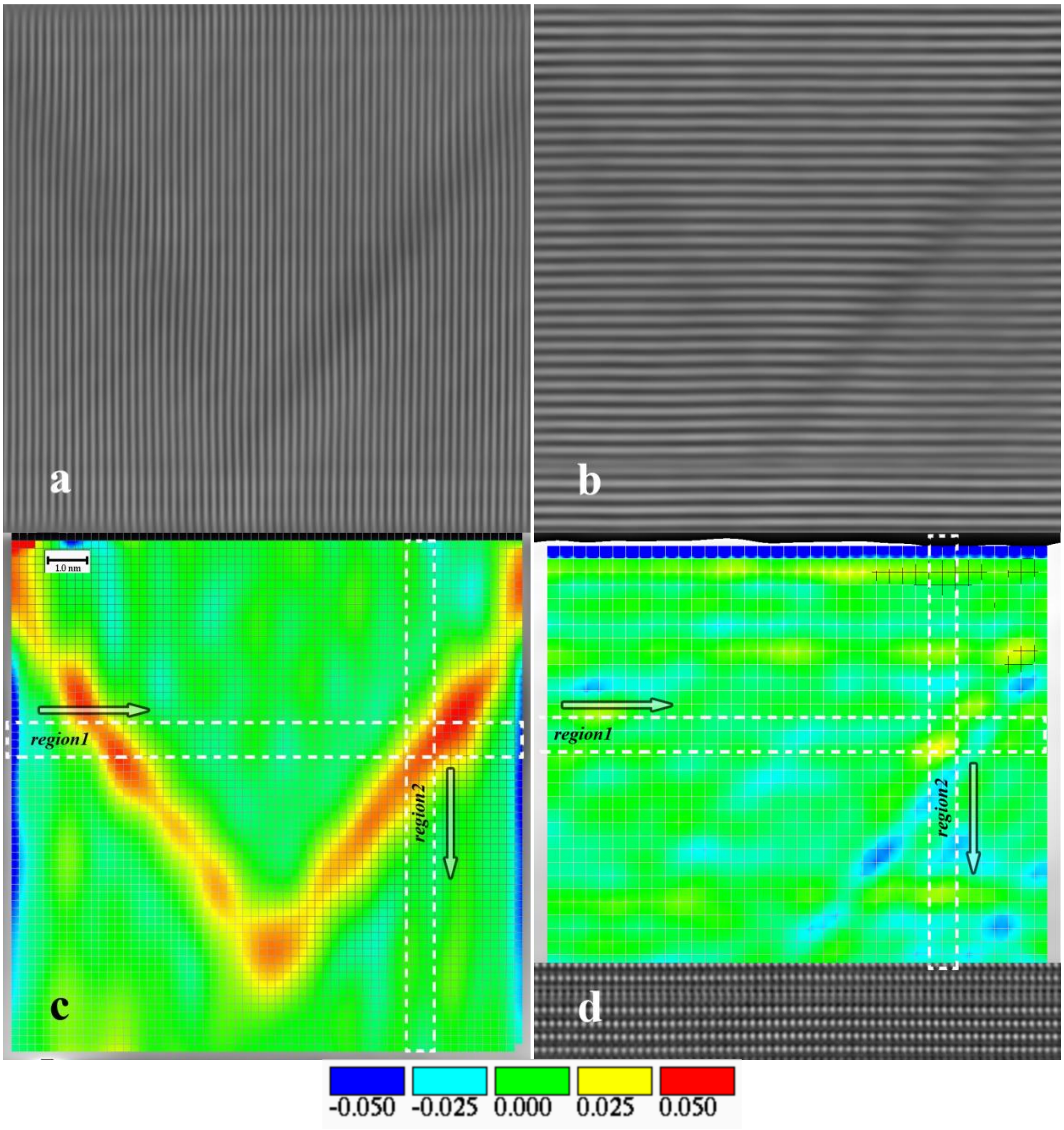

Fig.9-10. Bragg-filtered images for reflection $g_{\bar{1}\bar{1}20}$ (a) and g_{0002} (b), respectively. The relative lattice variations are mapped along $\vec{x}_1$ (c) and along $\vec{x}_2$ (d), respectively.

Using the GPA algorithm, the phase of the lattice fringes as a function of positions in the image is determined and lattice distortions can be mapped (see in fig.9-10c and fig.9-10d), which are the tetragonal elements of the 2D strain field, e_{11} and e_{22}. Similar to the displacement field and strain filed analysis by the 'peak-finding' method, lattice variations can also quantified by the GPA algorithm. Two regions (*region1* and *region2*) are chosen. Fig.9-11a - fig.9-11d are profiles along $\vec{x}_1$ and along $\vec{x}_2$ within the two chosen regions (*region 1* and *region2*). The lattice distortion at the right pyramidal IDB can thus be quantified, given by $\left(4\pm0.4\right)\%$ along $\vec{x}_1$. Compared to the result by the 'peak-finding' method, relatively smaller error bars are obtained, which is due to the merit of the adaptive Bragg-filter.

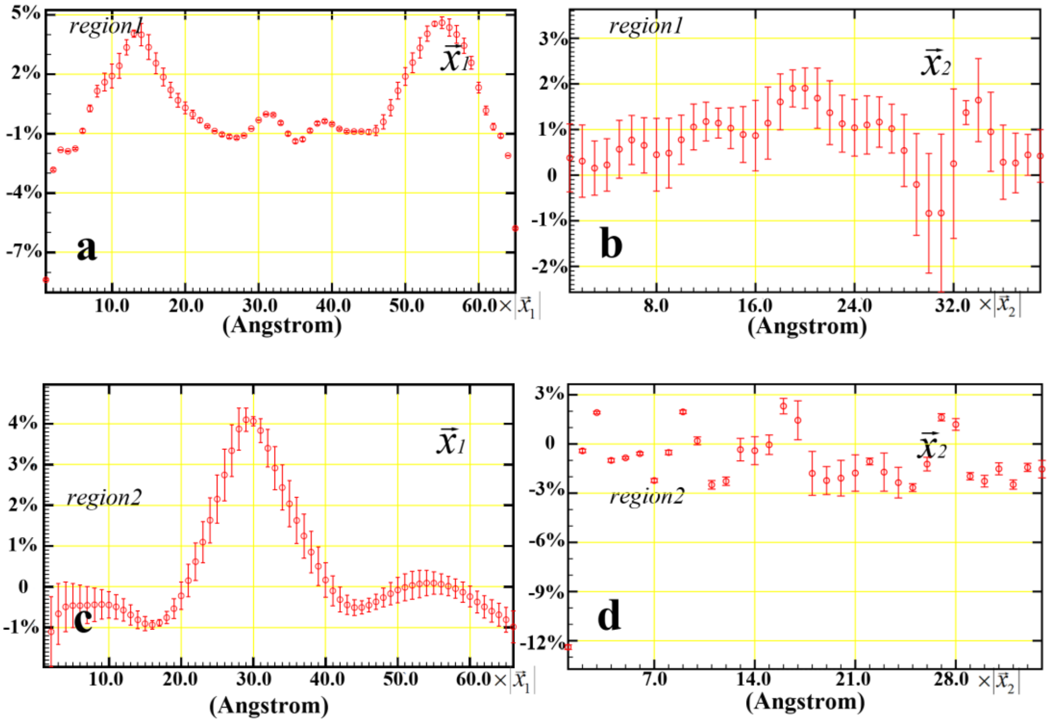

Fig.9-11. Line profiles of the relative lattice variations for the selected regions (*region1* and *region2*) in fig.9-9, are displayed in (a) and (c) along direction $\vec{x}_1$, and, (b) and (d) along direction $\vec{x}_2$, respectively.

Chapter 10 HR-TEM phase imaging

10.1 Structure of the basal IDB

The local structure of the basal IDB is imaged along both zone axes of ZnO, $[1\bar{1}00]$ (*m* axis) and $[2\bar{1}\bar{1}0]$ (*a* axis), respectively. These two zone axes form an angle of 30 °±*n* 60 °by rotation about the c-axis of ZnO (with *n* integer). HR-TEM imaging and focal series reconstruction were used for the structure refinement of the basal IDB.

10.1.1 HR-TEM imaging in both zone axes

Fig.10-1 is a highly magnified image of the basal IDB in the *m* axis from fig.7-4. The projected distance between Zn-Zn atom columns of ~1.6 Å is clearly resolved. The indium atom columns are aligned horizontally in the centre of the image region, denoted by a triangle at the left. Attributed to the negative C_s at the 'bright-atom' contrast condition, the weakly scattering O atoms in the $\left[\mathrm{InO}_{6/3}^{-}\right]_{2}^{\infty}$ octahedral monolayer can be imaged at this zone axis with a projected distance of ~ 1.1 Å.

Focal series images with the basal IDB in the *a* axis were acquired and the exit-plane wave was successfully reconstructed. Fig.10-2a shows the reconstructed phase with the specimen hole near the right-bottom of the image region. In this zone axis, the projected distance between Zn and O atoms is ~ 1.1 Å. Fig.10-2b is the experimental TEM image, at over-focus of ~ 4 nm, within the same region selected in the dashed box in fig.10-2a. From the experimental TEM image, the Zn and O atoms are already resolved (selected in a dashed form in fig.10-2b) and their corresponding intensity line profile is shown in fig.10-2c. At the basal IDB, the projected distances between In and O were measured as projected distance $d_1 = 1.33 \pm 0.10$ Å and $d_2 = 2.15 \pm 0.10$ Å, which are slightly different from the values quantified from powder x-ray diffraction for $m = 5$, with $d_1^* = 1.3797(88)$ Å and $d_2^* = 2.1618(20)$ Å, respectively.

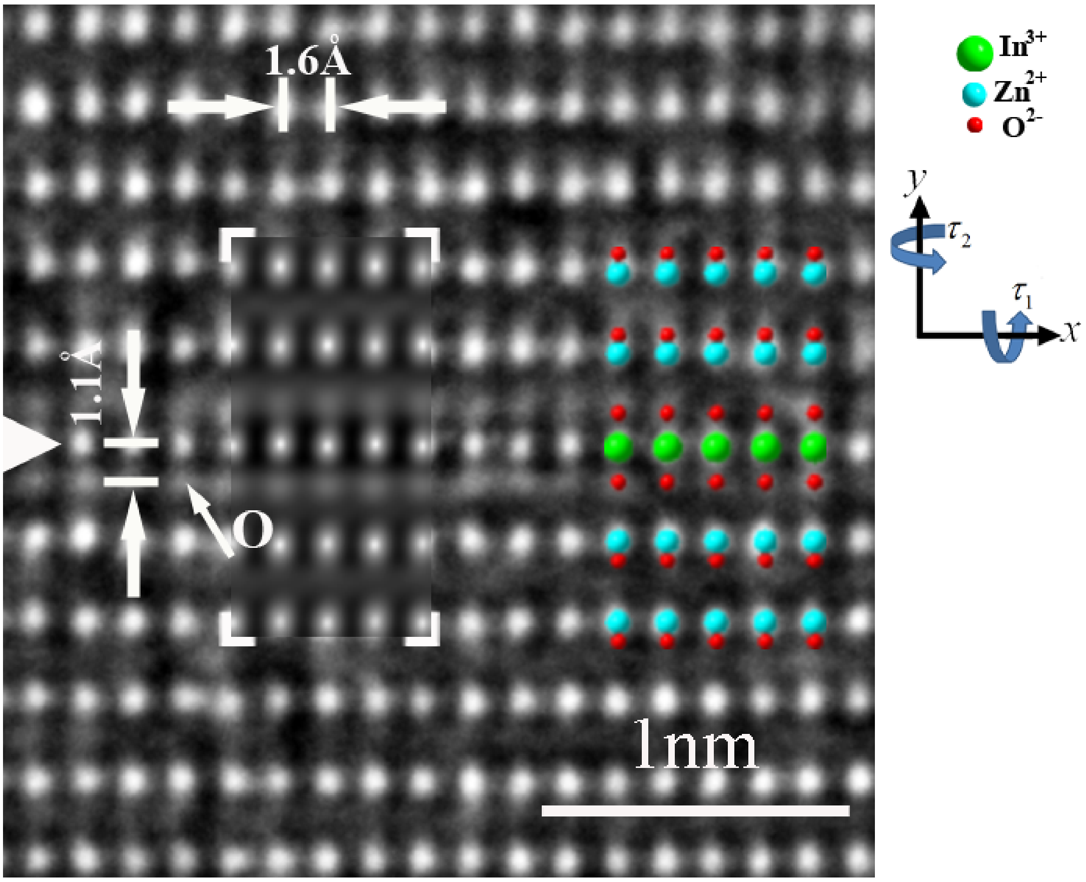

Fig.10-1. HR-TEM image in $[1\bar{1}00]$ zone axis. At the basal IDB, the projected column spacing between In and O atom columns of ~ 1.1 Å is resolved.

10.1.2 Structure model for the basal IDB

Combination of HRTEM imaging in both zone axes proves the presence of a octahedrally coordinated indium monolayer at the basal IDB. A supercell in the *m* axis was generated (fig.10-3) with the indium in octahedral co-ordination as the basal IDB in the middle and two parts of ZnO domains pointing with the c axes towards the octahedral $\left[\mathrm{InO}_{6/3}^{-}\right]_2^{\infty}$ layer. A part of the structure model with 90 °rotation is shown as an inset at the right side of fig.10-1. The dimensions of the supercell are $A = 52.42$ Å, $B = 26.21$ Å and $C = 5.64$ Å, with cell axes parallel to the $[0001]$, $[2\bar{1}\bar{1}0]$ and $[01\bar{1}0]$ directions of ZnO, respectively. Along the *A* direction, the structure is not periodic. Nine Zn-O double layers were constructed on both sides of the Inversion boundary to avoid the interference by the artificial boundaries of the supercell along *A*.

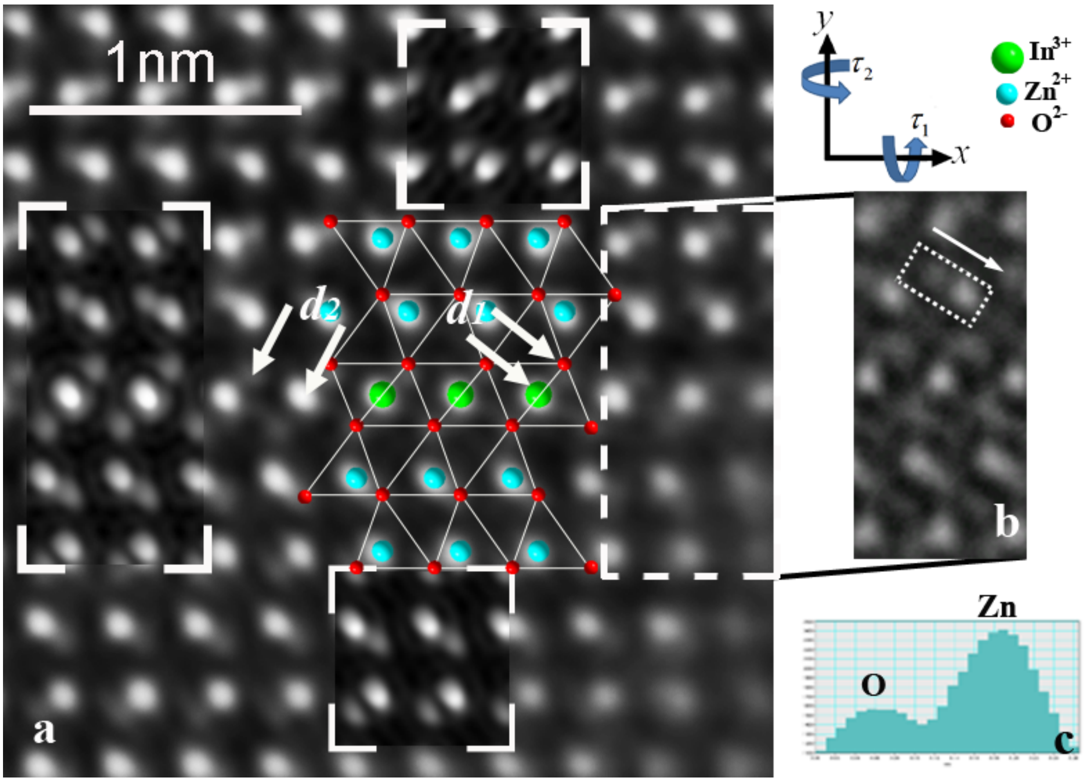

Fig.10-2. (a) Reconstructed phase image viewed in the *a* axis, with the basal IDB aligned horizontally. (b) Experimental TEM image of the same region as selected in the dashed box in (a). (c) Intensity line profile of the Zn and O atoms selected in (b).

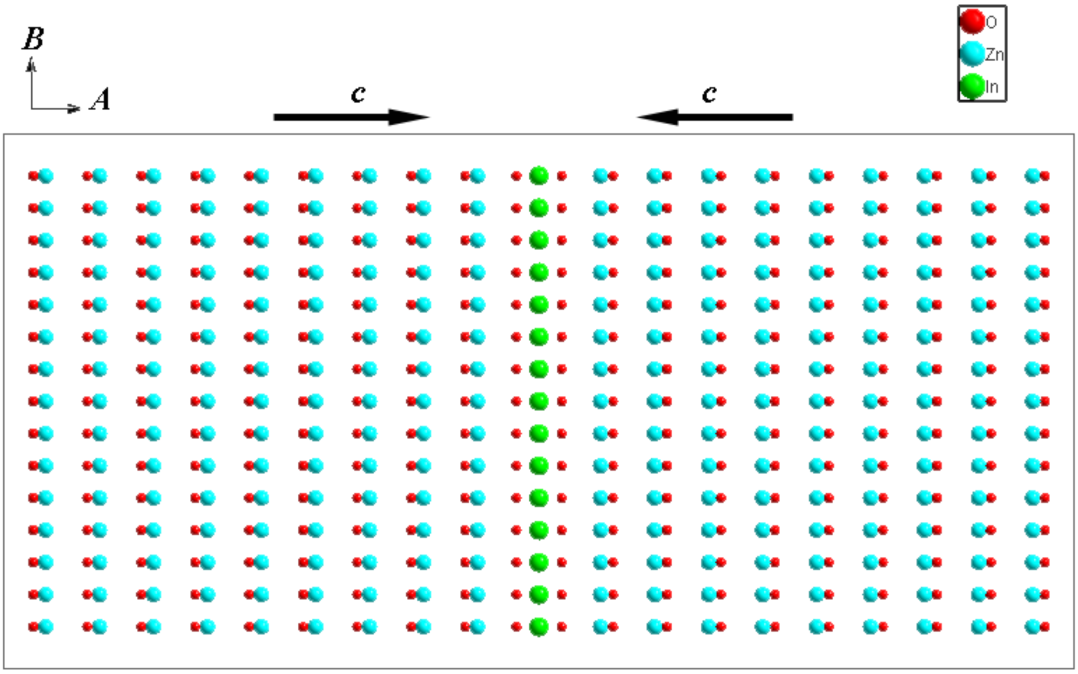

Fig.10-3. Supercell of the basal IDB, with In in octahedral co-ordination in the middle and 9 Zn-O double layers with c axes pointing towards the basal IDB.

10.1.3 Structure refinement of the basal IDB

For image simulations, the incident electron beam was set to be parallel to the *C* direction of the supercell, and the supercell is rotated of about 90 °around *C* axis, resulting in the basal IDB of the superell horizontally. Using the software package 'EWACS', integrated with the EMS package, the sample parameters and the local atom structure can be determined and refined with the highest XCC (cross-correlation coefficients) as parameter for comparison of image intensities.

In principle, the full non-linear (FNL) approximation should be used for the image simulation processes. Due to time consumption, the past-plate (PP) approximation (parabolic method) is preferred for the image simulations, because only small deviations are found between both methods. However, the FNL approximation is used for checking the subtle features of the simulated images afterwards.

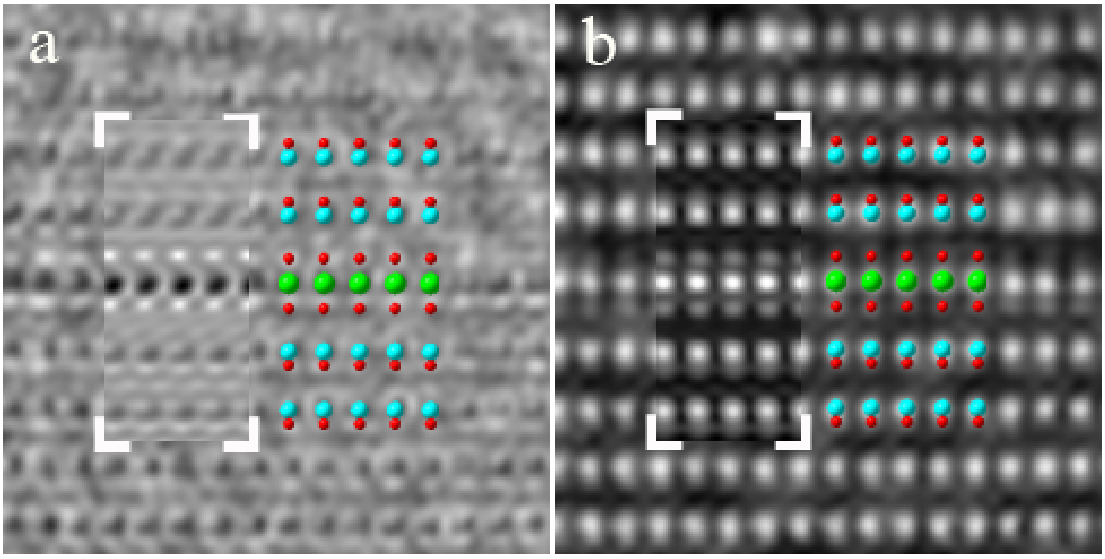

Fig.10-4. Reconstructed amplitude (a) and phase (b) in the *m* axis, with the basal IDB. Structure model and simulated amplitude and phase are superposed.

The simulated image in the *m* axis is superposed on fig.10-1. The sample thickness can be estimated as: (3.4 ±0.25) nm. The specimen tilt is: τ = (-0.5 ±0.1 °, -1.0 ±0.1 °). On the other hand, the exit-plane wave of the basal IDB in this zone axis was reconstructed by focal series reconstruction. The reconstructed amplitude and phase are shown in fig.10-4a and fig.10-4b, respectively. Because the amplitude of the reconstructed exit-plane wave is more sensitive to specimen thickness and tilt than those of the reconstructed phase, the amplitude was used for the determinations of the specimen thickness and specimen tilt. The robust reconstructed phase was used for the refinement of the structure model of the basal IDB.

After the estimation of the slice thickness, a 3D structure model of the basal IDB was first generated from the measured projected distances between the atom columns in the experimental TEM image in the *m* axis (fig.10-1). Based on the structure model, the images and the waves were then simulated. The resulting images and the phases were compared with the experimental images and the reconstructed phases, respectively, based on the XCC coefficients. Choosing different size of the regions, the structure model of the distance between In-In atom columns along the basal planes and the distances between In-O, In-Zn and Zn-Zn atom columns along the prism planes is refined step-by-step. The structure model producing the highest XCC results in the correct structure model (Appendix E). The refined projected distances between the atom columns in the *m* axis are listed in table 10-1.

Zone axis	$[1\bar{1}00]$			
thickness t:	3.4 ± 0.25 nm	$d_{\text{In-O}}$:	1.11 ± 0.10 Å	along prism plane
tilt_1 τ_1:	-0.5 ± 0.1 °	$d_{\text{In-Zn}}$:	3.02 ± 0.05 Å	
tilt_2 τ_2:	-1.0 ± 0.1 °	$d_{\text{Zn-Zn}}$:	2.64 ± 0.05 Å	
		$2{*}d_{\text{In-In}}$:	3.19 ± 0.04 Å	along basal plane
Zone axis	$[2\bar{1}\bar{1}0]$			
Thickness t:	3.2 ± 0.25 nm	$d_{\text{In-In}}$:	2.82 ± 0.05 Å	along basal plane
tilt_1 τ_1:	-1.4 ± 0.1 °			
tilt_2 τ_2:	-1.0 ± 0.1 °			

Table 10-1. Structure determination and the structure refinement in both zone axes.

Because ZnO has a wurzite type structure, it has three equivalent axes of the type $<2\bar{1}\bar{1}0>$. For the image simulations in the *a* axis, we can simply set the incident beam along *B* direction of the supercell. The structure model of the projected distance In-In along the basal plane (which is the proportion to the slice thickness in the *m* axis) were checked and listed in table 10-1. The left inset in fig.10-2 is the simulated phase in the *a* axis.

The simulated images by using the PP approximation and the FNL approximation are compared with the experimental images. The results are nearly the same XCC for both image simulation methods (Appendix F).

10.1.4 Bending of the specimen

The XCC of the simulated and reconstructed waves in the *a* axis is lower than that in the *m* axis. The reason might be the thickness variations and bending of the sample. Because in the *a* axis, the projected distance of ~ 1.1 Å between the Zn-O columns is resolved, it is possible to estimate the thickness and the specimen tilt of the ZnO domains at both sides of the basal IDB separately. By choosing different parts of ZnO domains, the phases of the exit-plane wave are simulated and displayed in the lower (thin part) and upper (thick part) insets (fig.10-2). The parameters were determined and listed in table 10-2, with thickness difference of ~ 0.3 nm and tilt difference of at least 0.3 °.

Thick part:		**Thin part:**	
thickness t:	3.1 ± 0.15 nm	thickness t:	2.8 ± 0.15 nm
tilt_1 τ_1:	-1.3 ± 0.1 °	tilt_1 τ_1:	-1.6 ± 0.1 °
tilt_2 τ_2:	-1.0 ± 0.1 °	tilt_2 τ_2:	-1.0 ± 0.1 °
XCC:	0.897	XCC:	0.902

Table 10-2. Thickness and tilt of two ZnO domains besides the basal IDB.

10.2 Atomic structure of the pyramidal IDB

HR-TEM single-shot images and through-focal series images were successfully taken at the pyramidal IDBs in both zone axes (*m* axis and *a* axis) (see fig.7-4 and fig.7-16). From the observed details at the pyramidal IDBs, the contrast of the weakly scattering O atom columns can be observed and the structure model with In in trigonal bi-pyramidal co-ordination was preferred. Combined with the quantified displacement field, a relaxed structure model of the pyramidal IDB can be proposed.

10.2.1 HR-TEM imaging of the pyramidal IDB in the *m* axis

Fig.10-5 is the TEM image in the *m* orientation with the dashed line indicating the region of the pyramidal IDB. The upper right and the lower left regions are supposed to be two undisturbed ZnO domains, with Zn atom columns of bright contrast. The contrast of the pyramidal IDB is fast straight with a constant angle of ~58 ° (anti-clockwise) to the basal plane.

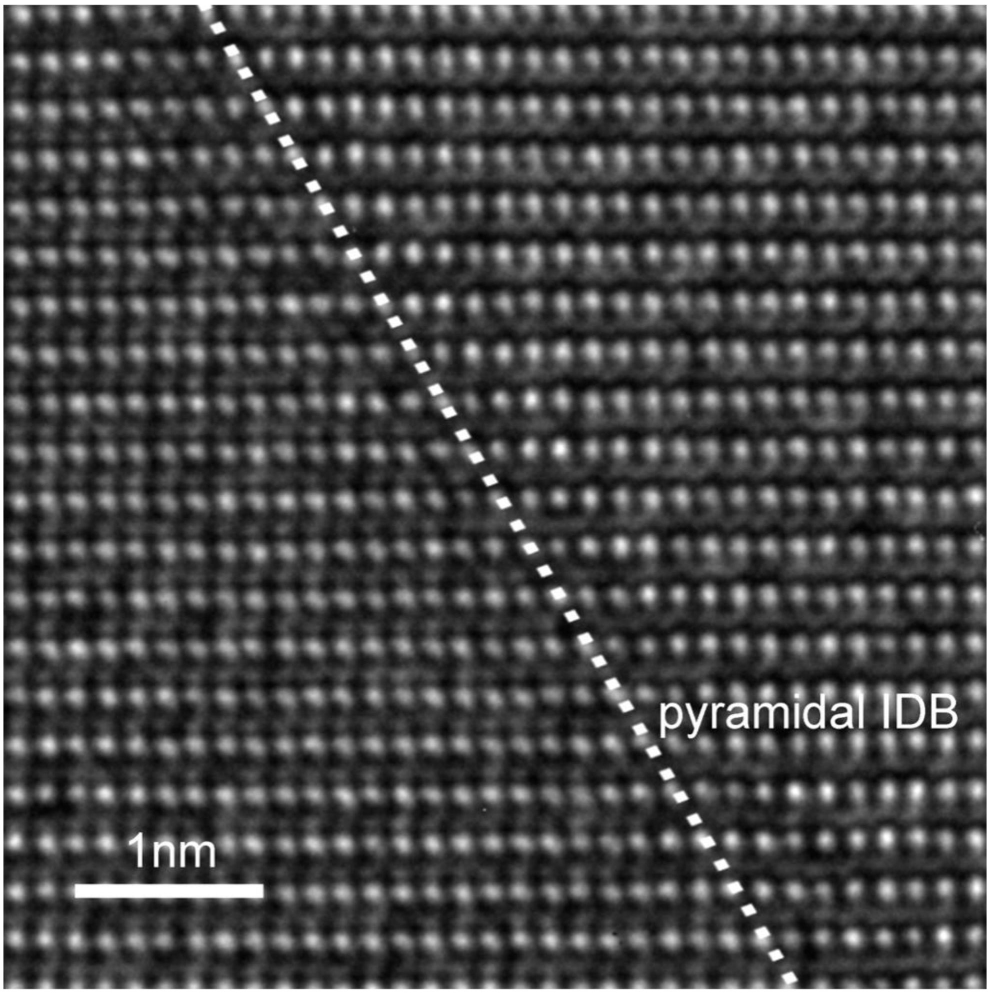

Fig.10-5. HR-TEM image in $[1\bar{1}00]$ zone axis with the region of the pyramidal IDB marked with the dashed line.

10.2.2 Focal series reconstruction of the pyramidal IDB in the *a* axis

The exit-plane wave of the pyramidal IDB in the *a* axis was successfully reconstructed (fig.10-6). The region of the pyramidal IDB is denoted as dotted line. Contrast of the weakly scattering O atom columns is clearly observed inside both ZnO domains, with the projected distance of ~ 1.1 Å between Zn and O atom columns well resolved. From the contrast estimation and the assignment of Zn and O atom columns, small arrows in yellow are drawn pointing the projected directions from the Zn atoms to the O atoms. Along the basal planes from left to right, it is clear that there is a gradual transition of O atom columns across the pyramidal IDB, with the arrow directions from pointing lower right to upper right, superposed to the slight positional change of the metal atom columns. Thus, an inversion of polar *c* axis of the ZnO domains can be directly revealed, which is indicated by two large arrows. Additionally, instead of a clear round-shaped profile, the contrast of the O atom columns at the pyramidal IDB presents elongated profiles, which might be caused by different projected positions of O atom columns in the *a* axis.

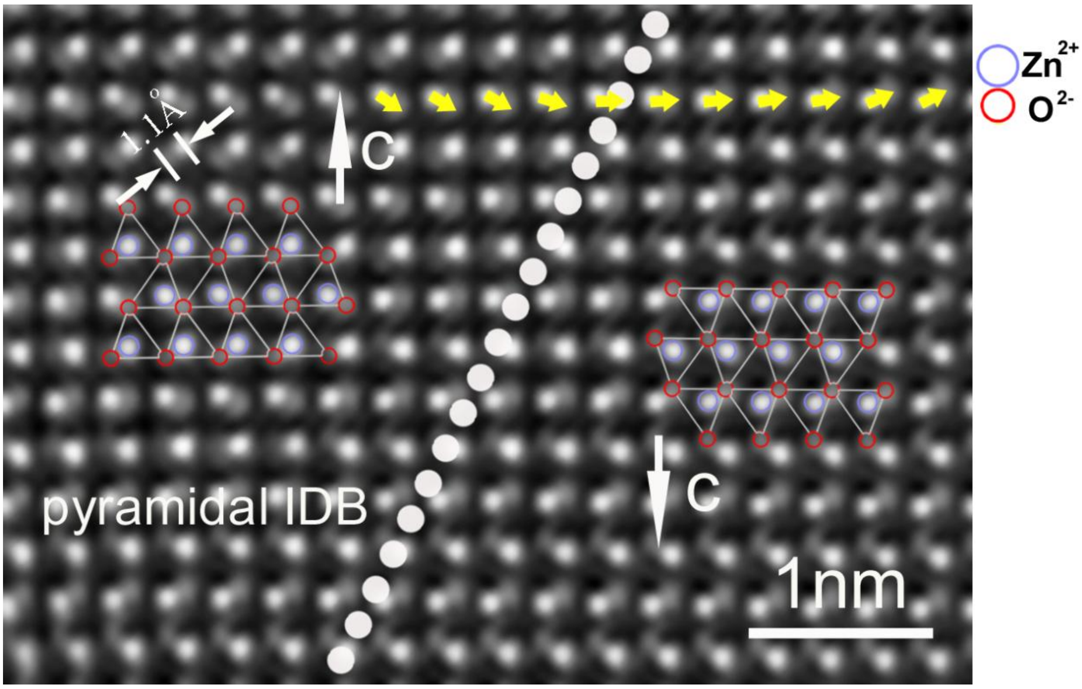

Fig.10-6. Reconstructed phase of the pyramidal IDB in the *a* axis. Contrast of O atom columns can be resolved, together with the relaxation of the atom columns across the pyramidal IDB.

10.2.3 Structure models of the pyramidal IDB

Based on the crystallographic principles and the measured angle between the pyramidal IDB and the basal planes, two rigid-body models at the pyramidal IDB are generated with the O atoms lying straight along the basal planes. Indium atoms at the pyramidal IDBs might be either in octahedral co-ordination or in trigonal bi-pyramidal co-ordination, with the pyramidal IDB connecting the two polar *c* axis inversed ZnO domains in tail-to-tail configuration. Fig.10-7a is the 'octahedral model' with In in octahedral co-ordination. To prevent ‘face-sharing’, additional caution was taken with empty sites at two adjacent atom columns besides the In atom column. Fig.10-7b is a ‘trigonal bi-pyramidal model’ with In in trigonal bi-pyramids, with the occupied and the empty tetrahedrons sharing one basal plane. Thus, the polar *c* axis of ZnO is inverted by shifting the metal atoms through the equatorial plane of the bi-pyramids. However, in the experimental images at the pyramidal IDB, a large shift of contrast at the two adjacent atom columns beside the pyramidal IDBs is not observed. The structure model with In in trigonal bi-pyramidal co-ordination is thus preferred.

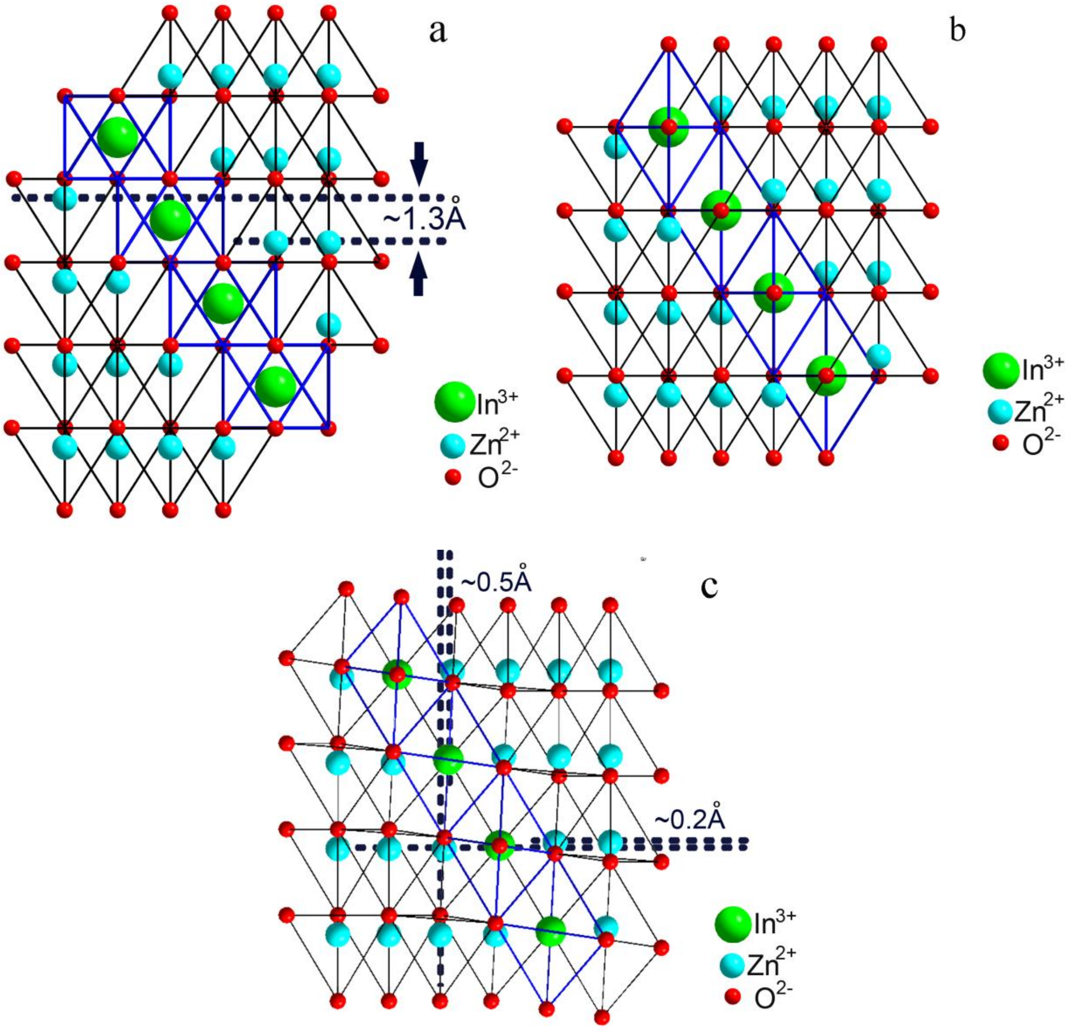

Fig.10-7. Structure models at the pyramidal IDB, with In in octahedral co-ordination (a) and In in trigonal bi-pyramidal co-ordination (b). (c) Relaxed structure model considering the small displacements of the metal atom columns.

Attributed to the improved resolution of the microscopes, clear evidence for the lattice displacements was found and quantified in the *m* axis of ZnO, leading to the bending of type $\{2\bar{1}\bar{1}0\}$ and {0002} lattice planes across the pyramidal IDB with a maximum position shift of metal atoms of about 0.5 Å and 0.2 Å, respectively (chapter 9). Considering the reconstructed phase of the pyramidal IDB in the *a* axis, a relaxed structure model of the pyramidal IDB is proposed (fig.10-6c), with a relaxation of 5 atom columns.

10.2.4 Image simulations of the pyramidal IDBs

Contrary to the contrast at the basal IDB containing only one monolayer, the contrast at the pyramidal IDB in the *m* axis is slightly lower than that of ZnO domains over several atom columns (fig.10-8a). Image simulations are needed to allocate the In atoms. Because the regions with the pyramidal IDB (fig.10-5) is not far away from the region with the basal IDB (fig.7-4), a reasonable approximation is made by assuming both regions having nearly the same specimen thickness and the specimen tilt. Based on the structure model (fig.10-8c) with only one In atom column, a phase image at defocus of ~ 5.9 nm were simulated and displayed in fig.10-8b. Obviously, there is big contrast difference between the experimental image and the simulated image. Fig.10-8d - fig.10-8f are simulated images with different In concentrations within the region of the pyramidal IDB. However, the difference between the resulting simulated phase images was quite small (fig.10-8a - fig.10-8d) (See details in Appendix G). It is not possible simply from phase image in the *m* axis to determine the In concentrations of the pyramidal IDB. On the other hand, in the *a* axis, the pyramidal IDB is inclined to the incident electron beam [131], making it even more difficult to determine the In concentrations and the width of the pyramidal IDB. To solve this problem, the atomically resolved Z-contrast imaging is required for the determination of the atom species at the pyramidal IDB, which will be discussed in chapter 11.

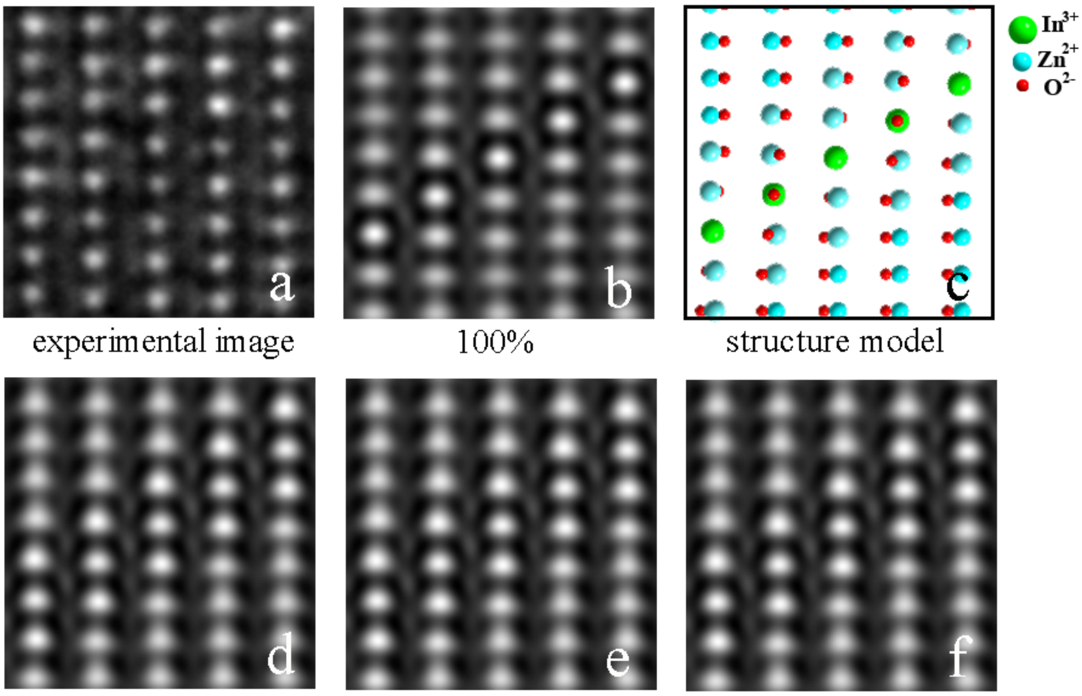

experimental image 100% structure model

33%,33%,33% 25%,50%,25% 10%,20%,40%,20%,10%

Fig.10-8. (a) Experimental image of the pyramidal IDB at the bright-atom contrast condition. (b) Simulated image with only one In atom column at the pyramidal IDB. (c) Structure model of the pyramidal IDB with only one In atom column. (d)-(f) Simulated images of the pyramidal IDB in the *m* axis, under which show the assumed In concentrations.

Chapter 11 Z-Contrast Imaging

As discussed in sec.10.2.4, it is not possible to determine In contents at the pyramidal IDBs by simply analyzing the HR phase-contrast images. It is a challenge to quantify the In contents by EELS, because the In_$M_{4,5}$ edge with an energy loss of ~ 443 eV is quite weak and delayed. Furthermore, the In_L_2 and In_L_3 edges are beyond 3700 eV and produce a signal too low to detect. However, HAADF/STEM imaging offers the possibility to detect and to locate single column at atomic resolution. Contrary to the phase contrast, it is of Z-contrast. By using the probe-side aberration corrected electron microscope, atom columns with spacing of ~ 1.62 Å can be atomically resolved. Because light O atoms do not produce significant contrast, we can assign those HAADF images properly as atomically resolved HAADF images. Atomically resolved HAADF imaging of $In_2O_3(ZnO)_m$ compound in both zone axes of ZnO was achieved. Based on the structure model of the pyramidal IDBs obtained from the phase imaging analysis with In atoms in trigonal bi-pyramidal co-ordination, HAADF images in the *m* axis were simulated with different In contents inside the region of the pyramidal IDB. After comparison with the simulated HAADF images and the experimental ones, the mean In concentration at the pyramidal IDBs can be quantified. Thus, a relative complete description of the 3D atomic structure model of the pyramidal IDBs can be proposed.

11.1 Experimental HAADF imaging and intensity extraction

11.1.1 Experimental HAADF images

11.1.1.1 HR HAADF images of the pyramidal IDB in the *m* axis

After plasma cleaning to remove the hydrocarbon contamination from the TEM sample, the $In_2O_3(ZnO)_m$ compound was conducted on the probe-side aberration corrected FEI Titan 80-300 electron microscope, where a probe of size less than 1 Å can be formed. Because the In atoms have higher atomic number (Z_{In} = 49) than that of Zn atoms ($Z_{Zn} = 30$), the In-rich region should exhibit higher intensity contrast, at nearly zero defocus and homogeneous thickness of the sample. Fig.11-1 shows a HAADF/STEM image of the $In_2O_3(ZnO)_m$ compound in the *m* axis orientation. In this imaged region, the In with relatively higher contrast distributes at the planar Basal IDBs and the zig-zag shaped pyramidal IDBs. With the decrease of the thickness at the lower right of the image, the signal collected by the HAADF detector is lower, resulting in the lower contrast and both types of IDBs being hardly seen.

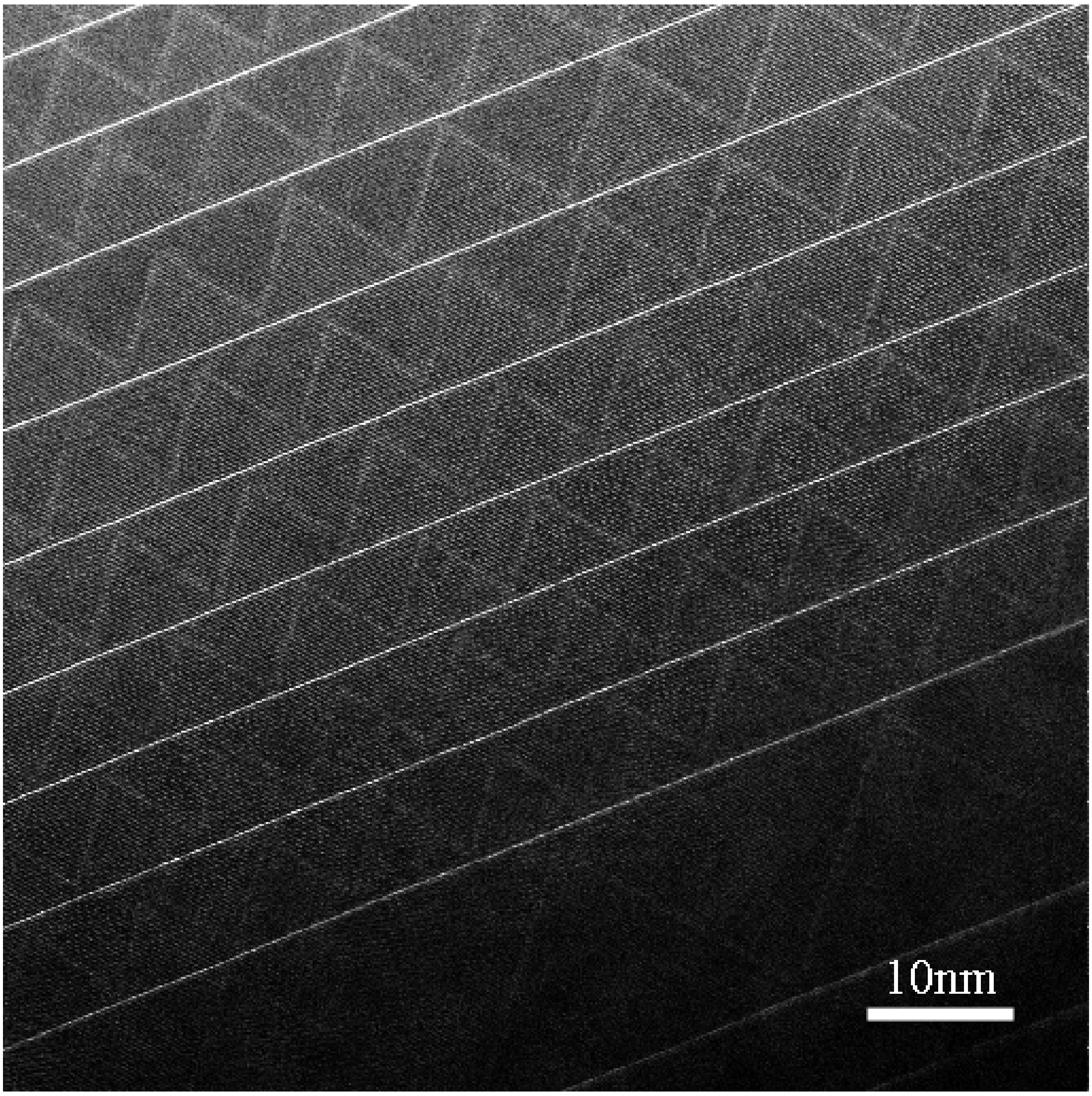

Fig.11-1. HAADF image of $In_2O_3(ZnO)_m$ (m = 30) compound in the *m* axis, which exhibits the In distribution with higher contrast at the basal IDBs and the pyramidal IDBs.

In both zone axes, the HAADF/STEM images with relative larger magnifications are achieved with atom columns along the basal planes resolved, which are displayed in fig.11-2 and fig.11-3, respectively. At the basal IDBs, it does exhibit a close-packed In monolayer with relatively high contrast. However, the contrast at the pyramidal IDBs is much lower compared with that at the basal IDBs. From the determined atomic structure of the pyramidal IDBs, they are inclined in the *a* axis, showing a broadened and lower contrast in fig.11-2. In the *m* axis, the pyramidal IDBs are edge-on and the angles between both sides of the pyramidal IDBs and the basal planes are symmetric amounting to ~ 58 º. The contrast at the pyramidal IDBs shows a width over at least 3 - 4 atom columns (fig.11-3). Because the contrast of the basal IDBs is perfectly straight, the recorded HAADF image (fig.11-3) can be considered without scanning faults and without detectable specimen drift during HAADF imaging. Thus,

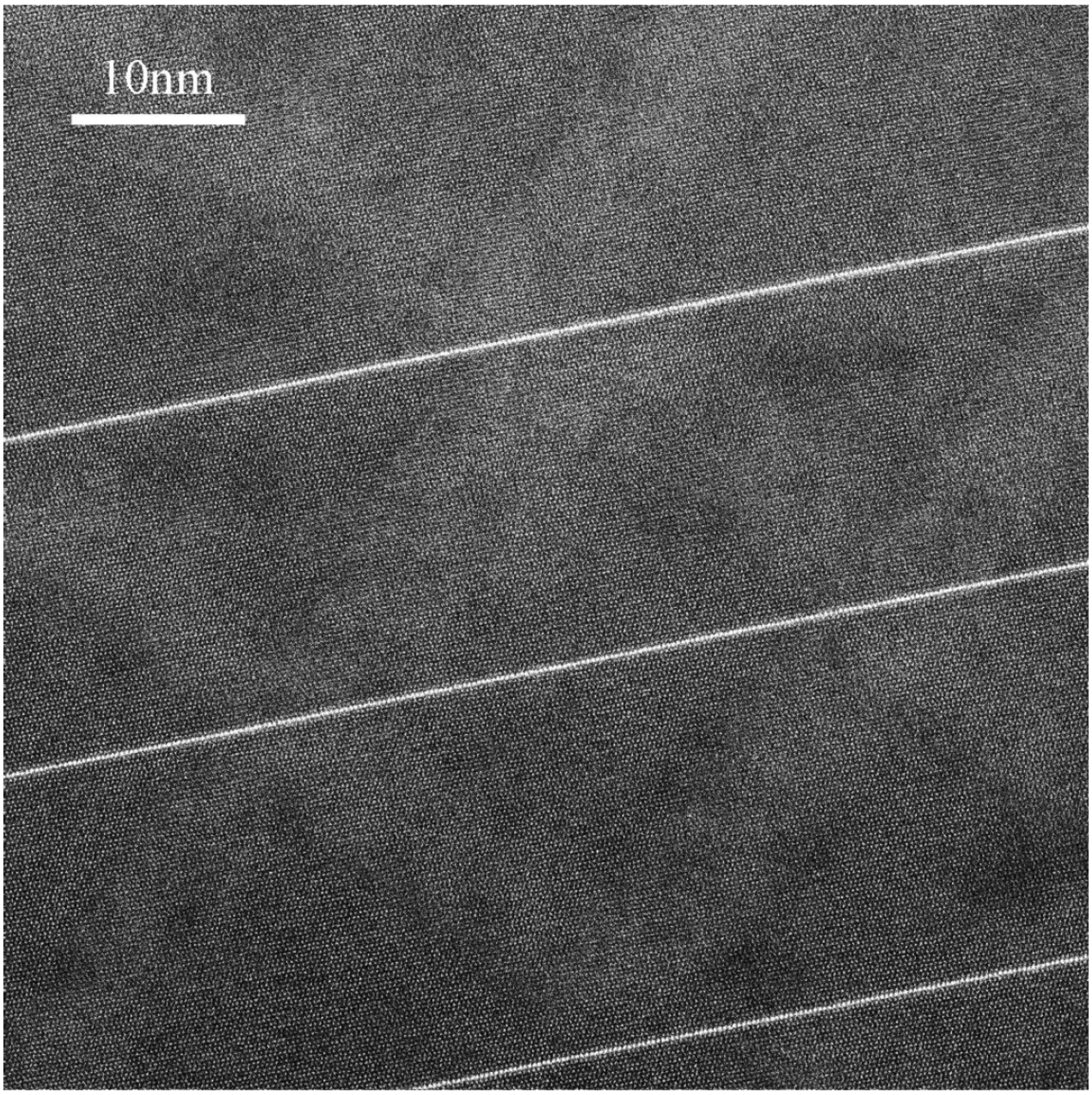

Fig.11-2. HAADF images of $In_2O_3(ZnO)_m$ (m = 80) compound in the *a* axis, with contrast of both types of the IDBs seen.

small displacements at the pyramidal IDB can be directly observed, which is in agreement with the atomically resolved phase contrast imaging analysis.

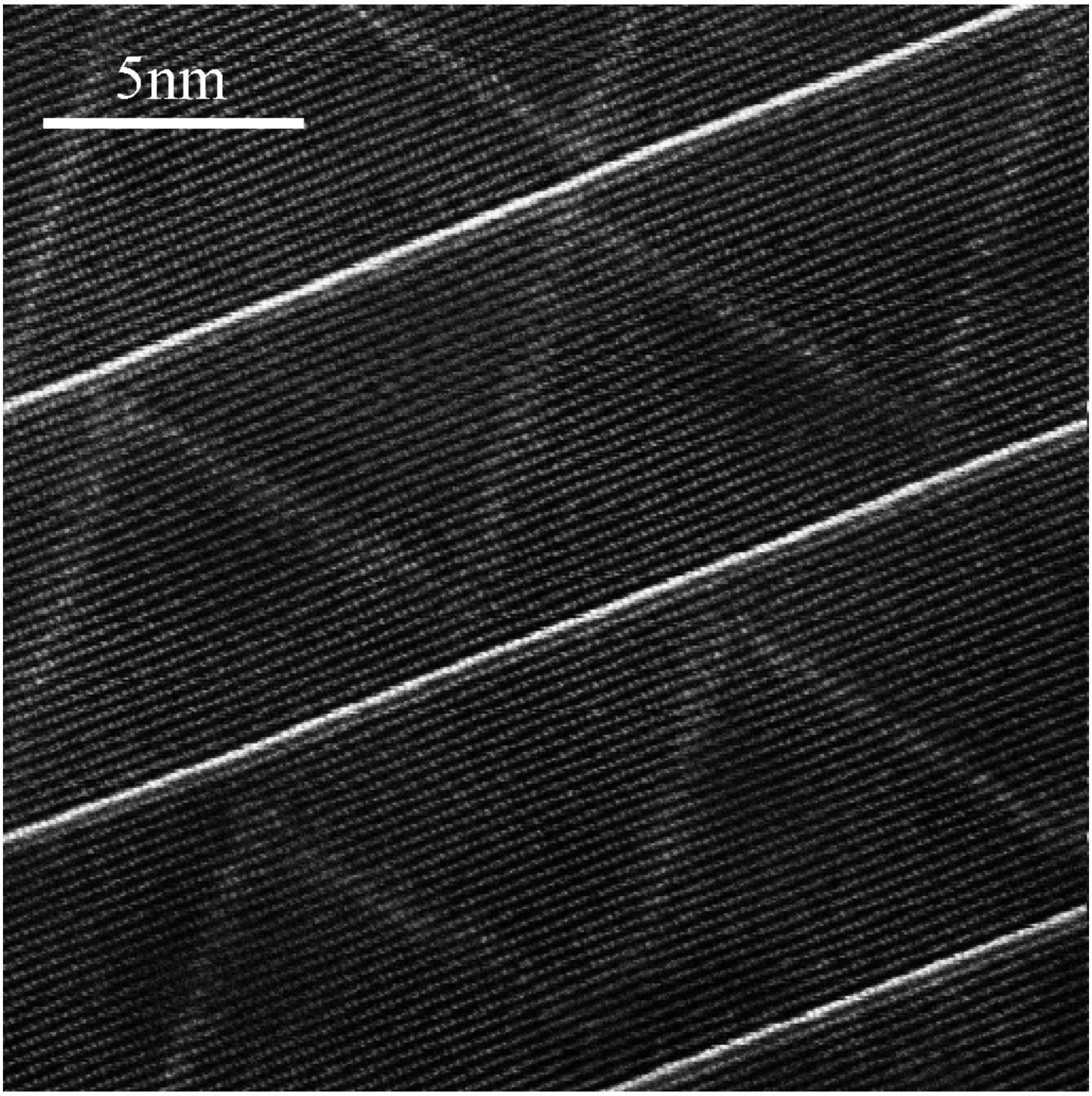

Fig.11-3. HAADF images of $In_2O_3(ZnO)_{30}$ in the *m* axis. The contrast of both types of IDBs can be clearly seen.

11.1.1.2 Atomically resolved HAADF imaging

Atomically resolved HAADF images in both zone axes were achieved and shown in fig.11-4 (*a* axis) and fig.11-6 (*m* axis).

In fig.11-4, Zn atom columns with the column spacing of ~ 2.7 Å along the basal planes are well resolved. The contrast of the basal IDBs containing In monolayers is clearly seen with bright contrast. The magnified inset is a blow-up of the selected region1, at the basal IDB. An atomic structure model of the basal IDB fits the contrast of the metal columns in the HAADF image. However, the contrast of the weak scattering O atoms cannot be imaged.

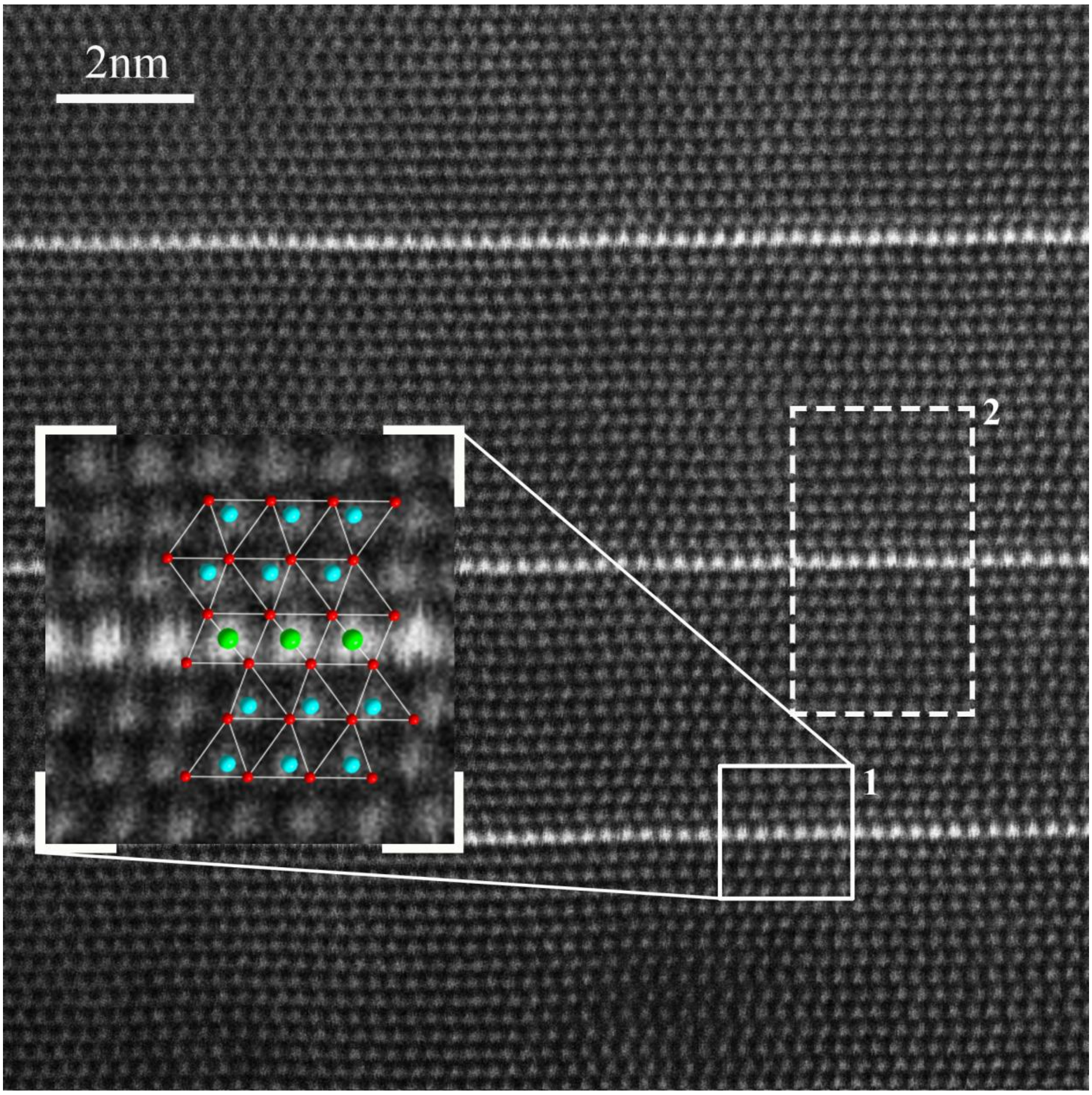

Fig.11-4. Atomically resolved HAADF image of $In_2O_3(ZnO)_m$ (m = 15) in the *a* axis. The large blow-up of the selected region1 fits the atomic structure of the basal IDBs, with In, Zn and O atoms in green, in blue and in red, respectively. Region2 is used for the line profile analysis.

Fig.11-5 is another atomically resolved HAADF image of $In_2O_3(ZnO)_m$ (m = 15) compound in the *a* axis. In atom columns with strong contrast at the basal IDBs can be clearly seen. Slight zig-zag shaped contrast variations inside the ZnO domains are the result of the inclined pyramidal IDBs.

Fig.11-6 is the atomically resolved HAADF image in the *m* axis. From the contrast of the basal IDB being nicely straight, we can neglect the specimen drift and the scanning faults induced during the HAADF image acquisitions, respectively. Lattice distortions can be observed at both sides of the pyramidal IDBs, especially nearly the top of them, which is in agreement with the contrast of HR-TEM images. Compared to the local contrast at the basal IDBs, the contrast at the pyramidal IDBs is lower and exhibits a distribution with somewhat higher contrast over several atom columns than the ZnO domains.

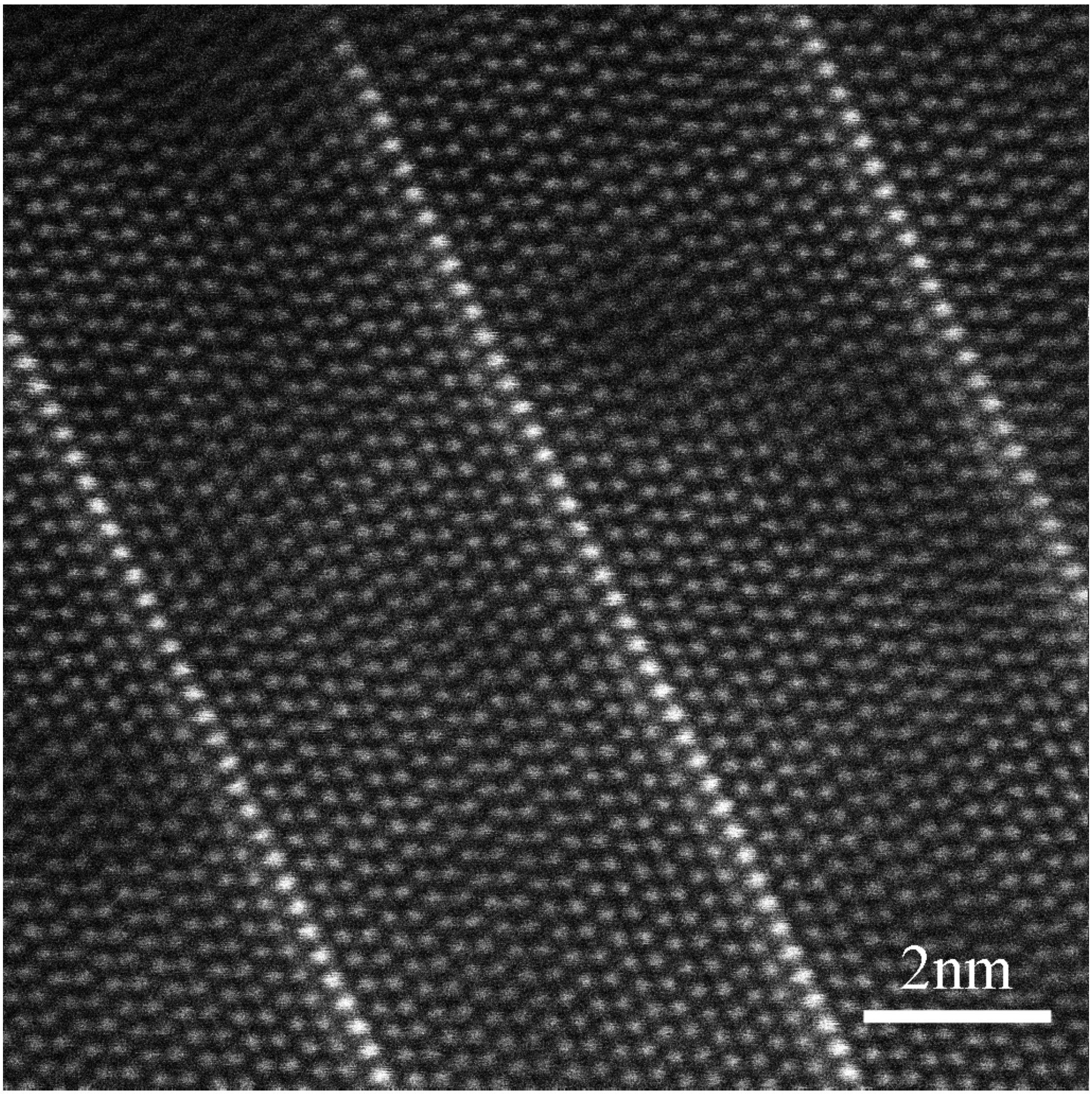

Fig.11-5. Atomically-resolved HAADF image of $In_2O_3(ZnO)_m$ (m = 15) compound in the *a* axis, showing slight contrast variations of the pyramidal IDBs.

Because both regions of the basal IDBs of the HR-TEM image (fig.7-4) and of the HAADF image (fig.11-6) are only ~ 10 nm from each other, from the determined specimen thickness at the basal IDB of about (3.4 ± 0.25) nm (fig.7-4), the specimen thickness (fig.11-6) can be estimated to be less than 10 nm, by considering the wedge-shaped specimen with a small wedge angle of ~10 °.

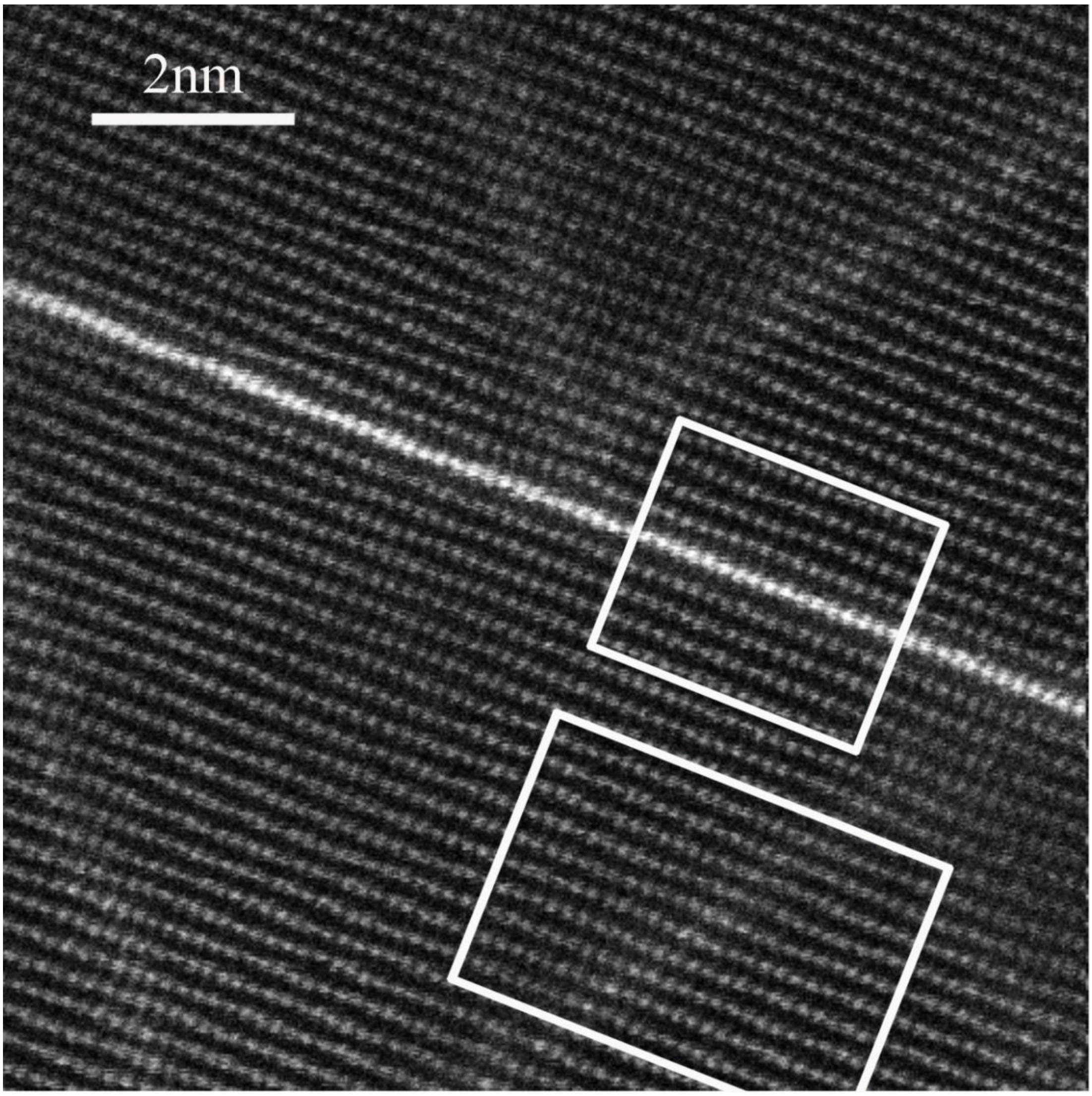

Fig.11-6. Atomically resolved HAADF image of $In_2O_3(ZnO)_{30}$ compounds in the *m* orientation with contrast of both IDBs.

11.1.1.3 Explanations of the reduced contrast of the pyramidal IDBs

Because ZnO has a hexagonal structure, the viewing directions $[1\bar{1}00]$, $[01\bar{1}0]$ and $[\bar{1}010]$ are equivalent and are considered as the *m* axes. The same is true for the *a* axes. One *m* axis and one of its neighbouring *a* axis form an angle of 30 ° by tilting around the c axis of ZnO. Due to the existence of the pyramidal IDBs, extending along only one of the three *m* axis, the viewing directions are no longer equivalent and the contrast of the pyramidal IDBs cannot be observed in other directions (fig.11-4).

The contrast of the pyramidal IDBs depends not only on the viewing direction [131] but also on the specimen ($In_2O_3(ZnO)_m$) thickness *t* (fig.7-3). For simplicity, the situation with only ONE In atom column of the pyramidal IDB is considered and no absorption is included:

In the $[1\bar{1}00]$ axis, the pyramidal IDBs are assumed to be edge-on and clear contrast can be observed, independent of the specimen thickness *t*.

In the viewing direction $[1\bar{2}10]$, the pyramidal IDBs are inclined and their contrast shows a spreading of width *d*, which depends on the specimen thickness *t*, with a relation given by: $d = t/2$. If the specimen thickness is relatively thick $\left(t \geq \sqrt{3} \cdot a \cdot m\right)$, with ‘a’ the lattice parameter of ZnO, both sides of the pyramidal IDBs might be overlapped, resulting in no visible contrast at the pyramidal IDBs. For *m* = 30, to observe the pyramidal IDBs, the maximum thickness t should be less than 16.62 nm.

In the viewing direction $[0\bar{1}10]$, the pyramidal IDBs is $60\,^{\circ}$from the edge-on condition. The width of the observed pyramidal IDB is even wider of $d = \sqrt{3}t/2$. The contrast of the pyramidal IDBs might be seen for thin specimens with thickness $t < \frac{2\sqrt{3}}{3} \cdot a \cdot m$. For m = 30, the maximum thickness t is ~ 11.08 nm.

In the viewing direction $[\bar{1}\bar{1}20]$, the pyramidal IDBs are lying perpendicular in the TEM specimen and the contrast of the pyramidal IDBs disappears completely.

If there is an In distribution at the pyramidal IDBs, it is only possible to observe the contrast of the pyramidal IDBs in a suitable *m* axis.

11.1.2 Information extraction

To obtain information of the contrast of the atom columns more quantitatively, the intensity line profiles are extracted from the HAADF images.

11.1.2.1 Line profiles across the basal IDBs

Fig.11-7a is a highly magnified image of the basal IDB in the *a* axis, selected from *region2* (see fig.11-4). The basal IDB is aligned horizontally. The intensity line profile is shown in fig.11-7b with an integration width of 7 atom columns. The minimum value of the HAADF image is assumed to be the contribution of the dark current, which is within a range of < 100 counts. Compared to the Zn signals of ~ 2000 counts, the contribution of the dark current can be neglected. The profiles of atom columns are assumed to be Gaussian-like. Using the self-module of the 'multi-peak Gaussian fit' by software Origin [153], the integrated intensities, corresponding to the atom columns, can be fitted and quantified by Gaussian functions. Thus, the ratio of the integrated intensity from the In signals and the averaged Zn signals, averaged over 10 Zn atom columns, can be obtained as: $\frac{I_{In}}{\overline{I}_{Zn}} = 2.4 \pm 0.1$.

Fig.11-8a is the HAADF image of the basal IDB in the *m* axis, selected in fig.11-6. The structure model of the basal IDB, which is obtained from the phase image analysis, fits the contrast of the related Zn and In atom columns in the HAADF image. An intensity line profile of the basal IDB along the prism plane is shown in fig.11-8b, with an integration width of 11 atom columns. The integrated intensities of the atom columns in the *m* axis can be quantified by using the same procedure for the line profile in the *a* axis. The resulting intensity ratio is $\frac{I_{In}}{\overline{I}_{Zn}} = 2.6 \pm 0.1$.

From the incoherence concept of the HAADF/STEM imaging, each atom can be considered as an individual scatterer with a cross-section about Z^n, deviating slightly from the Rutherford scattering, which predicts a Z^2 scattering dependence of the intensity, with the atomic number Z and a constant n depending on the collection condition ($1.6 < n < 2.0$) [154,155]. The Z dependency of HAADF image intensity can be proven from the intensity ratio from the experimental image in the *m* axis:

$\left(\frac{I_{In}}{I_{Zn}}\right)_{theo} \approx \frac{Z_{In}^n}{Z_{Zn}^n} = \left(\frac{49}{30}\right)^n = 2.6$, with $n = \sim 1.9$.

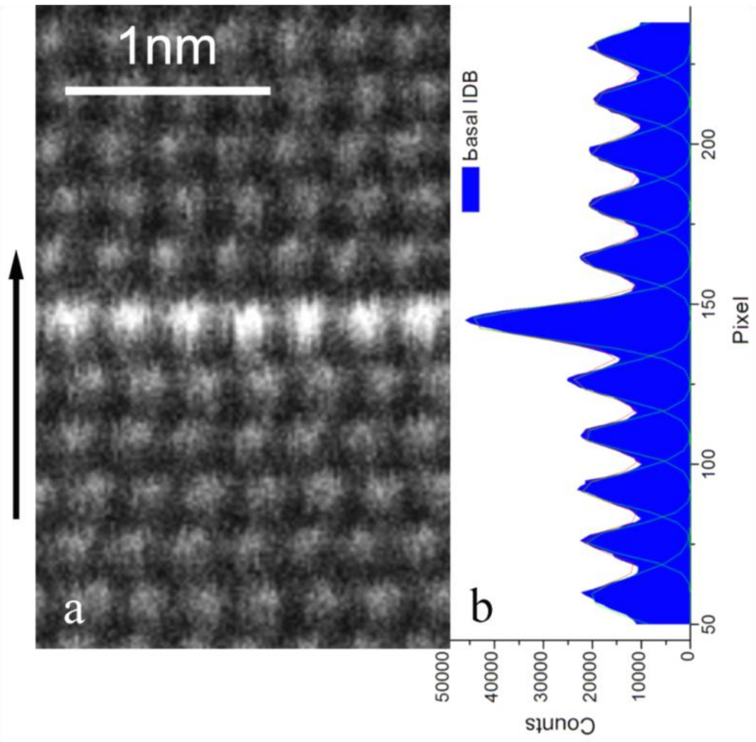

Fig.11-7. (a) Atomically resolved HAADF image at the basal IDB in the *a* axis, (b) corresponding intensity line profile, horizontally averaged.

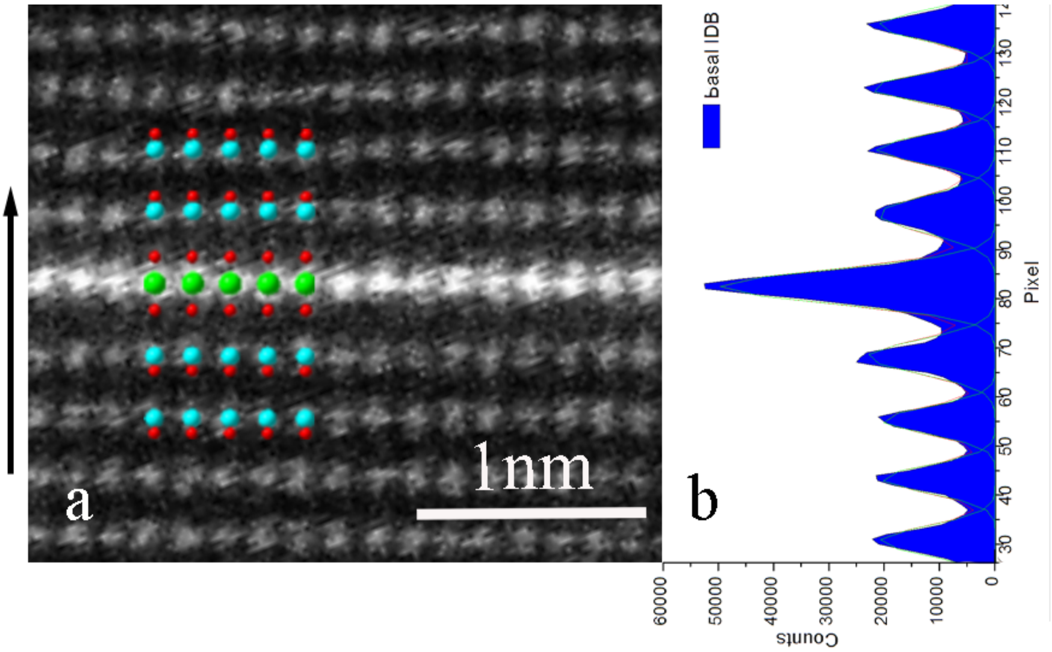

Fig.11-8. (a) Magnified HAADF image in the *m* axis, (b) corresponding intensity line profile integrated over 11 atom columns.

However, the intensity ratio of the basal IDB obtained in the *a* axis is smaller than that in the *m* axis. Possible reasons might be:

Orientation effect: due to different orientations, atom numbers in the column for these two zone axes are different. Therefore, the exit-plane wave function, hence the intensity collected by the HAADF detector, might be different.

Influence of the pyramidal IDBs: in the *m* axis, the region can be selected away from the pyramidal IDBs. However, in the *a* axis, contrast variations of the pyramidal IDBs are hardly seen. The selected region for the line profile might include the pyramidal IDBs, hence, the contribution of the In atoms, resulting in the increased signals of the Zn atom columns.

11.1.2.2 Line profiles across the pyramidal IDBs

The pyramidal IDBs are analyzed in the *m* axis. Because in the *a* axis, the pyramidal IDBs are inclined. The region at the pyramidal IDB (selected in fig.11-6) is shown in fig.11-9a. At the pyramidal IDBs, the In density per area and hence, the associated peak signal is lower compared to that at the basal IDB. An intensity line profile was chosen along the basal plane with an integration width of one atom column along *c* orientation of ZnO. In order to improve the signal to noise ratio, ten of such intensity line profiles along the basal planes were drawn, each with the same integration width. The intensity line profiles are shifted and aligned with respect to the position of the pyramidal IDB. The averaged intensity profile with 14 maxima is numbered and shown in fig.11-9b. It is apparent that the left four columns (col.1 - col.4) and the right five columns (col.10 - col.14) produce almost the same intensity and are lower in intensity than the five columns in the centre (col.5 - col.9). Thus, the nine atom columns, left and right, can be assumed to be pure Zn atom columns.

Because the column spacing is small of about 1.6 Å and the intensities between atom columns are relatively high, it is difficult to quantify the integrated intensities of the atom columns by the ‘multi-peak Gaussian fit’ module. An alternative way is to use simply the ‘column-sum’ method. The contribution of the atom column can be chosen within a range of two neighbouring intensity minima. The integrated intensity of the atom column is obtained by multiplying the pixel size with the sum of the intensities within the selected range. Thus, the integrated intensities and the average value of Zn columns can be calculated. The pyramidal IDB with higher contrast appears to be distributed over at least 3 atomic distances, which is in agreement with the analyzed result of phase-contrast imaging at atomic resolution. The intensity ratios of the integrated intensity of the five central columns and the average of Zn columns (col.1 - col.4 and col.10 - col.14) are shown in the 1st line of table 11-1.

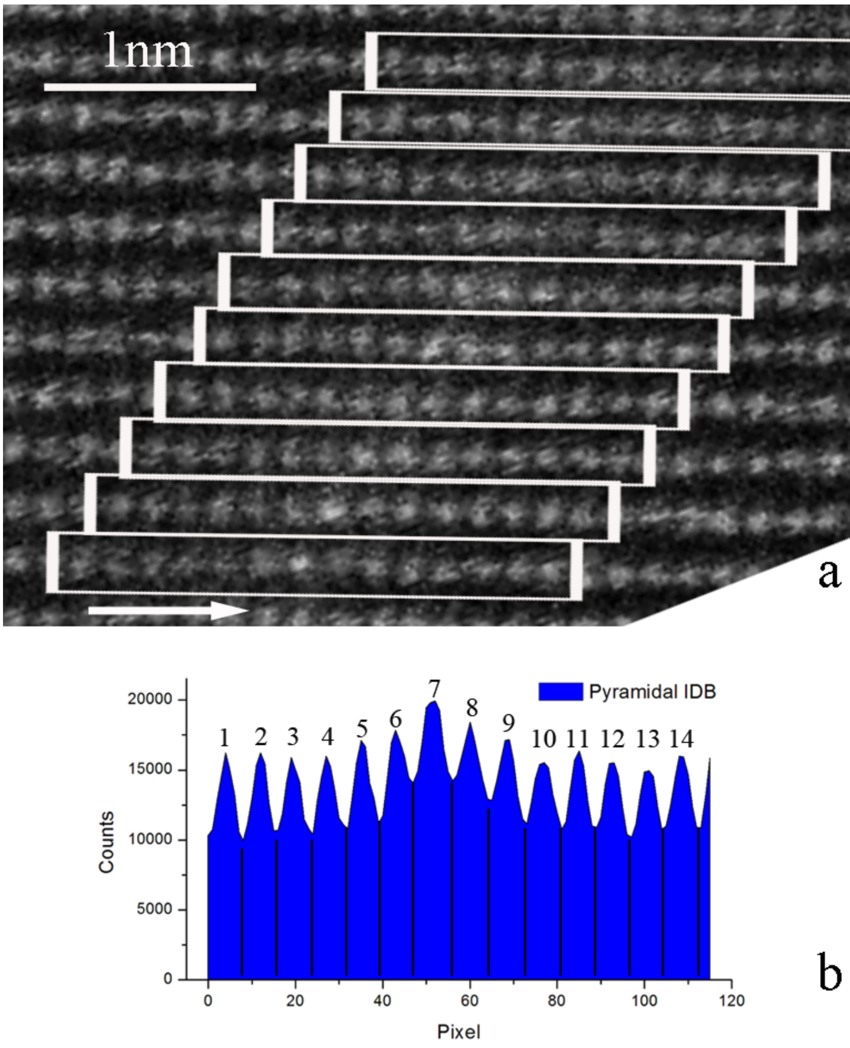

Fig.11-9. (a) HAADF image of the region containing the pyramidal IDB in the *m* axis, (b) corresponding averaged intensity line profile along 14 atom columns.

Column No.	5	6	7	8	9
Intensity ratio	1.15±0.11	1.25±0.12	1.46±0.14	1.30±0.13	1.20±0.12

Table 11-1. Intensity ratios of the integrated In(Zn) atom columns v.s. Zn columns from experimental HAADF image (fig.11-9).

11.2 HAADF image simulations of the pyramidal IDBs

This section is divided into five sub-sections. In sec.11.2.1, two structure models of the pyramidal IDB are generated. Based on the parameters of the microscope, HAADF images are simulated. In sec.11.2.2, thickness effects on intensities are first investigated. For different models of In content, a calibration curve presenting the relation between the intensity ratios of In(Zn) columns over Zn columns vs. In content of the atom column is obtained (sec.11.2.3). In the following subsection, effects of specimen tilt are discussed. Finally, an atomic structure model of the pyramidal IDB with an In distribution is proposed (sec.11.2.4).

11.2.1 HAADF image simulations by different atomic structure models

Because the contrast in the experimental HAADF images, the In appears to be distributed over at least 3 atom columns at the pyramidal IDBs. For simplicity, two structure models of the pyramidal IDBs (fig.10-6c) are generated for the simulations (code ref. [23]). The structure model 1 of the pyramidal IDB has an In distribution of 33.3% In content over 3 columns (fig.11-10). The structure model 2 of the pyramidal IDB has an In distribution of 25%, 50% and 25% In content over 3 columns (fig.11-12).

The parameters of the FEI Titan 80-300 probe-side aberration-corrected electron microscope were chosen, with accelerating voltage E = 300 keV, defocus Δf = 1.7 nm (at Scherzer defocus), spherical aberration coefficient C_s = -1 µm, chromatic aberration coefficient C_c = 1 mm, energy dispersion ΔE = 0.6 eV, convergence angle θ = 25 mrad and HAADF detector collecting angle D_{det} = 70-200 mrad. The pixel size of the simulated HAADF images is set to 0.2344 Å to avoid under-sampling, and the pixel size is ca. 4 times smaller than the probe size (< 1 Å) of the Titan microscope.

Based on the structure models of the pyramidal IDB (model 1 and model 2), two series of HAADF images with different sample thicknesses were simulated. From the structure model 1 of 33.3% In content over 3 columns, one series of the simulated HAADF images within a thickness range of 15.98 Å and 100.58 Å is displayed in fig.11-10. The bright contrast is mainly concentrated on the positions of the atom columns. However, with increase of thickness, e.g. to 100.58 Å, interference of atom columns can be observed with additional intensity between Zn columns. Intensity line

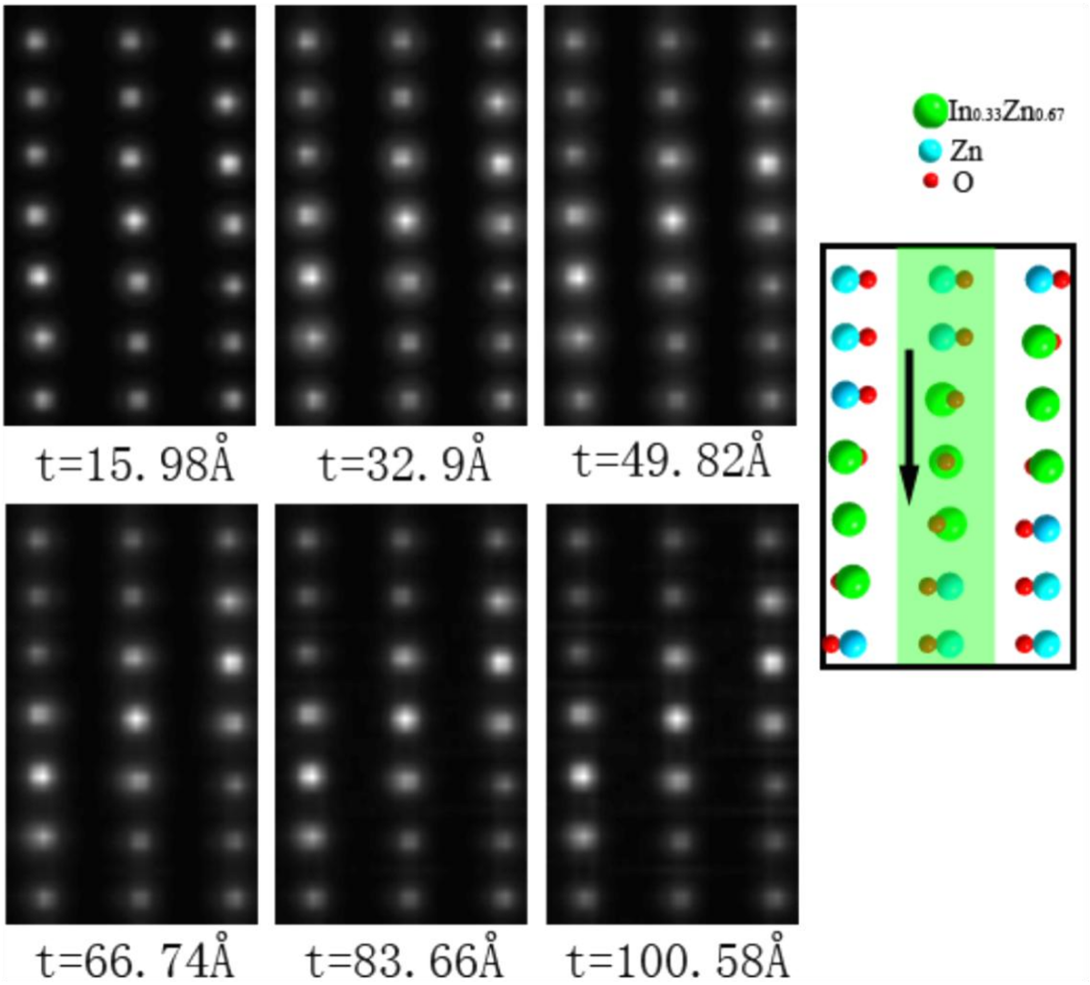

Fig.11-10. Thickness series of simulated HAADF images of the pyramidal IDB with a structure model containing 33.3% In over 3 atom columns each. Structure model of the pyramidal IDB on the right with columns of Zn (blue), O (red) and $2/3\,\mathrm{Zn} + 1/3\,\mathrm{In}$ (green).

profiles were extracted along the 2nd line of the image with an integration width of ~ 2.6 Å, as displayed by the green field in fig.11-10. The resulting line profiles are displayed in fig.11-11.

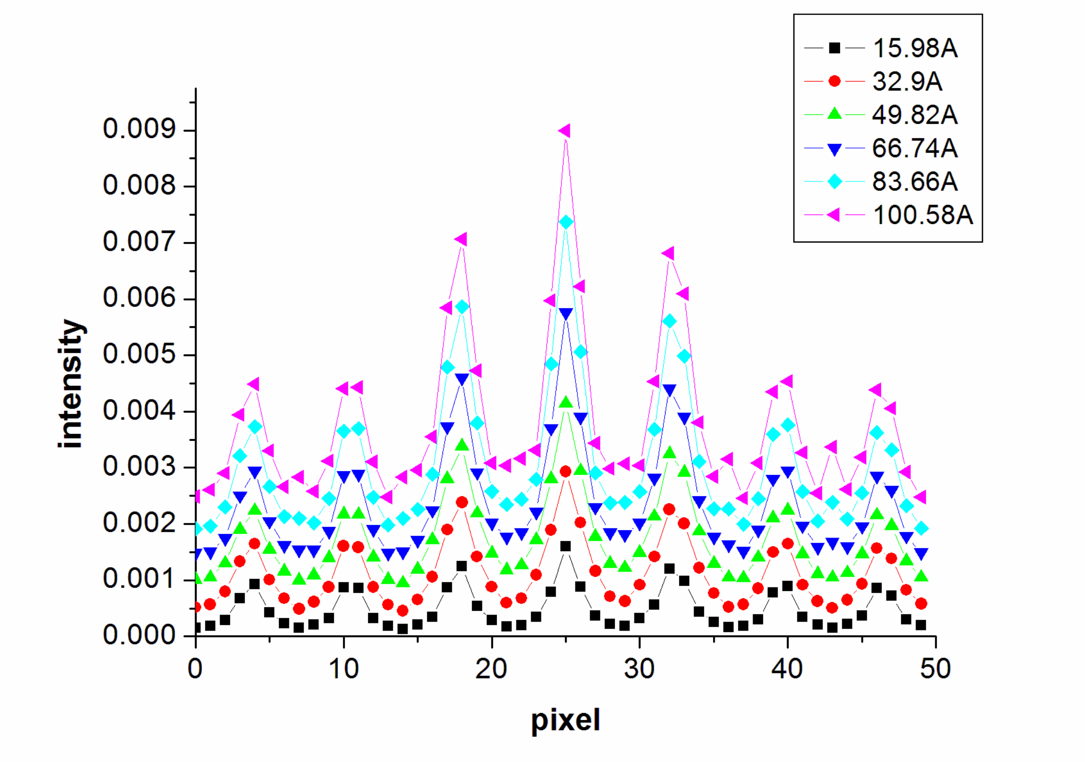

Fig.11-11. Intensity line profiles from the simulated HAADF images at different thickness with the normalized intensity. In distribution across pyramidal IDB is ~33% of In content over three atom columns, which exhibit higher intensity than the atom columns of pure Zn.

From the structure model 2 of 25%, 50% and 25% In content over 3 columns, the second series of simulated HAADF images within a thickness range of 21.63 Å and 81.30 Å is displayed in fig.11-12. Following the same procedure of the intensity extraction as for the structure model 1, the corresponding intensity line profiles are shown in fig.11-13.

From the two line profiles (fig.11-11 and fig.11-13), it is obvious that intensity from the atom columns increases with specimen thickness. The intensity from the central three In(Zn) atom columns is higher than that of the remaining Zn atom columns. However, the atom column in the centre exhibits the highest intensity maximum compared to its neighbouring In(Zn) atom columns. This might be due to the contribution of the weakly scattering O atoms, which align perfectly with the cations in this column, seen in the structure model of the pyramidal IDB. There are slight O atom displacements at the two neighbouring atom columns, Thus, due to the position change of O columns, it causes variations of the profiles in intensity maximum and profile widths (fig.11-11).

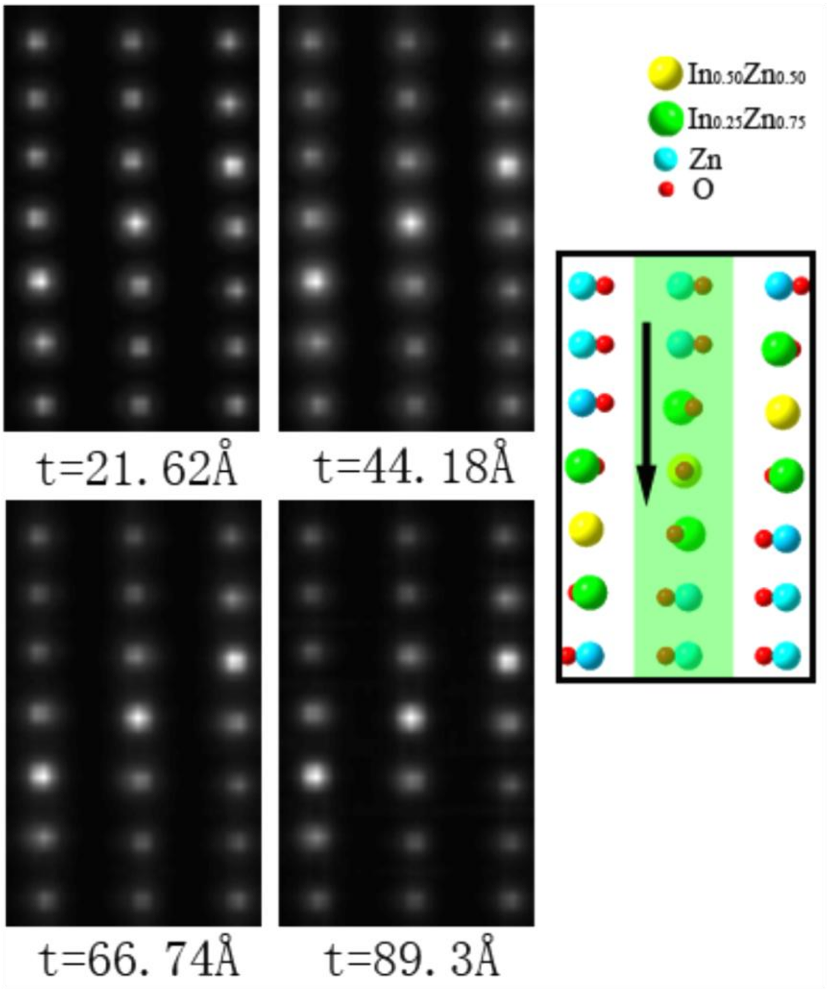

Fig.11-12. Thickness series of simulated HAADF images of the pyramidal IDB with a structure model of 25%, 50% and 25% In content distributed over 3 atom columns, respectively. Structure model of the pyramidal IDB on the right shows columns of Zn (blue), O (red), $\left(1/2\,\mathrm{Zn}+1/2\,\mathrm{In}\right)$ (yellow) and $\left(3/4\,\mathrm{Zn}+1/4\,\mathrm{In}\right)$ (green).

11.2.2 Investigation of specimen thickness effects on intensities

Due to the unknown absolute intensity of the incident electron beam, it is not wise to directly compare the intensities of the atom columns of different HAADF images. To overcome this dilemma, the integrated intensity ratios of the atom columns are used to compare different HAADF images. The integrated intensity of the atom column is calculated by the 'column sum' method (sec.11.1.2.2) and the corresponding integrated intensity ratios of the central three atom columns over the Zn columns are displayed in fig.11-14, which have almost the same ratios within the thickness range of 1 nm≤ t ≤10 nm.

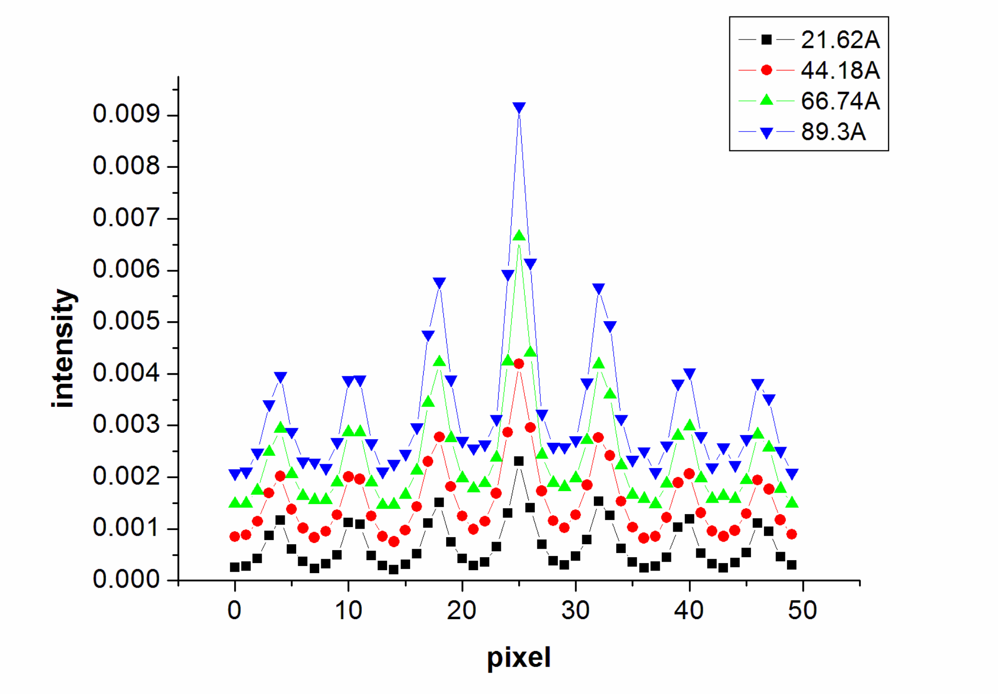

Fig.11-13. Intensity line profiles from the simulated HAADF images at different thickness with the normalized intensity. In distributions are 25%, 50% and 25% of In content over three atom columns, which exhibit higher intensity than the atom columns of Zn.

The calculated integrated intensity ratios for structure model 2 exhibit similar features, with the integrated intensity ratios having constant values over a thickness range of 2 nm ≤ t ≤ 9 nm (fig.11-15). Though small differences of the integrated intensity ratios for 25% In content at thin thickness are found, however, the difference is within the error of the method. Thus, a thickness dependency can be neglected for the considered thickness range of 1 nm ≤ t ≤ 10 nm and one can treat the intensity ratios as independent from specimen thickness.

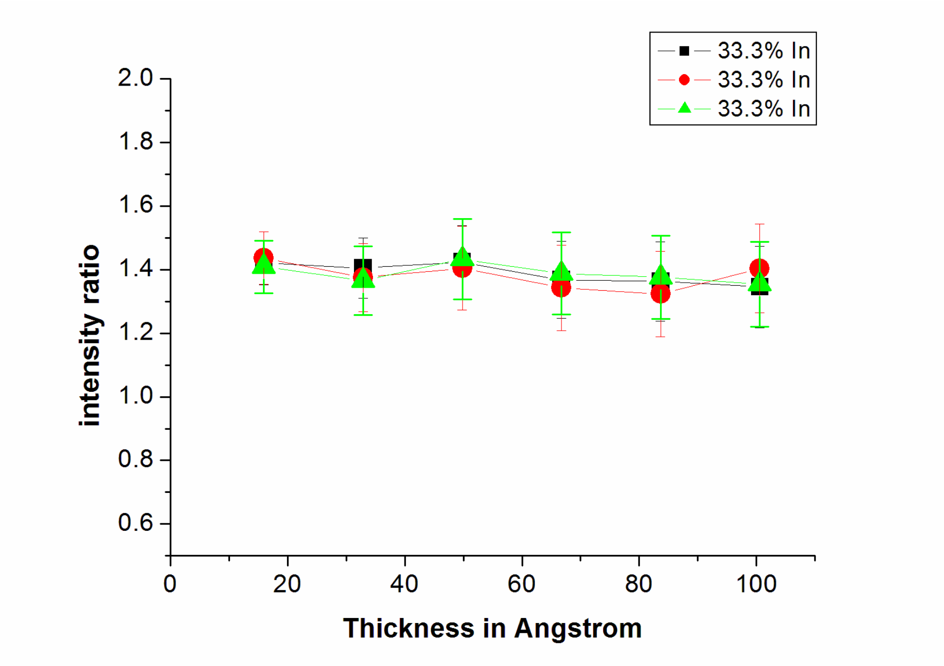

Fig.11-14. Intensity ratios of columns $\left(2/3\,\mathrm{Zn}+1/3\,\mathrm{In}\right)$ vs. Zn columns as function of specimen thickness from fig.11-10.

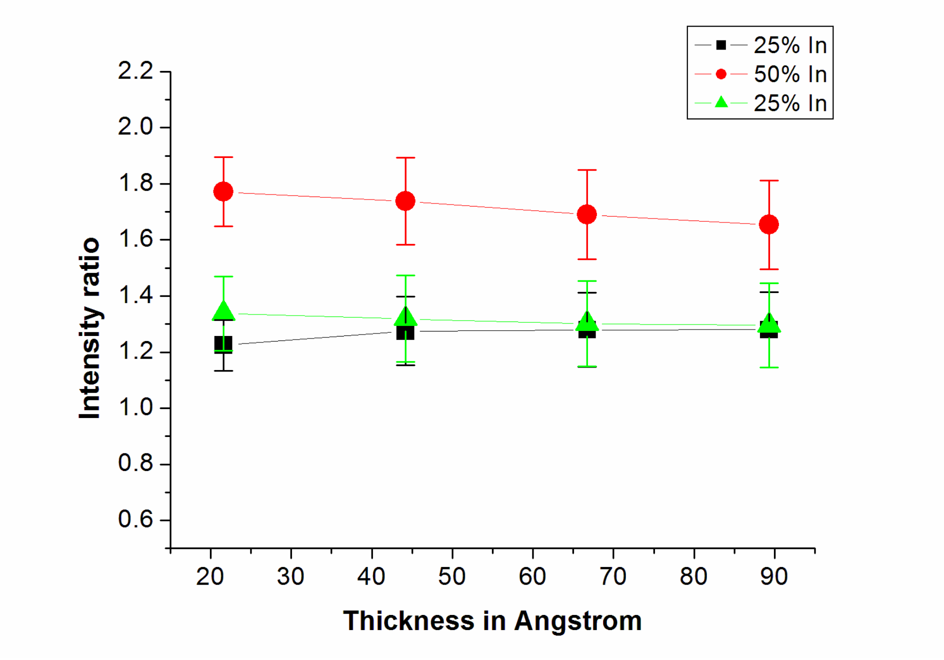

Fig.11-15. Intensity ratios of columns with different In content vs. Zn columns as function of specimen thickness from fig.11-12.

11.2.3 Investigation of the intensity ratios for different models of In content

Within a thickness range of 1 nm$\le t \le$10 nm, the integrated intensity ratios remain the same for a determined In content of the atom column. The mean intensity ratios for different In contents (25%, 33.3%, 50% and 100% of In) can be quantified as: 1.28 ± 0.05, 1.38 ± 0.03, 1.71 ± 0.08 and 2.66 ± 0.08, respectively. The intensity ratio for an In column (100% In) over a Zn column was obtained by the simulations of the basal IDB in the *m* axis as well as from the experimental image (sec.11.1).

A relation between the In content of an In(Zn) atom column and its integrated intensity ratio between that column over a Zn column can be obtained from the simulated HAADF images, shown as black symbols in fig.11-1b, which can be fitted as a formula: $y = y_0 + A \cdot e^{x/t}$, shown in red curve, with $y_0 = -0.37269 \pm 1.03769$, $A = 1.35338 \pm 0.97215$ and $t = 1.23324 \pm 0.58774$, respectively.

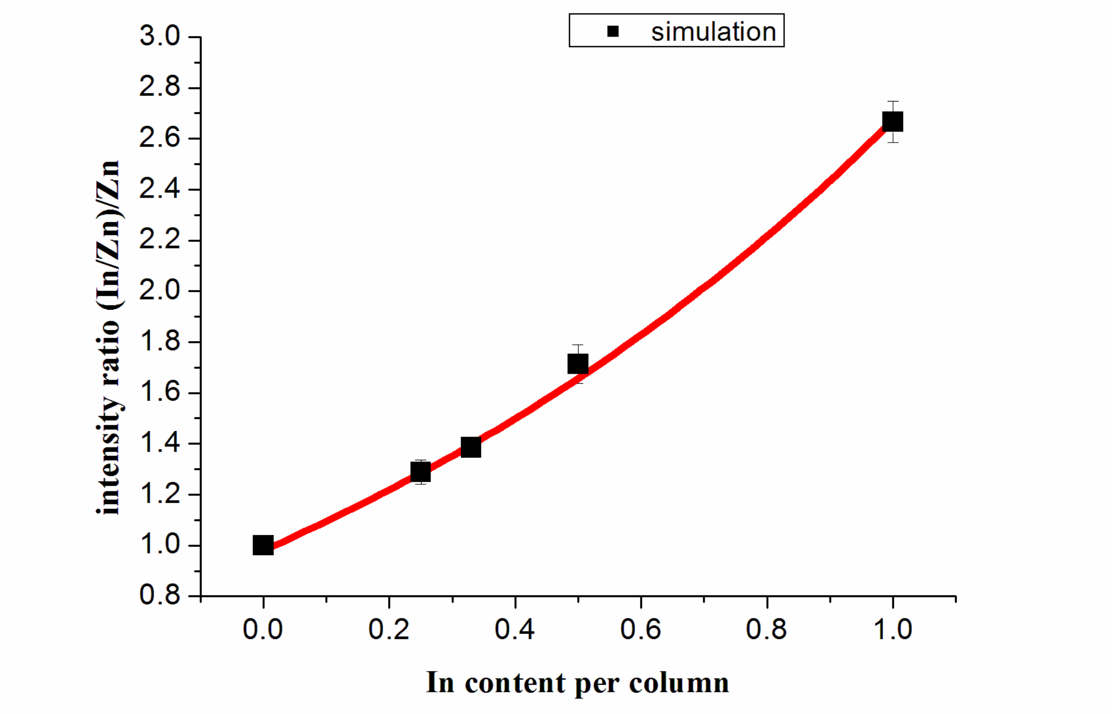

Fig.11-16. Intensity ratios as function of In content (red curve) determined from image simulations. Intensity ratios of columns in HAADF images at the pyramidal IDB can thus yield In contents.

Within the thickness range of 1 nm≤ t ≤10 nm, such relation can be treated as a calibration curve. With the determined integrated intensity ratios of the atom column at the pyramidal IDB over a Zn column, In contents of the atom column can be yielded.

11.2.4 Determination of In contents at the pyramidal IDB

As discussed in sec.11.2.1 - sec.11.2.3, it is possible to determine In contents at the pyramidal IDB from the experimental HAADF images by using the calibration curve (fig.11-16) from HAADF image simulations. Using experimental integrated intensity ratios, which are listed in the first line of table 11-1, the In content in atom percent of the atom column at the pyramidal IDBs can be quantified and displayed in fig.11-17.

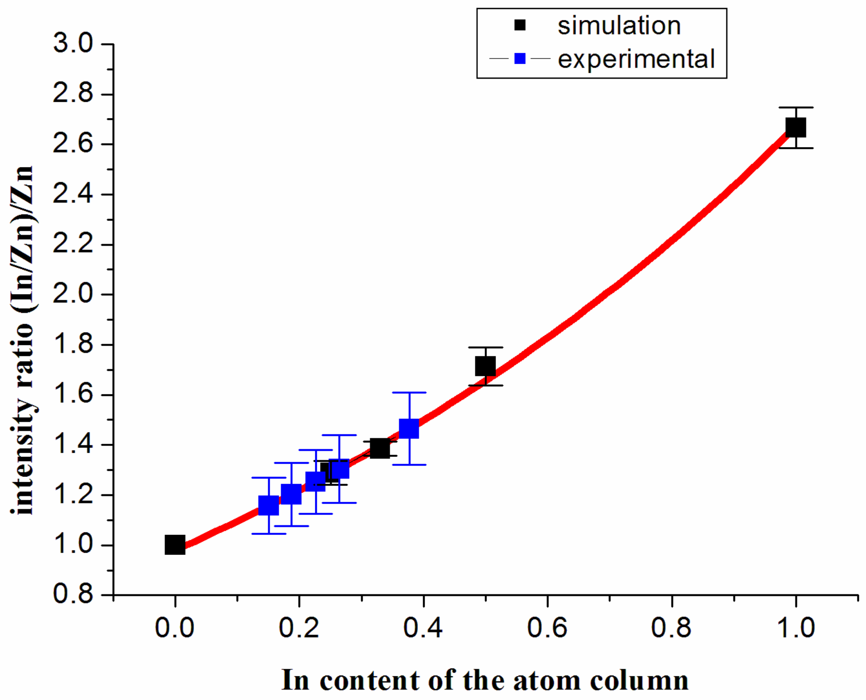

Fig.11-17. In contents at the pyramidal IDB, shown in blue, are calculated from the calibration curve of the integrated intensity ratios and In contents from the HAADF image simulations.

The quantified values are shown in table 11-2. Clearly, there is a distribution of In contents at the pyramidal IDB. The centre atom column (no. 7) has the highest In content of about 40%. Two neighbouring atom columns (no. 6 and no. 8) have In contents of ~20% and ~25%, respectively. The remaining In might be distributed in neighbouring atom columns of the pyramidal IDB, as shown in table 11-2.

Column No.	**5**	**6**	**7**	**8**	**9**
Intensity ratio	**1.15 ±0.11**	**1.25 ±0.12**	**1.46 ±0.14**	**1.30 ±0.13**	**1.20 ±0.12**
In contents (at%)	**12.6 ±9.6**	**20.6 ±10.2**	**36.4 ±10.1**	**24.6 ±10.5**	**16.5 ±10.4**

Table 11-2. Quantified In contents in at% of atom columns of the experimental HAADF image (fig.11-9), by using the calibration curve of a relation between the integrated intensity ratios and In contents from the simulations.

11.2.5 Effect of contrast variations by specimen tilt

In the experiments with a highly convergent electron beam, small residual tilt of the electron beam from the zone axis cannot be avoided. Therefore, the effect of the small specimen tilt to the HAADF contrast at the pyramidal IDBs needs to be examined. Specimen tilt $\vec{\tau}$ with the magnitude of 0.5° is under consideration and for simplicity, only four orientations of the specimen tilts are chosen:

1) $\tau_A = 0.5^\circ$, $\tau_B = 0$;
2) $\tau_A = 0$, $\tau_B = 0.5^\circ$;
3) $\tau_A = -0.5^\circ$, $\tau_B = 0$,
4) $\tau_A = 0$, $\tau_B = -0.5^\circ$.

The structure model for the pyramidal IDB of 33.3% In content distributed over 3 atom columns is generated for the simulations, which is displayed in the *m* axis (fig.11-18). The polar *c* orientations of ZnO domains are along *A* axis of the supercell. Due to time consumption, only parts of the supercell, in the dashed form (fig.11-18), are selected for the simulations, within the thickness range of 1 ~ 10 nm. Region *1* is selected for the specimen tilts of τ_A ($\pm 0.5^\circ$), containing 7×3 atom columns; region *2* is selected for the specimen tilts of τ_B.($\pm 0.5^\circ$) with 3×7 atom columns.

Fig.11-18a - d are the simulated HAADF images with specimen tilts for the chosen thicknesses. They exhibit similar features with a clear In distribution of higher

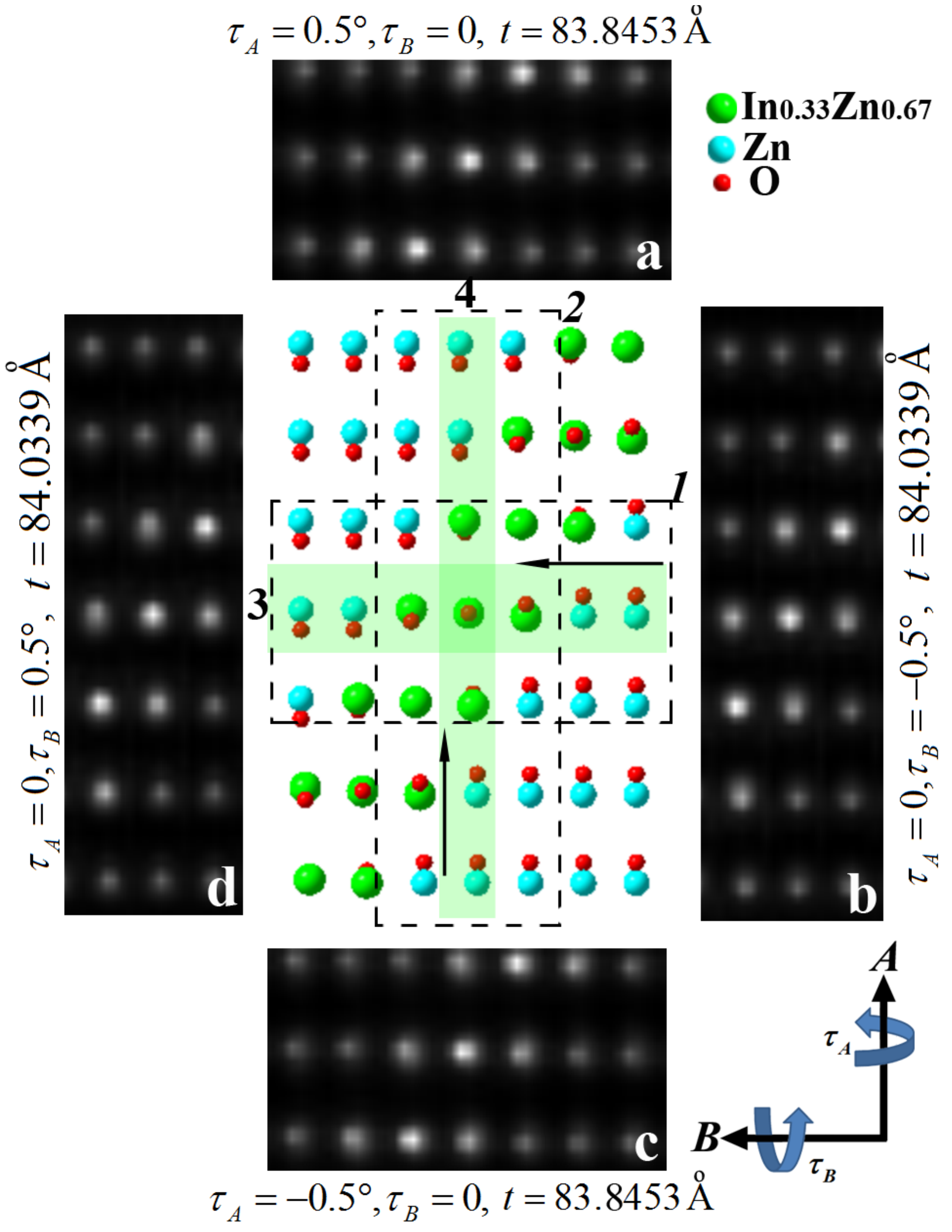

Fig.11-18. The structure model of the pyramidal IDB is shown in the centre. The simulated HAADF images with four orientations of specimen tilts are shown within the selected region *1* and *2*, respectively.

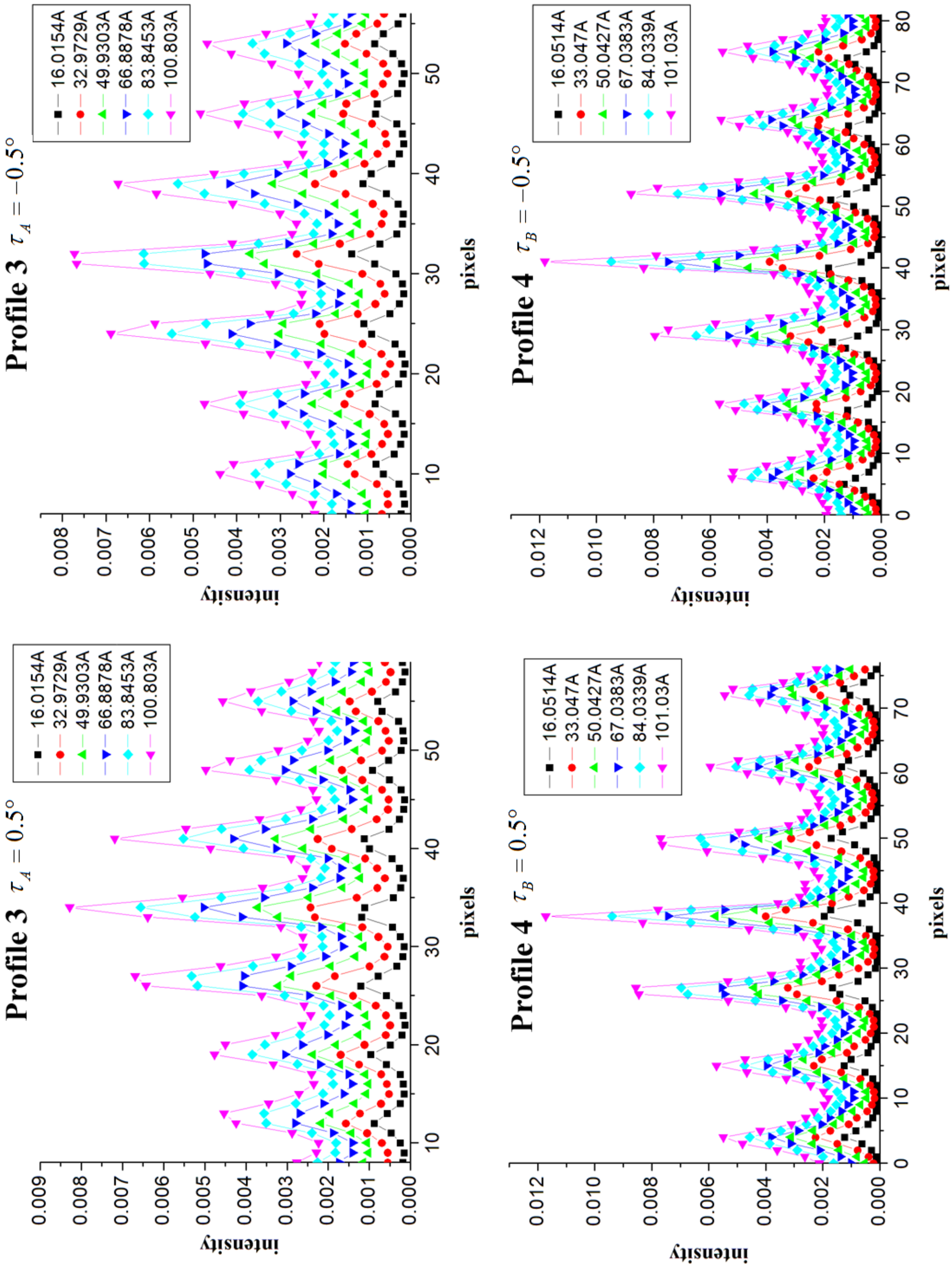

Fig.11-19. Intensity line profiles of simulated HAADF images with specimen tilt as function of specimen thickness. The line profiles show asymmetric features. With increase of thickness, the positions of the atom columns are shifting.

contrast than the rest Zn columns. Within the selected region *1* and *2*, line profiles of the central columns, along the black arrows, are integrated over one atom column (region 3 and 4 in green) to analyze the contrast differences in detail. The corresponding intensity line profiles with different specimen thicknesses are shown in fig.11-19. From the line profiles, one can directly observe that the column profiles are no longer ‘Gaussian-like’, they are asymmetric and exhibit elongated shapes, especially at relatively larger thicknesses. With an increase of the specimen thickness, the maxima positions of the atom columns are shifted.

The interesting points are the integrated intensity ratios. By using the ‘column sum’ method, the integrated intensity, hence the integrated intensity ratios of the three In(Zn) atom columns over that of a Zn column, can be calculated, which exhibit almost the same value. The mean integrated intensity ratios of In(Zn) over Zn columns with the specimen tilts τ_A (±0.5°) can be obtained. They are equivalent to 1.42 ±0.03. This also holds true for the specimen tilts τ_B (±0.5°) as 1.43 ±0.01. Compared with the integrated intensity ratio without specimen tilt of 1.38 ±0.02, there are no significant contrast variations of the simulated HAADF images with specimen tilt. Thus, it is reasonable to neglect the effect of the specimen tilts within a magnitude of 0.5 °and the calibration curve of the integrated intensity ratios and the In contents is still valid (fig.11-16).

11.2.6 Proposed structure model of the pyramidal IDB

Through HAADF image simulations, In contents at the pyramidal IDB of the experimental HAADF image were determined from the calibration curve (fig.11-17). A relaxed atomic structure model of the pyramidal IDB is then proposed with In ions in trigonal bi-pyramidal co-ordination and a distribution of In contents over 5 atom columns of about 10%, 20%, 40%, 20% and 10%, respectively. Based on this structure model, the HR-TEM image is simulated and displayed in fig.11-20.

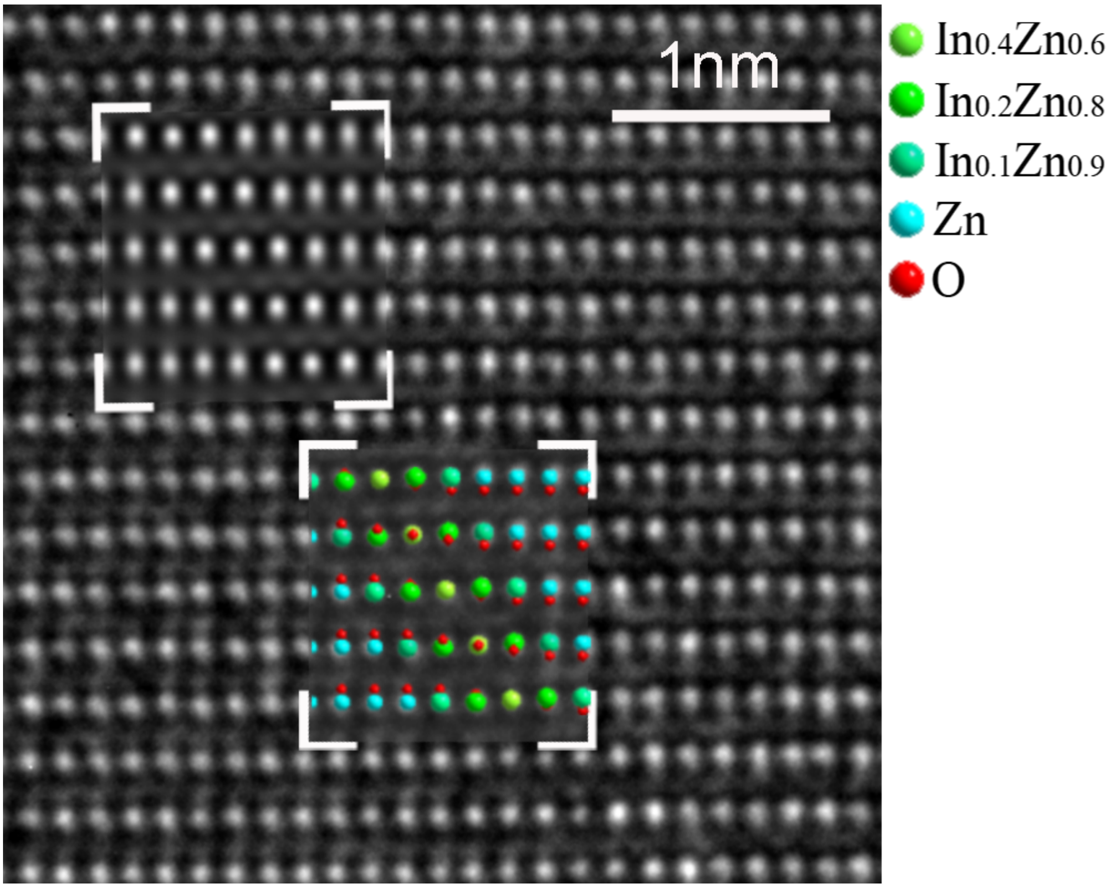

Fig.11-20. Atomically resolved HR-TEM image of the pyramidal IDB with a structure model with a distribution of In over 5 atom columns, with centre atom 40% of In and 20% of In at two neighbouring atom columns and 10% of In distributed at even further atom columns. The left-lower inset is the simulated phase-contrast TEM image.

11.3 Discussion of the domain microstructures

The results from atomic resolution phase-contrast and Z-contrast imaging of compounds with composition $In_2O_3(ZnO)_{30}$ depicted two main structural characteristics: In^{3+} ions form close-packed layers of edge sharing $\left[\mathrm{InO}_{6/3}^{-}\right]_2^{\infty}$ octahedrons and between them there is a wurtzite-type of structure $\left[(\mathrm{In},\mathrm{Zn})\mathrm{O}_{4/4}^{+}\right]_3^{\infty}$ consisting of $(\mathrm{InZn}_m)\mathrm{O}_{m+1}^{+}$ tetrahedrons. To prevent edge sharing with the $\left[\mathrm{InO}_{6/3}^{-}\right]_2^{\infty}$ octahedrons, the Zn^{2+} ions occupy the second type of tetrahedral sites (t_{II}), thereby forming ZnO domains with inverted *c* axis orientation [156]. Together with the octahedral layer and the original ZnO, they form the basal IDBs in a head-to-head configuration of the *c* axes. The ZnO block between two neighbouring basal IDBs must contain a second inversion domain boundary with ZnO domains in a tail-to-tail configuration of the *c* axes.

11.3.1 In^{3+} in trigonal bi-pyramids

Obviously, there is a strong tendency to preserve the hexagonal symmetry in the $\left(InZn_m\right)O^+_{m+1}$ wurtzite-type layers [157]. In the hexagonally close-packed oxygen layers, the tetrahedral sites are small and there is large stress to the surrounding crystal if the voids are fully occupied. To avoid this situation, the trivalent In^{3+} ions prefer 5-fold co-ordinations, which could be shown by x-ray diffraction with In^{3+} being built into the tail-to-tail oriented IDBs forming InO_5 trigonal bi-pyramids, for $m < 7$ [128,129].

From arguments of local charge balance, the ZnO_4 tetrahedrons $\left[ZnO^0_{4/4}\right]^\infty_3$ and the InO_6 octahedrons are neutral in charge. An In^{3+} ion tetrahedral co-ordinated by oxygen, $\left[InO^{+1}_{4/4}\right]^\infty_3$, has a local charge +1. However, if the In^{3+} ion is co-ordinated by a trigonal bi-pyramid, $\left[\left(InO_{3/3}O_{2/1}\right)^{+0.5}\right]^\infty_2$, the local charge is lowered to +0.5. Hence, according to Pauling’s rule, In^{3+} ions in 5-fold trigonal bi-pyramids are preferred. To preserve neutrality of local charge, the neighbouring Zn^{2+} ions in trigonal bi-pyramids, $\left[\left(ZnO_{3/3}O_{2/1}\right)^{-0.5}\right]^\infty_2$, have local charge of -0.5 and thus balance the positive charge produced by the In^{3+} ions in trigonal bi-pyramidal co-ordination.

11.3.2 Formation of zig-zag shaped pyramidal IDBs

The absolute energy of a surface or of an internal boundary scales with its area. From energetic considerations one would not expect the formation of zigzag-shaped boundaries in the $In_2O_3(ZnO)_m$ compounds with m > 7, if the boundary energy is independent of orientation and atomic structure. However, an increase of boundary area by a factor of ~ 1.8 compared to a planar boundary is measured. The TEM observations show that the domain boundaries on pyramidal planes must be energetically favoured, and the reason for that is the specific boundary energy γ_{pyr} of the pyramidal IDB being smaller than the energy of the planar IDB by more than a factor of 1.8. The obvious reason for lowering the specific boundary energy is distributing the In^{3+} ions over a larger space in the homologous compounds with large *m* offering sufficiently large wurtzite blocks. The somewhat larger ionic radius $r_{\mathrm{In3+/4}}$ = 0.62 Å compared to the Zn^{2+} ions with $r_{\mathrm{Zn2+/4}}$ = 0.60 Å [158] and in particular, the higher ionic charge can be assumed to be the driving force for distribution of In^{3+} ions. The charged $\left[\left(\mathrm{InO}_{3/3}\mathrm{O}_{2/1}\right)^{+0.5}\right]_2^{\infty}$ trigonal bi-pyramids will produce electrostatic repulsion, which is considered as the origin for the distribution of In^{3+} ions along the basal planes of ZnO, which is observed in HAADF images at atomic resolution. First, the distribution of In^{3+} ions over an area 1.8 times larger than the planar one reduces their mean distance at the pyramidal planes, and second, the distribution along the basal planes of ZnO by 10%, 20%, 40%, 20% and 10% over 5 atom columns, respectively, additionally reduces the mean distance at the pyramidal IDBs. By this operation, the observed strain is created with a lattice dilatation of max. $(4 \pm 0.8)\%$ and lattice rotation of $(1.9 \pm 0.3)°$.

Summary

In this work, the characteristic inversion domain microstructures of $In_2O_3(ZnO)_m$ (m = 30) compounds were investigated by TEM methods. Both phase contrast and Z-contrast imaging of the compounds were achieved at atomic resolution. The observed results and conclusions are given in the following.

Determination of displacements and the strain field

At bright-atom contrast condition, atomically resolved HR-TEM images of $In_2O_3(ZnO)_{30}$ were successfully acquired in $[1\bar{1}00]$ zone axis of ZnO, with projected metal columns of ~1.6 Å well resolved. For a sufficiently thin sample, bright contrast TEM images are directly interpretable as projected potentials of atom columns. From contrast maxima in the TEM images, local lattice distortions at the pyramidal IDBs were observed for the first time. Lattice displacements and the strain field in two-dimensions were visualized and measured using the 'DALI' algorithm.

The displacements are concentrated at the pyramidal IDBs over 3 - 4 atom columns. The displacements were quantified, given by $\vec{u} \approx \left(0.55 \pm 0.06\right)_{\vec{x}_1} + \left(0.16 \pm 0.06\right)_{\vec{x}_2}$ Å, with $\vec{x}_1$ aligned along the basal plane of ZnO. Influence to the position of contrast maxima by variations of specimen thickness, defocus and crystal tilt were discussed, and might induce an additional error of max. (0.126 ± 0.067) Å along $\vec{x}_1$.

The 2D strain was described as the symmetric term ε and the anti-symmetric term ω. The diagonal element ε_{11} of the strain field ε exhibits a lattice dilatation of max. $\left(4 \pm 0.8\right)\%$ at the pyramidal IDBs along $\vec{x}_1$. The off-diagonal elements of the rotation field ω, proves a rotation of the lattice by (1.9 ± 0.3) $^{\circ}$at a specific pyramidal IDB having the opposite signs at the pyramidal IDB with the other inclination. The strain field exhibits a plane of mirror symmetry through the centre of the triangular inversion domains IDBs.

Atomic structure of inversion domain boundaries by HR-TEM imaging

Atomically resolved single shot and focal series images of $In_2O_3(ZnO)_{30}$ were achieved in both zone axes of ZnO, $[1\bar{1}00]$ and $[2\bar{1}\bar{1}0]$, respectively.

- Basal IDB

From the lattice image contrast and assignment of atom columns, a close-packed In monolayer at the basal IDB is proven. At the bright-atom contrast condition, the weakly scattering O atom columns were resolved with a projected distance of ~ 1.1 Å to the In columns at the basal IDBs in $[1\bar{1}00]$ zone axis. The electron waves at the exit-plane were successfully reconstructed using the software package ‘TrueImage’. Compared with the simulated waves, specimen thickness t and tilt τ were estimated to be: $t = (3.4 \pm 0.25)$ nm and $\tau = (-0.5 \pm 0.1^\circ, -1.0 \pm 0.1^\circ)$, respectively. Finally, the atomic structure model of the basal IDB was refined iteratively. The basal IDB consists of a closed-packed edge-sharing layer of InO_6 octahedrons.

- Pyramidal IDB

The exit-plane wave of the pyramidal IDB in $[2\bar{1}\bar{1}0]$ zone axis was successfully reconstructed. In this zone axis, the pyramidal IDBs are inclined. Contrast from the weakly scattering O atom columns was clearly observed with a gradual positional transition across the pyramidal IDBs, directly proving the inversion of the polar c axis of the ZnO domains. From the observed results of images and the reconstructed exit-plane waves in both zone axes, a three-dimensional atomic structure model of the pyramidal IDB was then proposed with In in trigonal bi-pyramidal co-ordination. However, differences in contrast between the simulated and experimental phase images were observed, indicating a distribution of In at the pyramidal IDBs along the direction of the basal plane.

Determination of In contents at the pyramidal IDB

Z-contrast imaging was utilized to determine compositions of the chemical elements Zn and In at atomic resolution. Atomically resolved HAADF images of $In_2O_3(ZnO)_{30}$ were achieved in both zone axes. The weakly scattering O atoms did not produce significant contrast. From the Z-contrast of the metal columns, a close-packed In monolayer at the basal IDBs is clearly confirmed. Contrary to the basal IDB, the Z-contrast at the pyramidal IDBs indicated an In distribution over at least 3 atomic columns.

The intensity ratios of In(Zn) columns to the mean Zn columns were calculated, which could be used to quantify the In content in individual columns at the pyramidal IDB. Based on the structure models obtained from phase images, HAADF images of the pyramidal IDB in $[1\bar{1}00]$ zone axis were simulated with different In contents. From these results, effects of crystal thickness to the peak positions could be neglected for a thickness range of $1\ \mathrm{nm} \leq t \leq 10\ \mathrm{nm}$. Thus, a relation between the intensity ratios and In contents was obtained, which could be used as a calibration curve. After comparison with intensity ratios from experimental images, the mean In contents in atom percent of the atom columns could be quantified at the pyramidal IDBs. By simulations of HAADF images, peak positions are investigated showing that effects of crystal tilts up to $0.5°$ can be neglected. Finally, a three dimensional atomic structure model for the pyramidal IDB was proposed, with an In distribution of 10%, 20%, 40%, 20% and 10% of In contents over 5 atom columns along basal planes, respectively.

Through a detailed structural study of $In_2O_3(ZnO)_m$ compounds by using phase-contrast and Z-contrast imaging at atomic resolution, In^{3+} atoms are determined with trigonal bi-pyramidal co-ordination and are distributed at the pyramidal IDBs. Hence, the atomic structure of the pyramidal IDBs with precise atoms positions was made possible. The proposed 3D atomic structure of the pyramidal IDB could be treated as the base structure of the materials of type $RAO_3(MO)_m$ (with $m \geq 7$; R = Sc, Y, In Ho, Er, Tm, Yb, Lu; A = In, Ga, Al, Fe; and M = Mg, Mn, Fe, Co, Cu, Zn, Cd). In further studies, the structure of the pyramidal IDBs needs to be refined with calculations from first principles such as density functional theory. Though a plausible explanation for the formation of inversion domain structures was proposed for the Fe^{3+} doped ZnO, the mechanism of forming inversion domain microstructures needs to be investigated further for better understanding physical properties of this group of materials forming homologous structures.

References

1. M. Knoll and E. Ruska, Z.für Physik 78 (1932) 318.
2. H. Rose, Ultramicroscopy 56 (1994) 11.
3. D. B. Williams and C. B. Carter, Transmission electron Microscopy, Plenum Press, New York, 1996.
4. O. Scherzer, Optik 2 (1947) 114.
5. H. Rose, Optik 85 (1990) 19.
6. M. Haider, H. Rose, S. Uhlemann, E. Schwan, B. Kabius, K. Urban, Ultramicroscopy 75 (1998) 53.
7. O. L.Krivanek, N. Dellby, A. R. Lupini, Ultramicroscopy 78 (1999) 1.
8. G. Benner, M. Matijevic, A. Orchowski, P. Schlossmacher, A. Thesen, M. Haider, P. Hartel, Microsc Microanal. 10 (Suppl. 3) (2004) 6.
9. B. Freitag, S. Kujawa, P.M. Mul, J. Ringnalda, P.C. Tiemeijer, Ultramicroscopy 102 (2005) 209.
10. A.E. Thesen, M. Matijevic, G. Benner, Microsc Microanal. 11 (2005) 2144.
11. B. Freitag, S. Kujawa, P.M. Mul, P.C. Tiemeijer, Microsc Microanal. 10 (Suppl. 3) (2004) 4.
12. A. Steinecker, Ph.D. Dissertation, University of Bonn, 2000.
13. L. Reimer, Elektronenmikroskopische Untersuchungs- und Präparationsmethoden. 2.Auflage, Berlin, 1967.
14. L. Reimer, Transmission Electron Microscopy: Physics of Image Formation and Microanalysis, Springer-Verlag, Berlin, 1984.
15. B. Fultz and J. M. Howe, Transmission Electron Microscopy and Diffractometry of Materials, Springer-Verlag, Berlin Heidelberg and New York, 2001.
16. C. J. Humphreys. Rep. Prog. Phys. 42 (1979), 1825.
17. H. Bethe, Ann. Phys. 87 (1928) 55.
18. J. M. Cowley and A. F. Moodie, Acta Cryst. 10 (1957) 609.
19. P. Goodman and A. F. Moodie, Acta Cryst. A30 (1974) 280.
20. J. M. Cowley. Diffraction Physics, 2nd Ed. North-Holland, Amsterdam, 1975.
21. K. Ishizuka, Acta Cryst. A38 (1982) 773.
22. J. H. Chen, D. Van Dyck, and M. Op de Beck. Acta Cryst., A53 (1997) 576.
23. C. Koch, Ph.D. Dissertation, Arizona State University, 2002.
24. O. Scherzer, J. Appl. Phys.20 (1949) 20.

25. H. Lichte, Ultramicroscopy 38 (1991) 13.
26. W. Coene & A. J. E. M. Jansen, Scanning Microsc. Supl. 6 (1992) 379.
27. K. Heinemann, Optik 34 (1971) 113.
28. D. B. Williams and C. B. Carter, Transmission electron Microscopy, Plenum Press, New York, 1996, p.467.
29. M. Lentzen, B. Jahnen, C. L. Jia, A. Thust, K. Tillmann,& K. Urban, Ultramicroscopy 92 (2002) 233.
30. C. L. Jia, M. Lentzen, & K. Urban, Microsc. Microanal. 10 (2004) 174.
31. G. Moliere, Z. fur Naturforsch. 2A (1947) 133.
32. L. I. Schiff, Quantum Mechanics, McGraw-Hill, 1968.
33. K. Ishizuka, Ultramicroscopy, 5 (1980) 55.
34. M. Troyon. Optik 46 (1976) 439.
35. J. C. H. Spence, Experimental High-Resolution Electron Microscopy, 2nd Ed. Oxford University Press, New York, 1981.
36. M. Lentzen, Microsc. Microanal. 12 (2006) 191.
37. S. Kret, P. Ruterana, A. Rosenauer & d. Gerthsenet, Phys. Stat. Solidi (b) 227 (2001) 247.
38. M. J. Hÿtch, E. Snoeck, & R. Kilaas, Ultramicroscopy 74 (1998) 131.
39. URL http://www.hremresearch.com/
40. A. Rosenauer, S. Kaiser, T. Reisinger, J. Zweck, W. Gebhardt & D. Gerthsen, Optik 102 (1996) 63.
41. R. Bierwolf, H. Hohenstein, F. Philipp, O. Brandt, G. E. Crook, K. Ploog, Ultramicroscopy 49 (1993) 273.
42. P. Bayle, T. Deutsch, B. Gilles, F. Lancon, A. Marty, & J. Thibault, Ultramicroscopy 56 (1994) 94.
43. P. H. Jouneau, A. Tardot, B. Feuillet, H. Mariette, & J. Cibert, J. Appl. Phys. 75 (1994) 7310.
44. M. D. Robertson, J. E. Currie, J. M. Corbett, & J. B. Webb, Ultramicroscopy 58 (1995) 175.
45. A. Rosenauer, S. Kaiser, T. Reisinger, J. Zweck, W. Gebhardt, & D. Gerthsen, Optik, 102 (1996) 63.
46. D. Typke & K. Dierksen, Optik 99 (1995) 155.
47. J. Barthel, Ph.D. Thesis, FZ Jülich, 2007.
48. S. Uhlemann & M. Haider, Ultramicroscopy 72 (1998) 109.

49. O. L. Krivanek, N. Dellby, and A. R. Lupini, Ultramicroscopy 78 (1999) 1.
50. W. O. Saxton, J. Microscopy 179 (1995) 201.
51. F. Zemlin, K. Weiss, P. Schiske, W. Kunath, & K.H. Herrmann, Ultramicroscopy 3 (1978) 49.
52. URL http://www.ceos-gmbh.de/
53. A. Thust, M. H. F. Overwijk, W. M. J. Coene, & M. Lentzen, Ultramicroscopy 64 (1996) 249.
54. M. Op de Beeck, D. van Dyck, and W. M. J. Coene, Ultramiscorcopy 64 (1996) 167.
55. A. Thust, M. Lentzen, & K. Urban, Ultramicroscopy 53 (1994) 101.
56. A. Thust, W. M. J. Coene, M. Op de Beeck, & D. Van Dyck, Ultramicroscopy 64 (1996) 211.
57. W. M. J. Coene, A. Thust, M. Op de Beeck, & D. Van Dyck, Ultramicroscopy 64 (1996) 109.
58. R. F. Egerton, Electron Energy-Loss Spectroscopy in the Electron Microscope 2nd Ed. Plenum Press, New York and London, 1996.
59. G. Cliff, & G. W. Lorimer, J. Microsc. 103 (1975) 203.
60. L. Reimer, I. Fromm, P. Hirsch, U. Plate & R. Rennekamp, Ultramicroscopy 46 (1992) 335.
61. T. Walther, Ultramicroscopy 96 (2003) 401.
62. L. Reimer, Energy-Filtering Transmission Electron Microscopy, Springer-Verlag, Berlin, 1995.
63. A. V. Crewe, J. Wall, & J. Langmore, Visibility of single atoms, Science 168 (1970) 1338.
64. P. D. Nellist, & J. M. Rodenburg, Ultramicroscopy 54 (1994) 61.
65. P. D. Nellist, & S. J. Pennycook, Proceeding EMAG99 161 (1999) 315.
66. P. E. Batson, N. Dellby, & O. L. Krivanek, Nature 418 (2002) 617.
67. M. Haider, S. Hulmann, E. Schhwan, H. Rose, B. Kabius & K. Urban, Nature 392 (1998) 768.
68. M. Bosman, V. J. Keast, J. L. Garcia-Munoz, A. J. D’Alfonso, S. D. Findlay & L. J. Allen, Phys. Rev. Lett. 99 (2007) 086102.
69. K. Kimoto, et al., Nature 450 (2007) 702.
70. D. A. Muller, et al., Science 319 (2008) 1073.

71. S. J. Pennycook, D. E. Jesson, & M. F. Chisholm, Proceedings Microsc. Semicond. Mater. 100 (1989) 51.
72. S. J. Pennycook & D. E. Jesson, Ultramicroscopy 37 (1991) 14.
73. S. J. Pennycook & L. A. Boatner, Nature 336 (1988) 565.
74. J. C. H. Spence, High-Resolution Transmission Electron Microscopy, 3rd Ed., Oxford University Press, Oxford, 2003.
75. P. D. Nellist & S. J. Pennycook, Ultramicroscopy 78(1999)111.
76. D. E. Jesson & S. J. Pennycook, Proc. Roy. Soc. London A449 (1995) 273.
77. Z. L. Wang & J. M. Cowley, Ultramicroscopy 31 (1989) 437.
78. C. B. Boothroyd, R. E. Dunin-Borkowski & T. Walther, Mater. Res. Soc. Symp. Proc. 466 (1997) 113.
79. Z. L. Wang & J. M. Cowley, Ultramicroscopy 32 (1990) 275.
80. J. M. LeBeau, S. D. Findlay, L. J. Allen, & S. Stemmer, accepted for publications in Phys. Rev. Letters (2008).
81. T. Yamazaki, K. Watanabe, A. Recnik, M. Ceh, M. Kawasaki & M. Shiojiri, J. Electron Microsc. 49 (2000) 753.
82. K. Watanabe, N. Nakanishi, T. Yamazaki, M. Kawasaki, I. Hashimoto & M. Shiojiri, Phys. Stat. Sol. B 235 (2003) 179.
83. S. Sturm, A. Recnik, M. Kwasaki, T. Yamazaki, K. Watanabe, M. Shiojiri & M. Ceh, JEOL News 37 E (2002) 22.
84. A. Howie, J. Microsc. 117 (1979) 11.
85. A. V. Crewe, J. P. Langmore & M. S. Isaacson, Physical Aspects of Electron Microscopy and Microbeam Analysis, Wiley, New York, 1975.
86. C. J. Humphreys, A. Hart-Davis & J. P. Spencer, Proc. 8th Int. Congr. On Electron Microscopy, Canberra, 1974, p.248.
87. M. Kawasaki, T. Yamazaki, S. Sato, K. Watanabe & M. Shiojiri, Philos. Mag. A 81 (2001) 245.
88. R. F. Loane, P. Xu & J. Silcox, Ultramicroscopy 40 (1992) 121.
89. P. M. Voyles, D. A. Muller & E. J. Kirkland, Microsc. Microanal.10 (2004) 291.
90. D. D. Perovic, C. J. Rossouw & A. Howie, Ultramicroscopy 52 (1993) 353.
91. L. J. Allen, S. D. Findlay, M. P. Oxley & C. J. Rossouw, Ultramicroscopy 96 (2003) 47.
92. S. Hillyard & J. Silcox, Ultramicroscopy 52 (1993) 325.
93. S. Hillyard, R. F. Loane & J. Silcox, Ultramicroscopy 49 (1993)14.

94. S. Hillyard & J. Silcox, Ultramicroscopy 58 (1995) 6.
95. P. Hartel, H. Rose & C. Dinges, Ultramicroscopy 63 (1996) 93.
96. R. F. Loane, P. R. Xu & J. Silcox, Acta Crystallogr. A47 (1991) 267.
97. Y. P. Peng, P. D. Nellist & S. J. Pennycook, J. Electron Microsc. 53 (2004) 257.
98. M. M. J. Treacy & J. M. Gibson, Ultramicroscopy 52 (1993) 31.
99. C. Dwyer & J. Etheridge, Ultramicroscopy 96 (2003) 343.
100. G. Möbus & S. Nufer, Ultramicroscopy 96 (2003) 285.
101. T. Plamann & M.J.Hytch, Ultramicroscopy 78 (1999) 153.
102. C. J. Rossouw, L. J. Allen, S. D. Findlay & M. P. Oxley, Ultramcirscopy 96 (2003) 299.
103. Z. Yu, P. E. Batson & J. Silcox, Ultramicroscopy 96 (2003) 275.
104. D. O. Klenov, S. D. Findlay, L. J. Allen & S. Stemmer, Phys. Rev. B, 76 (2007) 014111.
105. S. E. Maccagnono-Zacher, K. A. Mkhoyan, E. J. Kirkland & J. Silcox, Ultramicroscopy 108 (2008) 718.
106. K. A. Mkhoyan, S. E. Maccagnano-Zacher, E. J. Kirkland, J. Silcox, Ultramicroscopy 108 (2008) 791.
107. V. Grillo, E. Carlino, & F. Glas, Phys. Rev. B, 77 (2008) 054103.
108. E. J. Kirkland, R. F. Loane & J. Silcox, Ultramicroscopy 23 (1987) 77.
109. A. Amali & P. Rez, Microsc. Microanal. 3 (1997) 28.
110. K. Ishisuka, Ultramicroscopy 90 (2002) 71.
111. E. J. Kirkland, Advanced Computing in Electron Microscopy, Plenum Press, New York, 1998.
112. K. Watanabe, T. Yamazaki, I. Hashimoto & M. Shiojiri, Phys. Rev. B 64 (2001) 115432.
113. T. Yamazaki, N. Nakanishi, A. Recnik, M. Kawasaki, K. Watanabe, M. Ceh & M. Shiojiri, Ultramicroscopy 98 (2004) 305.
114. S. J. Pennycook & D. E. Jesson, Phys. Rev. Lett. 64 (1990) 938.
115. C. R. Hall & P. B. Hirsh, Proc. Roy. Soc. A 286 (1965) 158.
116. G. Radi, Acta Crystallorg., Sect. A 26 (1970) 41.
117. D. M. Bird & O. A. King, Acta Crystallorg., Sect. A 46 (1990) 202.
118. S. D. Findlay, L. J. Alle, M. P. Oxley & C. J. Rossouw, Ultramicroscopy 96 (2003) 65.
119. URL http://www.fftw.org

120. URL http://www.mathworks.com/products/matlab/

121. Ü. Özgür, Ya. I. Alivov, C. Liu, et al., J. Appl. Phys. 98 (2005) 041301.

122. T. Minami, Semicond. Sci. Technol. 20 (2005) S35.

123. H. Kasper, Z. Anorg. Allg. Chem. 349 (1967) 113.

124. P. J. Cannard & R. J. D. Tilley, J. Solid State Chem.73 (1988) 418.

125. C. Li, Y. Bando, M. Nakamura, M. Onoda & N. Kimizuka, J. Solid State Chem. 139 (1998) 347.

126. C. Li, Y. Bando, M. Nakamura & N. Kimizuka, Micron 31 (2000) 543.

127. Y. Yan, S. J. Pennycook, J. Dai, R. P. H. Chang, A. Wang & T. J. Marks, Appl. Phys. Lett. 73 (1998) 2585.

128. C. Schinzer, F. Heyd & S. F. Matar, J. Mater. Chem. 9 (1999) 1569.

129. W. Pitschke & K. Koumoto, Powder Diffr. 14 (1999) 213.

130. L. Dupont, C. Maugy, N. Naghavi, C. Guery & J. -M. Tarascon, J. Solid State Chem. 158 (2001) 119.

131. T. Hörlin, G. Svensson & E. Olsson, J. Mater. Chem. 8 (1998) 2465.

132. C. Li, Y. Bando, M. Nakamura & N. Kimizuka, J. Electron. Microsc. 46 (1997) 119.

133. C. Li, Y. Bando, M. Nakamura & N. Kimizuka, Electron Microsc. Anal. 153 (1997) 475.

134. A. Loewe, Ph.D. Thesis, Uni. Bonn, 2001.

135. C. Li, Y. Bando, M. Nakamura & N. Kimizuka, Z. Kristallogr. 214 (1999) 528.

136. N. Kimizuka, M. Isobe & M. Nakamura, J. Solid State Chem. 116 (1995) 170.

137. H. Hiramatsu, W. -S. Seo & K. Koumoto, Chem.Mater.10 (1998) 3033.

138. T. Moriga, D. D. Edwards, T. O. Mason, G. B. Palmer, K. R. Poeppelmeier, J. L. Schindler & C. R. Kannewurf, J. Am. Ceram. Soc. 81 (1998) 1310.

139. N. Ohashi, I. Sakaguchi, S. Hishita, Y. Adachi, H. Hareda & T. Ogino, J. Appl. Phys. 92 (2002) 2378.

140. Y. Yan, J. L. F. Da Silva, S.-H. Wei & M. Al-Jassim, Appl. Phys. Lett. 90 (2007) 261904.

141. N. Kimizuka, M. Isobe, M. Nakamura & T. Mohri, J. Solid State Chem. 103 (1993) 394.

142. M. Nakamura, N. Kimizuka, T. Mohri & M. Isobe, J. Solid State Chem. 105 (1993) 535.

143. C. W. Na, S. Y. Bae & J. Park, J. Phys. Chem. B 109 (2005) 12785.

144. D.-G. Kim, S. Lee, D.-H. Kim, G.-H. Lee & M. Isshiki, Thin Solid Films 516 (2008) 2045.
145. J. Jie, G. Wang, X. Han & J. G. Hou, J. Phys. Chem. B 108 (2004) 17027.
146. L. Xu, Y. Su, Y. Che, H. Xiao, L. Zhu, Q. Zhou & S. Li, J. Phys. Chem. B 110 (2006) 6637.
147. H. Fan, B. Fuhrmann, R. Scholz, C. Himcinschi, A. Bergre, H. Leipner, A. Dadgar, A. Krost, S. Christiansen, U. Gösele & M. Zacharias, Nanotechnology 17 (2006) S231.
148. M. Lentzen, B. Jahnen, C. L. Jia, A. Thust, K. Tillmann & K. Urban, Ultramicroscopy 92 (2002) 223.
149. L. Houben, A. Thust & K. Urban, Ultramocriscopy 106 (2006) 200.
150. M. Op de Beeck, D. van Dyck & W. M. J. Coene, Ultramicroscopy 64 (1996) 167.
151. P. A. Stadelmann, Ultramicroscopy 21 (1987) 131.
152. W. H. Press, W. T. Vetterling, S. A. Teukolsky, B. P. Flannery: Numerical Recipes in C. pp. 547-549. Cambridge University Press, 1992.
153. URL http://www.originlab.com
154. R. F. Klie & Y. Zhu, Micron 36 (2005) 219.
155. P. D. Nellist & S. J. Pennycook, Ultramicroscopy 78 (1999) 111.
156. O. Köster-Scherger, H. Schmid, N. Vanderschaeghe, F. Wolf, and W. Mader, J. Am. Ceram. Soc., 90 (2007) 3984.
157. O. Madelung, M. Schultz, and H. Weiss, edl, Semiconductor: Physics of group IV elements and III-V compounds, vol. 17 of Landolt-Börstein, New Series, Group III, Springer-Verlag, Berlin, 1982.
158. R. D. Shannon, Acta Cryst. A32 (1976) 751.

Appendix A

Scherzer defocus

The contrast of TEM images is dominated by the *PCTF*.

When $\chi = -\frac{n}{2}$ $n \in N_0$, $\sin(2\pi\chi) = 0$. To maximize the phase contrast of a weak-phase object, the ideal case is to set $\sin(2\pi\chi)$ to be nearly -1 and as flat as possible. So, $\frac{\partial \chi(\vec{g})}{\partial g} = Z\lambda g + Cs\lambda^3 g^3 = 0 \Rightarrow g = \sqrt{\frac{-Z}{Cs\lambda^2}}$.

From the case $\sin(2\pi\chi) \approx -0.86$, with $2\pi\chi$ between -120 ° and -60 °, the passband of *PCTF* comes to the minimum with $-\frac{2\pi}{3} = 2\pi\left(\frac{1}{2}Z\lambda g^2 + \frac{1}{4}Cs\lambda^3 g^4\right)$. So, in the case of defocus (referred as Scherzer's defocus) $Z_{Sch} = -\left(\frac{4}{3}Cs\lambda\right)^{1/2}$, the phase contrast of a weak-phase object is maximized up to the maximum spatial frequency: $g_{Sch} = \left(\frac{3}{16}Cs\lambda^3\right)^{-1/4}$.

Appendix B

Lichte defocus

The contrast delocalization is quantified by the radius of *PSF*:,

$$R = \max\left|\frac{\partial \chi}{\partial \vec{g}}\right| = \max\left|Z\lambda g + Cs\lambda^3 g^3\right|,\ g \in [0, g_{\max}],$$

Set $f(g) = Z\lambda g + Cs\lambda^3 g^3$,

If $g_0 = 0, \sqrt{\frac{-Z}{Cs\lambda^2}}$, $f(g) = 0$, with $Z_0 = -Cs\lambda^2 g_0^2$.

$f'(g) = Z\lambda + 3Cs\lambda^3 g^2 = 0 \Rightarrow g_{in} = \sqrt{\frac{-Z}{3Cs\lambda^2}}$ with g > 0 and $f''(g) = 6Cs\lambda^3 g > 0$.

$$f\left(g\right)_{\min} = Z\lambda g_{in} + Cs\lambda^3 g_{in}^3 = -2Cs\lambda^3\left(\frac{-Z}{3Cs\lambda^2}\right)^{\frac{3}{2}} < 0 \text{ with } Z = -3Cs\lambda^2 g_{in}^2 .$$

At the meantime, $f\left(g_{\max}\right) = Z\lambda g_{\max} + Cs\lambda^3 g_{\max}^3$.

The problem left is to find the minimum value of the delocalization for $g \in \left[0, g_{\max}\right]$.

Set function $G(Z) = -f\left(Z\right)_{\min} - \left|f\left(g_{\max}\right)\right|$,

Then, $G(Z) = \begin{cases} -f\left(Z\right)_{\min} + f\left(g_{\max}\right) > 0 \\ -f\left(Z\right)_{\min} - f\left(g_{\max}\right) \end{cases}$, with $\begin{matrix} Z < -Cs\lambda^2 g_{\max}^2 \\ Z \geq -Cs\lambda^2 g_{\max}^2 \end{matrix}$

For the case $Z \geq -Cs\lambda^2 g_{\max}^2$:

$$\begin{aligned} G(Z) &= -f\left(Z\right)_{\min} - f\left(g_{\max}\right) = -Z\lambda\left(\frac{-Z}{3Cs\lambda^2}\right)^{1/2} - Cs\lambda^3\left(\frac{-Z}{3Cs\lambda^2}\right)^{3/2} - Z\lambda g_{\max} - Cs\lambda^3 g_{\max}^3 \\ &= -Cs\lambda^3\left(g_{\max}^3 - 3\left(\frac{-Z}{3Cs\lambda^2}\right)g_{\max} - 2\left(\frac{-Z}{3Cs\lambda^2}\right)^{3/2}\right) \\ &= -Cs\lambda^3\left(g_{\max} - \left(\frac{-4Z}{3Cs\lambda^2}\right)^{1/2}\right)\left(g_{\max}^2 + 2\left(\frac{-Z}{3Cs\lambda^2}\right)^{1/2} g_{\max} + \left(\frac{-Z}{3Cs\lambda^2}\right)\right) \end{aligned}$$

For $Z < 0$, the third term of above equation is larger than 0;

$$G(Z) = \begin{cases} \geq 0 \\ < 0 \end{cases} \text{ with } \begin{matrix} -0.75Cs\lambda^2 g_{\max}^2 \geq Z \geq -Cs\lambda^2 g_{\max}^2 \\ Z > -0.75Cs\lambda^2 g_{\max}^2 \end{matrix} .$$

For the case $Z < -Cs\lambda^2 g_{\max}^2$:

$$R(Z) = \begin{cases} -f\left(g_{\max}\right) \\ -f\left(Z\right)_{\min} \end{cases} \text{ with } \begin{matrix} Z \leq -3Cs\lambda^2 g_{\max}^2 \\ -3Cs\lambda^2 g_{\max}^2 < Z < -Cs\lambda^2 g_{\max}^2 \end{matrix} .$$

$$\text{Thus, } R(Z) = \begin{cases} -f\left(g_{\max}\right) = -Z\lambda g_{\max} - Cs\lambda^3 g_{\max}^3 & Z \leq -3Cs\lambda^2 g_{\max}^2 \\ -f\left(Z\right)_{\min} = 2Cs\lambda^3\left(\frac{-Z}{3Cs\lambda^2}\right)^{3/2} & \text{, with } -3Cs\lambda^2 g_{\max}^2 < Z \leq -\frac{3}{4}Cs\lambda^2 g_{\max}^2 \\ f\left(g_{\max}\right) = Z\lambda g_{\max} + Cs\lambda^3 g_{\max}^3 & Z > -0.75Cs\lambda^2 g_{\max}^2 \end{cases} .$$

Set the defocus to be $Z_{Lichte} = -\frac{3}{4} Cs\lambda^2 g_{\max}^2$, the minimum contrast delocalization is given by: $R_{Lichte,\min} = 2Cs\lambda^3 \left(\frac{-Z_{Lichte}}{3Cs\lambda^2} \right)^{3/2} = \frac{1}{4} Cs\lambda^3 g_{\max}^3$.

Appendix C

Transmission coefficient

The aberration function $\chi(k;Z)$ can be expanded in terms of *k* and *Z* around k', k'' and Z, thus:

$$\chi(k+k'';Z+Z') - \chi(k+k';Z+Z') = \left[\chi(k'';Z') - \chi(k';Z')\right] + \\ k(\chi''_k - \chi'_k) + Z(\chi''_Z - \chi'_Z) + kZ(\chi''_{kZ} - \chi'_{kZ})$$

with $\chi_k = \frac{\partial \chi(k,Z)}{\partial k} = Cs\lambda^3 k^3 - Z\lambda k$, $\chi_Z = \frac{\partial \chi(k,Z)}{\partial Z} = -\frac{\lambda}{2} k^2$ and $\chi_{kZ} = \frac{\partial^2 \chi(k,Z)}{\partial Z \partial k} = -\lambda k$.

When the source spread function and the chromatic defocus spread function are represented by the normalized two- and one-dimensional Gaussians:

$s(k) = \frac{1}{\pi q_0^2} \exp\left(-\frac{k^2}{q_0^2} \right)$ and $f(Z) = \frac{1}{\sqrt{\pi}\Delta} \exp\left(-\frac{Z^2}{\Delta^2} \right)$, respectively,

with q_0 and Δ the 1/e half-width values, respectively.

The transmission cross-coefficient can then be carried out:

$$T(k'+k,k';Z) = \frac{a(k'')a(k')\exp\left\{-2\pi i\left[\chi(k'',Z) - \chi(k',Z)\right]\right\}}{\pi q_0^2 \sqrt{\pi}\Delta} \int dZ \cdot \\ \exp\left(-\frac{Z^2}{\Delta^2} - 2\pi i Z(\chi''_Z - \chi'_Z) \right) \int dk \exp\left\{ -\frac{k^2}{q_0^2} - 2\pi i\left[(\chi''_k - \chi'_k) + Z(\chi''_{kZ} - \chi'_{kZ}) \right] k \right\}$$

$$= \frac{a(k'')a(k')\exp\left\{-2\pi i\left[\chi(k'',Z) - \chi(k',Z)\right]\right\}}{\sqrt{\pi}\Delta} \int dZ \cdot \exp\left(-\frac{Z^2}{\Delta^2} - 2\pi i Z(\chi''_Z - \chi'_Z) \right) \cdot \\ \exp\left\{ -\pi^2 q_0^2 \left[(\chi''_k - \chi'_k) + Z(\chi''_{kZ} - \chi'_{kZ}) \right]^2 \right\}$$

$$= \frac{a(k'')a(k')\exp\left\{-2\pi i\left[\chi(k'',Z)-\chi(k',Z)\right]\right\}}{\sqrt{\pi}\Delta}\int dZ\cdot\exp\left\{-\frac{1+\pi^2q_0^2\Delta^2\left(\chi''_{kZ}-\chi'_{kZ}\right)^2}{\Delta^2}\left[Z^2+\right.\right.$$

$$\left.\left.2\cdot\frac{\pi i\Delta^2\left(\chi''_Z-\chi'_Z\right)+\pi^2q_0^2\Delta^2\left(\chi''_k-\chi'_k,\chi''_{kZ}-\chi'_{kZ}\right)}{1+\pi^2q_0^2\Delta^2\left(\chi''_{kZ}-\chi'_{kZ}\right)^2}\cdot Z\right]-\pi^2q_0^2\left(\chi''_k-\chi'_k\right)^2\right\}$$

$$= \frac{a(k'')a(k')\exp\left\{-2\pi i\left[\chi(k'',Z)-\chi(k',Z)\right]\right\}}{\sqrt{1+\pi^2q_0^2\Delta^2\left(\chi''_{kZ}-\chi'_{kZ}\right)^2}}\exp\left[-\pi^2q_0^2\left(\chi''_k-\chi'_k\right)^2\right]\cdot$$

$$\exp\left\{\frac{\left[\pi i\Delta\left(\chi''_Z-\chi'_Z\right)+\pi^2q_0^2\Delta\left(\chi''_k-\chi'_k,\chi''_{kZ}-\chi'_{kZ}\right)\right]^2}{1+\pi^2q_0^2\Delta^2\left(\chi''_{kZ}-\chi'_{kZ}\right)^2}\right\}$$

$$= \frac{a(k'')a(k')\exp\left\{-2\pi i\left[\chi(k'',Z)-\chi(k',Z)\right]\right\}}{\sqrt{1+\pi^2q_0^2\Delta^2\left(\chi''_{kZ}-\chi'_{kZ}\right)^2}}\exp\left[\frac{2\pi i\left(\pi q_0\Delta\right)^2\left(\chi''_Z-\chi'_Z\right)\cdot\left(\chi''_k-\chi'_k,\chi''_{kZ}-\chi'_{kZ}\right)}{1+\pi^2q_0^2\Delta^2\left(\chi''_{kZ}-\chi'_{kZ}\right)^2}\right]\cdot$$

$$\exp\left[-\frac{\pi^2q_0^2\left(\chi''_k-\chi'_k\right)^2}{1+\pi^2q_0^2\Delta^2\left(\chi''_{kZ}-\chi'_{kZ}\right)^2}\right]\cdot\exp\left\{-\frac{\left[\pi\Delta\left(\chi''_Z-\chi'_Z\right)\right]^2}{1+\pi^2q_0^2\Delta^2\left(\chi''_{kZ}-\chi'_{kZ}\right)^2}\right\}\cdot$$

$$\exp\left\{-\frac{\pi^4q_0^4\Delta^2\left(\chi''_k-\chi'_k\right)^2\left(\chi''_{kZ}-\chi'_{kZ}\right)^2-\left[\pi^2q_0^2\Delta\left(\chi''_k-\chi'_k,\chi''_{kZ}-\chi'_{kZ}\right)\right]^2}{1+\pi^2q_0^2\Delta^2\left(\chi''_{kZ}-\chi'_{kZ}\right)^2}\right\}$$

$$= a(k'')a(k')\exp\left\{-2\pi i\left[\chi(k'',Z)-\chi(k',Z)\right]\right\}\cdot\underbrace{\exp\left[\frac{2\pi i\left(\pi q_0\Delta\right)^2\left(\chi''_Z-\chi'_Z\right)\cdot\left(\chi''_k-\chi'_k,\chi''_{kZ}-\chi'_{kZ}\right)}{1+\pi^2q_0^2\Delta^2\left(\chi''_{kZ}-\chi'_{kZ}\right)^2}\right]}_{P(k'',k',Z)}\cdot$$

$$\underbrace{\exp\left[-\frac{\pi^2q_0^2\left(\chi''_k-\chi'_k\right)^2}{1+\pi^2q_0^2\Delta^2\left(\chi''_{kZ}-\chi'_{kZ}\right)^2}\right]}_{E_s(k'',k',Z)}\cdot\underbrace{\exp\left\{-\frac{\left[\pi\Delta\left(\chi''_Z-\chi'_Z\right)\right]^2}{1+\pi^2q_0^2\Delta^2\left(\chi''_{kZ}-\chi'_{kZ}\right)^2}\right\}}_{E_f(k'',k')}\cdot$$

$$\underbrace{\exp\left\{-\frac{\pi^4q_0^4\Delta^2\left[\left(\chi''_k-\chi'_k\right)\times\left(\chi''_{kZ}-\chi'_{kZ}\right)\right]^2}{1+\pi^2q_0^2\Delta^2\left(\chi''_{kZ}-\chi'_{kZ}\right)^2}\right\}/\sqrt{1+\pi^2q_0^2\Delta^2\left(\chi''_{kZ}-\chi'_{kZ}\right)^2}}_{E_x(k'',k')}$$

Formula $\sqrt{\frac{\pi}{a}}=\int e^{-ax^2}dx$ and $a^2b^2-(a,b)^2=(a\times b)^2$ are used for the detailed deduction above. The integrating factors k and Z are of two- and one-dimension, respectively.

Appendix D

Intensity line profile with different integration widths

For each block of the following images, 2D Gaussian shape with different sampling rate are generated and shown in the left-up corner. Line profiles are assumed along x-direction of the image (fig.6-2). Single line profiles with different y values are also calculated in blue, the displayed in the right-up of the block. To see more details, the diagrams with the averaged profiles in black and the middle maximum single 1D Gaussian profile in red are shown in the left-down of the block. Finally, the ratio between the average line profile and the single line profile with maximum intensity is calculated (right-down of the block).

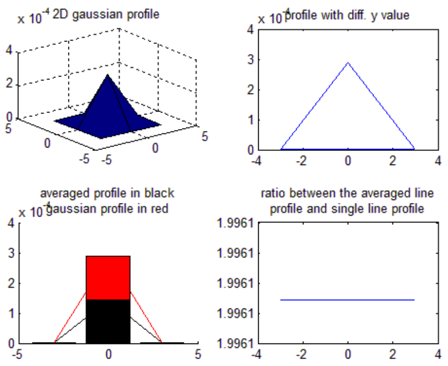

Sampling rate=3

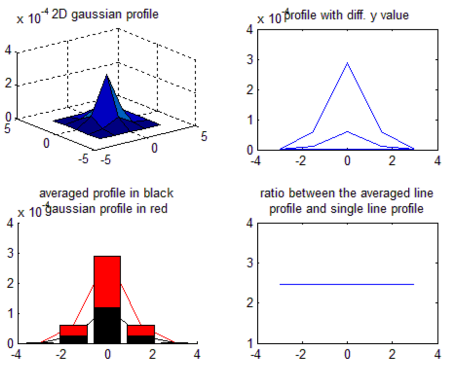

sampling rate=5

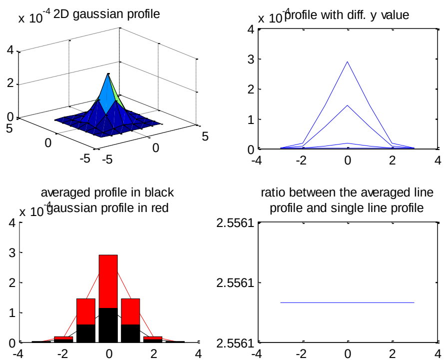

Sampling rate=7

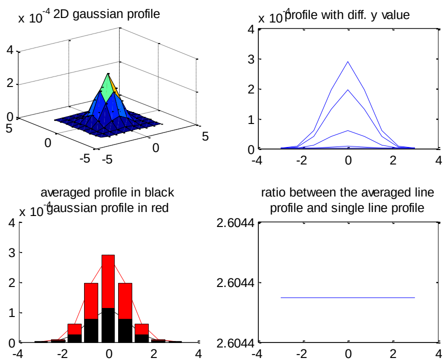

sampling rate=9

(to be continued)

(to be continued)

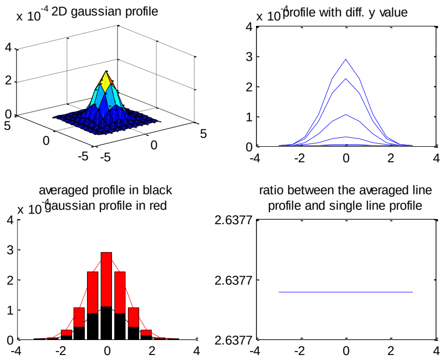

Sampling rate=11

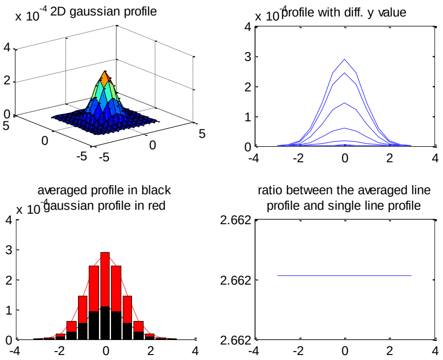

sampling rate=13

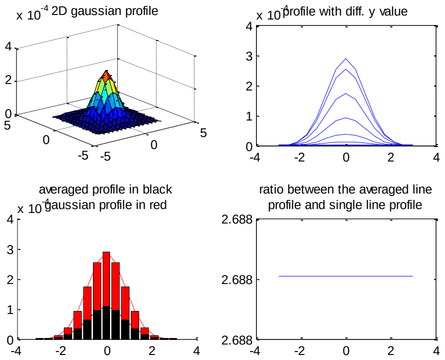

Sampling rate =15

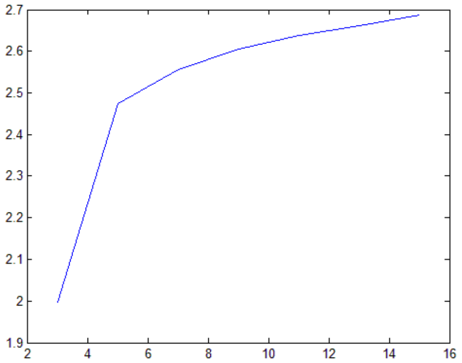

deviation of the averaged/single profile

Obviously, if the contribution from a single atom column is with or within ONE pixel of CCD, the ratio is always equal to 1. If the signal from a single atom column is more than one pixel on the CCD, the ratios are different with the increase of the sampling rate.

Appendix E

Atomic structure refinement at the basal IDB

In order to improve efficiency, the phase-plate approximation (parabolic algorithm) was used for image simulations. In the *m* axis, the slice thickness was first estimated to be 0.940 Å (according to the x-ray diffraction data for ZnO and $In_2O_3(ZnO)_m$ with m = 3,5). The structure model containing the basal IDB was refined by four steps: the projected distances of In-In atom columns along basal plane and In-O, In-Zn and Zn-

Zn atom columns along prism plane. Both simulated and experimental images as well as simulated and reconstructed exit-plane waves are used for comparison. The parameters with the highest (or nearly the highest) XCCs are chosen with bold in red, shown in the following tables. The atom structure model can then be refined.

After the determination of structure in the *m* axis, the reconstructed phase in the *a* axis (fig.10-2) was used for checking the validity of the slice thickness.

0. Check the slice thickness effect

Sample parameters: slices 36 (3.2 nm), x_tilt = -0.5 °, y_tilt = -1 °, *Cs* = -0.0127 mm, focal spread = 4.00 nm, convergence angle = 0.20 mrad, pixel size = 0.01024 nm/pixel, supercell size = 140×64, image rotation = -15.50 °

Image	Defocus (nm)	PosX (px)	PosY (px)	XCC (0.880Å)	XCC (0.895Å)	XCC (0.910Å)	XCC (0.925Å)	**XCC (0.940Å)**	XCC (0.955Å)	XCC (0.970Å)
1	18.4	358	187	0.901	0.901	0.901	0.901	**0.901**	0.901	0.901
2	17.5	360	195	0.920	0.920	0.920	0.920	**0.920**	0.920	0.920
3	16.6	355	221	0.915	0.915	0.916	0.916	**0.916**	0.916	0.916
4	15.7	351	218	0.914	0.914	0.914	0.915	**0.915**	0.915	0.916
5	14.9	345	216	0.903	0.903	0.903	0.904	**0.904**	0.904	0.904
6	14.0	344	214	0.910	0.910	0.910	0.909	**0.909**	0.909	0.909
7	13.1	341	209	0.883	0.884	0.884	0.885	**0.886**	0.886	0.886
8	12.2	342	210	0.855	0.857	0.859	0.861	**0.863**	0.864	0.866
9	11.3	344	208	0.830	0.832	0.834	0.835	**0.835**	0.837	0.838
10	10.4	347	225	0.812	0.815	0.817	0.819	**0.821**	0.822	0.824
11	9.50	347	226	0.841	0.843	0.844	0.846	**0.847**	0.849	0.850
12	8.60	345	226	0.860	0.861	0.861	0.862	**0.862**	0.862	0.862
13	7.70	340	225	0.829	0.830	0.832	0.833	**0.833**	0.834	0.835
14	6.80	337	221	0.852	0.853	0.853	0.855	**0.856**	0.857	0.857
15	5.90	334	223	0.892	0.893	0.894	0.894	**0.894**	0.895	0.894
16	5.00	334	222	0.885	0.885	0.884	0.884	**0.883**	0.882	0.881
17	4.10	336	232	0.868	0.868	0.869	0.869	**0.870**	0.870	0.871
18	3.20	333	230	0.843	0.843	0.844	0.844	**0.844**	0.844	0.844
19	2.30	335	230	0.844	0.845	0.846	0.847	**0.848**	0.849	0.849
20	1.40	335	231	0.788	0.791	0.793	0.794	**0.794**	0.795	0.795
21	0.50	333	233	0.426	0.444	0.468	0.485	**0.502**	0.519	0.533
22	-0.60	334	229	0.621	0.622	0.627	0.627	**0.628**	0.628	0.628
23	-3.30	330	223	0.576	0.574	0.573	0.572	**0.570**	0.569	0.567
24	-4.30	333	214	0.631	0.630	0.628	0.627	**0.626**	0.624	0.624
25	-5.30	335	211	0.798	0.796	0.794	0.793	**0.789**	0.788	0.787
26	-6.40	329	213	0.840	0.838	0.837	0.835	**0.834**	0.832	0.830
27	-7.30	329	208	0.902	0.901	0.900	0.898	**0.896**	0.894	0.892
28	-8.20	324	205	0.924	0.923	0.922	0.920	**0.919**	0.917	0.915
29	-9.10	322	200	0.946	0.946	0.945	0.944	**0.944**	0.943	0.942
30	-10.00	316	195	0.952	0.952	0.952	0.952	**0.951**	0.951	0.951
sum				24.961	24.989	25.024	25.047	**25.060**	25.076	25.087

For the above image simulations with different slice thicknesses, the differences of the XCCs are very small. Combined with the pure ZnO x-ray data, the slice thickness of 0.940 Å is preferred.

1. Check twice the projected distance between In-In along basal planes

Image 15th: thickness 3.4 nm

Name	Rota.	posX	posY	slices	tilt		XCC32x32	XCC32x128
test_In_In_3.11A.txt	-15.60	333	238	36	-0.5	-1.0	0.958	0.831
test_In_In_3.15A.txt	-15.60	333	238	36	-0.5	-1.0	0.962	0.854
test_In_In_3.19A.txt	**-15.60**	**333**	**238**	**36**	**-0.5**	**-1.0**	**0.963**	**0.850**
test_In_In_3.23A.txt	-15.60	333	222	36	-0.5	-1.0	0.963	0.835
test_In_In_3.27A.txt	-15.60	333	221	36	-0.5	-1.0	0.961	0.794
test_In_In_3.31A.txt	-15.60	333	221	36	-0.5	-1.0	0.958	0.736
test_In_In_3.35A.txt	-15.60	333	221	36	-0.5	-1.0	0.953	0.664
test_In_In_3.39A.txt	-15.60	333	22)	36	-0.5	-1.0	0.946	0.585

Wave: Absorption 0.050, Zero beam Attenuation 0.120, free propagation -0.10 nm

Name	Rota.	posX	posY	slices	tilt		XCCa 32x32	XCCp 32x32	XCCa 32x128	XCCp 32x128
test_In_In_3.11A.txt	-15.50	47.0	-58.0	36	-0.8	-1.0	0.623	0.937	0.609	0.897
test_In_In_3.15A.txt	-15.50	47.0	-57.0	36	-0.8	-1.0	0.622	0.936	0.607	0.911
test_In_In_3.19A.txt	**-15.50**	**47.0**	**-57.0**	**36**	**-0.8**	**-1.0**	**0.619**	**0.935**	**0.600**	**0.912**
test_In_O_3.23A.txt	-15.50	47.0	-57.0	36	-0.8	-1.0	0.611	0.930	0.583	0.902
test_In_O_3.27A.txt	-15.50	47.0	-57.0	36	-0.8	-1.0	0.600	0.923	0.561	0.880
test_In_O_3.31A.txt	-15.50	47.0	-57.0	36	-0.8	-1.0	0.590	0.916	0.538	0.850
test_In_O_3.35A.txt	-15.50	47.0	-57.0	36	-0.8	-1.0	0.582	0.908	0.540	0.814
test_In_O_3.39A.txt	-15.50	47.0	-57.0	36	-0.8	-1.0	0.576	0.908	0.520	0.774

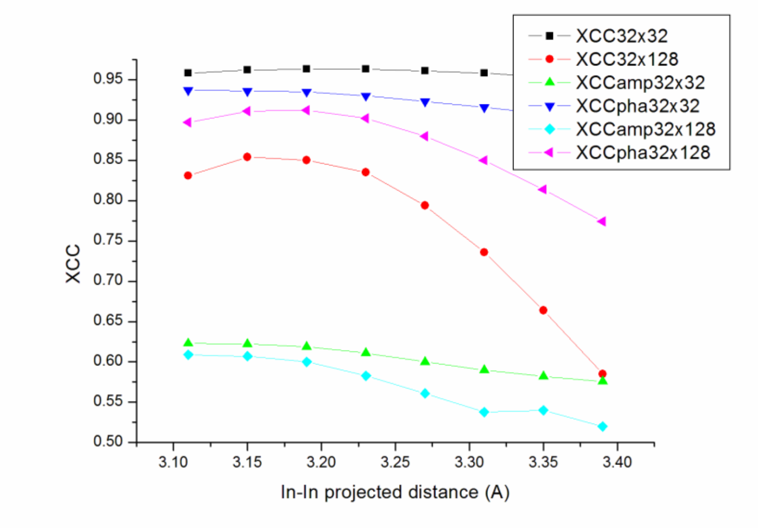

From the structure models with different projected distances of In-In, the XCCs are nearly the same. From the intensity line profiles of the experimental image at the basal IDB in the *m* axis at the bright-contrast defocus condition, the projected distance between In-In is ~ 3.18 Å. Thus, the projected distance between In-In of 3.19 Å is preferred.

⇨ the shortest projected distance between In-In is set to be 3.19 ±0.04 Å.

2. Check the projected distance between In-O along prism planes

Image 15th: thickness 3.4 nm

Name	Rota.	posX	posY	slices	tilt		XCC 40x64	XCC 40x32
test_In_O_0.93A.txt	-15.60	333.0	223(238)	36	-0.5	-1.0	0.901	0.944
test_In_O_1.00A.txt	-15.60	333.0	223(238)	36	-0.5	-1.0	0.905	0.949
test_In_O_1.07A.txt	-15.60	333.0	223(238)	36	-0.5	-1.0	0.907	0.951
test_In_O_1.11A.txt	**-15.60**	**333.0**	**223(238)**	**36**	**-0.5**	**-1.0**	**0.907**	**0.951**
test_In_O_1.14A.txt	-15.60	333.0	223(238)	36	-0.5	-1.0	0.906	0.950
test_In_O_1.19A.txt	-15.60	333.0	223(238)	36	-0.5	-1.0	0.903	0.947
test_In_O_1.21A.txt	-15.60	333.0	223(238)	36	-0.5	-1.0	0.901	0.946
test_In_O_1.28A.txt	-15.60	333.0	223(238)	36	-0.5	-1.0	0.893	0.938
test_In_O_1.35A.txt	-15.60	333.0	223(238)	36	-0.5	-1.0	0.883	0.928
test_In_O_1.42A.txt	-15.60	333.0	223(238)	36	-0.5	-1.0	0.846	0.894

Wave: absorption 0.050, Zero beam Attenuation 0.120, free propagation -0.10 nm

Name	Rota.	posX	posY	slices	tilt		XCCa 40x64	XCCp 40x64	XCCa 40x32	XCCp 40x32
test_In_O_0.93A.txt	-15.50	47.0	-73	36	-0.8	-1.0	0.734	0.931	0.794	0.948
test_In_O_1.00A.txt	-15.50	47.0	-73	36	-0.8	-1.0	0.725	0.928	0.780	0.944
test_In_O_1.07A.txt	-15.50	47.0	-73	36	-0.8	-1.0	0.703	0.923	0.765	0.937
test_In_O_1.11A.txt	**-15.50**	**47.0**	**-73**	**36**	**-0.8**	**-1.0**	**0.693**	**0.919**	**0.755**	**0.933**
test_In_O_1.14A.txt	-15.50	47.0	-73	36	-0.8	-1.0	0.683	0.916	0.745	0.929
test_In_O_1.19A.txt	-15.50	47.0	-73	36	-0.8	-1.0	0.665	0.910	0.727	0.921
test_In_O_1.21A.txt	-15.50	47.0	-72	36	-0.8	-1.0	0.657	0.907	0.719	0.918
test_In_O_1.28A.txt	-15.50	47.0	-72	36	-0.8	-1.0	0.631	0.897	0.693	0.906
test_In_O_1.35A.txt	-15.50	47.0	-73	36	-0.8	-1.0	0.607	0.887	0.667	0.893
test_In_O_1.42A.txt	-15.50	47.0	-73	36	-0.8	-1.0	0.642	0.912	0.687	0.912

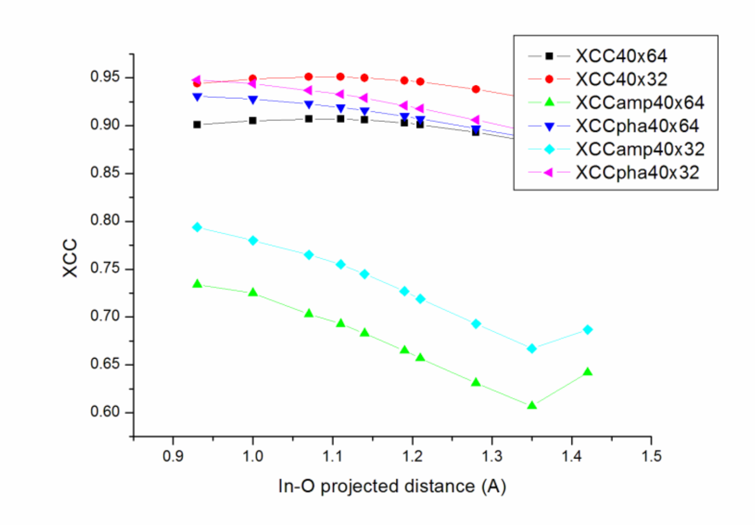

⇨ projected distance between In-O is set to be 1.11 ±0.1 Å.

3. Check the projected distance between In-Zn along the prism planes

---

Image 15th: thickness 3.4 nm

name	Rota.	posX	posY	slices	tilt		XCC (90x64)	XCC (90x32)
testN_In_Zn_2.92A.txt	-15.6	333.5	223(238)	36	-0.5	-1.0	0.897	0.908
testN_In_Zn_2.97A.txt	-15.6	333.5	223(238)	36	-0.5	-1.0	0.905	0.916
testN_In_Zn_3.02A.txt	**-15.6**	**333.5**	**223(238)**	**36**	**-0.5**	**-1.0**	**0.907**	**0.918**
testN_In_Zn_3.09A.txt	-15.6	333.5	223(238)	36	-0.5	-1.0	0.897	0.910
testN_In_Zn_3.12A.txt	-15.6	333.5	223(238)	36	-0.5	-1.0	0.888	0.902
testN_In_Zn_3.22A.txt	-15.6	333.5	223(238)	36	-0.5	-1.0	0.843	0.861
testN_In_Zn_3.32A.txt	-15.6	333.5	223(238)	36	-0.5	-1.0	0.777	0.799

Wave: absorption 0.050, Zero beam Attenuation 0.120, free propagation -0.10 nm.

name	Rota.	pos X	posY	slices	tilt		XCCa 90x64	XCCp 90x64	XCCa 90x32	XCCp 90x32
testN_In_Zn_2.92A.txt	-15.5	47	-57(-72)	36	-0.8	-1.0	0.453	0.894	0.458	0.902
testN_In_Zn_2.97A.txt	-15.5	47	-57(-72)	36	-0.8	-1.0	0.456	0.904	0.464	0.911
testN_In_Zn_3.02A.txt	**-15.5**	**47**	**-57(-72)**	**36**	**-0.8**	**-1.0**	**0.457**	**0.906**	**0.468**	**0.915**
testN_In_Zn_3.09A.txt	-15.5	47	-57(-72)	36	-0.8	-1.0	0.452	0.900	0.468	0.909
testN_In_Zn_3.12A.txt	-15.5	47	-57(-72)	36	-0.8	-1.0	0.447	0.893	0.465	0.903
testN_In_Zn_3.22A.txt	-15.5	47	-57(-72)	36	-0.8	-1.0	0.426	0.856	0.447	0.869
testN_In_Zn_3.32A.txt	-15.5	47	-57(-72)	36	-0.8	-1.0	0.396	0.803	0.485	0.815

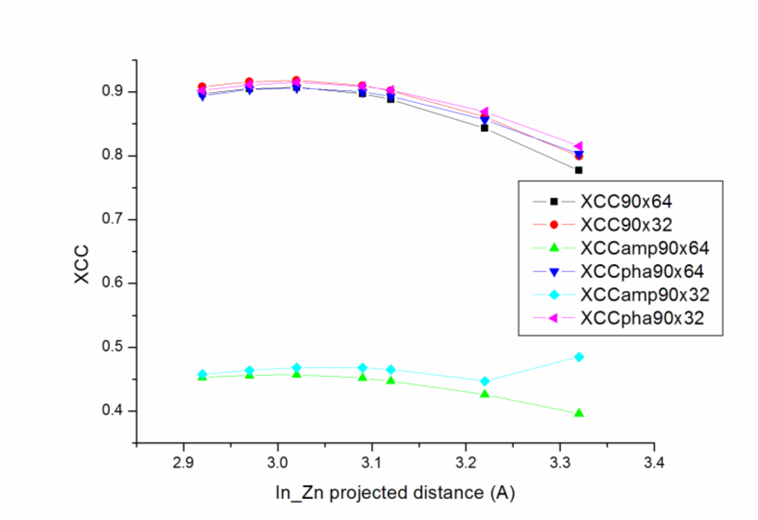

⇨ The projected distance between In-Zn is set to be 3.02 ±0.1 Å.

4. Check the projected distance between Zn-Zn along the prism planes

Image 15th

name	Rota.	posX	posY	slices	tilt		XCC 140x64	XCC 180x64	XCC 140x32	XCC 180x32
testN_Zn_Zn_2.52A.txt	-15.6	333.5	239	36	-0.8	-1.0	0.882	0.850	0.900	0.850
testN_Zn_Zn_2.58A.txt	-15.6	333.5	239	36	-0.8	-1.0	0.894	0.881	0.910	0.885
testN_Zn_Zn_2.62A.txt	-15.6	333.5	239	36	-0.8	-1.0	0.899	0.890	0.914	0.898
testN_Zn_Zn_2.64A.txt	**-15.6**	**333.5**	**239**	**36**	**-0.8**	**-1.0**	**0.900**	**0.895**	**0.915**	**0.902**
testN_Zn_Zn_2.67A.txt	-15.6	333.5	238	36	-0.8	-1.0	0.901	0.896	0.915	0.902
testN_Zn_Zn_2.72A.txt	-15.6	333.5	239	36	-0.8	-1.0	0.898	0.887	0.912	0.892

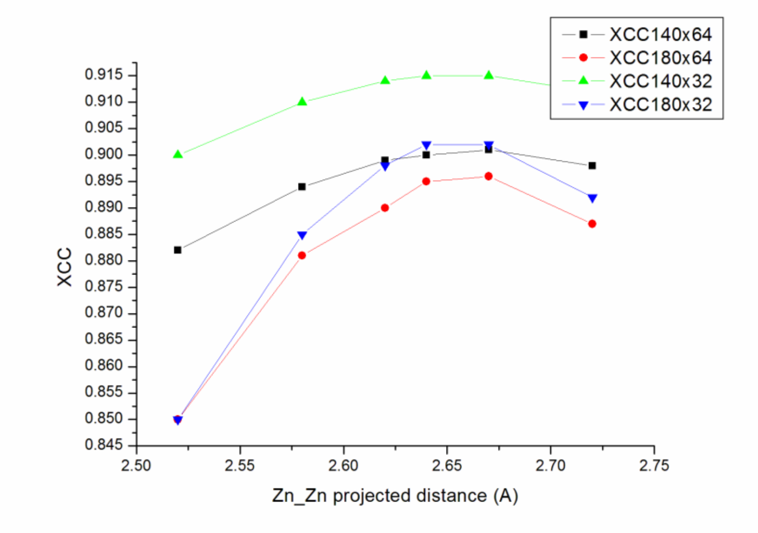

Wave: absorption 0.050, Zero beam attenuation 0.150, free propagation -0.10 nm

name	Rota.	posX	posY	slices	tilt		XCCa 140x64	XCCp 140x64	XCCa 180x64	XCCp 180x64
testN_Zn_Zn_2.52A.txt	-15.5	47	-58	36	-0.5	-1.0	0.442	0.879	0.402	0.862
testN_Zn_Zn_2.58A.txt	-15.5	47	-58	36	-0.5	-1.0	0.448	0.893	0.410	0.890
testN_Zn_Zn_2.62A.txt	-15.5	47	-58	36	-0.5	-1.0	0.451	0.899	0.415	0.900
testN_Zn_Zn_2.64A.txt	**-15.5**	**47**	**-59**	**36**	**-0.5**	**-1.0**	**0.452**	**0.902**	**0.418**	**0.902**
testN_Zn_Zn_2.67A.txt	-15.5	47	-58	36	-0.5	-1.0	0.453	0.903	0.417	0.901
testN_Zn_Zn_2.72A.txt	-15.5	47	-58	36	-0.5	-1.0	0.450	0.903	0.408	0.891

name	Rota.	posX	posY	slices	tilt		XCCa 140x32	XCCp 140x32	XCCa 180x32	XCCp 180x32
testN_Zn_Zn_2.52A.txt	-15.5	47	-73	36	-0.5	-1.0	0.497	0.884	0.448	0.866
testN_Zn_Zn_2.58A.txt	-15.5	47	-73	36	-0.5	-1.0	0.510	0.897	0.460	0.892
testN_Zn_Zn_2.62A.txt	-15.5	47	-73	36	-0.5	-1.0	0.514	0.903	0.464	0.900
testN_Zn_Zn_2.64A.txt	**-15.5**	**47**	**-73**	**36**	**-0.5**	**-1.0**	**0.515**	**0.905**	**0.463**	**0.901**
testN_Zn_Zn_2.67A.txt	-15.5	47	-73	36	-0.5	-1.0	0.517	0.906	0.469	0.900
testN_Zn_Zn_2.72A.txt	-15.5	47	-73	36	-0.5	-1.0	0.513	0.905	0.457	0.888

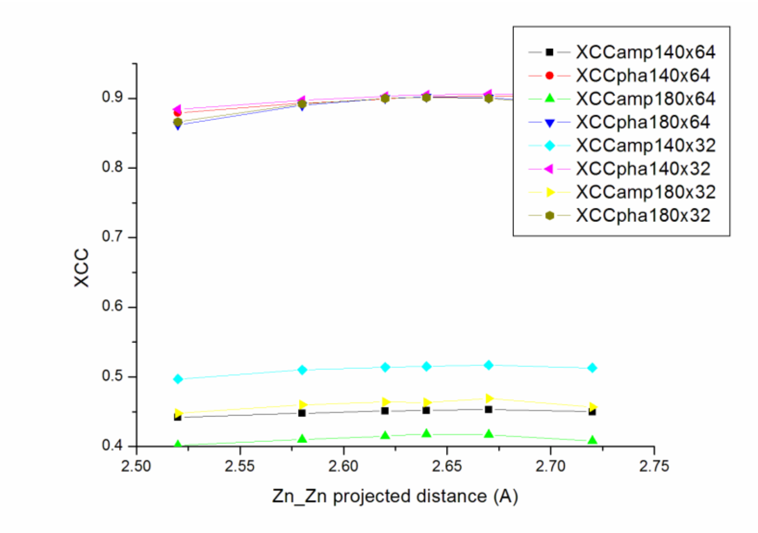

⇨ The projected distance between Zn-Zn is set to be 2.64 ± 0.05 Å.

The refined projected distances in the *m* axis are:

2*$d_{In\text{-}In}$ = **3.19 ± 0.04 Å**,
$d_{In\text{-}O}$ = **1.11 ± 0.10 Å**,
$d_{In\text{-}Zn}$ **= 3.02 ± 0.05 Å**,
$d_{Zn\text{-}Zn}$ **= 2.64 ± 0.05 Å**.

Appendix F

Difference of the simulated images from the Phase plate (PP) approximation and the Full Non-linear (FNL) approximation

Through-focal series images in the *m* axis were used to check the simulation results by using different image simulation approximations: e.g. phase plate (PP) and Full Non-linear (FNL) approximation. Finally, the focal series images are used for comparison of the simulation difference between the PP approximation and FNL calculation.

The sample parameters are: slices 36 (3.4 nm), x_tilt = -0.5°, y_tilt = -1°, C_s = -0.0127 mm, focal spread = 4.00 nm, convergence angle = 0.20 mrad, pixel size = 0.01024 nm/pixel, supercell size = 140x64, image rotation = -15.50°, resize 140×64.

Image	Defocus (nm)	Pos.x (px)	Pos.y (px)	XCC (PP)	XCC (FNL)
1	18.4	358	187	0.901	0.906
2	17.5	360	195	0.920	0.923
3	16.6	355	221	0.916	0.918
4	15.7	351	217	0.915	0.917
5	14.9	345	216	0.904	0.910
6	14.0	344	214	0.909	0.920
7	13.10	341	209	0.887	0.892
8	12.20	342	210	0.863	0.873
9	11.30	344	208	0.835	0.847
10	10.40	347	225	0.821	0.841
11	9.50	347	266	0.847	0.864
12	8.60	345	226	0.862	0.875
13	7.70	340	225	0.833	0.847
14	6.80	337	221	0.856	0.862
15	5.90	333	222	0.892	0.904
16	5.00	334	222	0.883	0.897
17	4.10	336	232	0.870	0.869
18	3.20	333	230	0.844	0.845
19	2.30	335	230	0.848	0.856
20	1.40	335	231	0.794	0.765
21	0.50	333	232	0.499	0.558
22	-0.60	334	229	0.628	0.562
23	-3.30	330	223	0.570	0.558
24	-4.30	333	214	0.626	0.627
25	-5.30	335	211	0.789	0.795
26	-6.40	329	213	0.834	0.837
27	-7.30	329	208	0.897	0.896
28	-8.20	324	205	0.921	0.919
29	-9.10	322	202	0.944	0.941
30	-10.00	316	195	0.951	0.953
sum				**25.059**	**25.177**

Only small difference in the simulated images was found between both approximations.

Appendix G

Image simulations at the pyramidal IDB by the structure models with different In distributions.

HR phase images in the *m* axis were simulated by using different atomic structure models with different In distributions:

1. 100% of In;
2. 10%, 20%, 40%, 20% and 10% of In over 5 atom columns;
3. 25%, 50% and 25% of In over 3 atom columns;

4. 33.3% of In over 3 atom columns.

They were then compared with the experimental focal series images.

The sample parameters are: slices 48 (4.5 nm), x_tilt = 0.2 °, y_tilt = -1 °, C_s = -0.0127 mm, focal spread = 4.00 nm, convergence angle=0.20 mrad, pixel size = 0.01024 nm/pixel, super-cell size = 128×128, image rotation = -16.20 °.

Image	Defocus (nm)	Position x (px)	Position y (px)	XCC (0.1.0)	XCC (1.2.4.2.1)	XCC (2.5-5-2.5)	XCC (3.3.3)
1	18.4	-107	-8.5	0.856	0.860	0.859	0.860
2	17.5	-106	-15.5	0.896	0.901	0.900	0.901
3	16.6	-110	-34.5	0.858	0.865	0.864	0.865
4	15.7	-116	-37.5	0.861	0.866	0.865	0.866
5	14.9	-119	-39.5	0.841	0.846	0.845	0.845
6	14.0	-121	-43.5	0.773	0.781	0.780	0.780
7	13.10	-123	-43.5	0.781	0.784	0.784	0.783
8	12.20	-123	-40.5	0.793	0.797	0.796	0.796
9	11.30	-121	-44.5	0.805	0.806	0.806	0.805
10	10.40	-118	-44.5	0.846	0.848	0.848	0.848
11	9.50	-118	-44.5	0.805	0.808	0.807	0.807
12	8.60	-119	-42.5	0.882	0.883	0.882	0.882
13	7.70	-122.5	-44.5	0.875	0.876	0.875	0.875
14	6.80	-126	-45.5	0.866	0.867	0.866	0.866
15	5.90	-130	-47.5	0.855	0.856	0.855	0.855
16	5.00	-128	-48.5	0.816	0.817	0.816	0.816
17	4.10	-127	-51.5	0.776	0.776	0.776	0.775
18	3.20	-129	-54.5	0.778	0.780	0.780	0.780
19	2.30	-130	-55.5	0.674	0.686	0.685	0.685
20	1.40	-128	-55.5	0.507	0.532	0.528	0.533
21	0.50	-131	-53.5	0.490	0.540	0.533	0.543
22	-0.60	-105	-55.5	0.543	0.582	0.577	0.583
23	-3.30	-107	-51.5	0.676	0.684	0.683	0.684
24	-4.30	-106	-52.5	0.689	0.693	0.693	0.693
25	-5.30	-105	-55.5	0.740	0.744	0.743	0.743
26	-6.40	-109	-59.5	0.789	0.793	0.793	0.792
27	-7.30	-109	-60.5	0.823	0.829	0.828	0.829
28	-8.20	-115	-66.5	0.848	0.854	0.853	0.853
29	-9.10	-116	-73.5	0.883	0.889	0.888	0.888
30	-10.00	-121.5	-79.5	0.907	0.913	0.911	0.911
sum				**23.532**	**23.756**	**23.719**	**23.742**

From the simulations, the structure model of only one atom column of In at the pyramidal IDB results in the lowest XCCs compared to those with other structure models. The structure model with an Indium distribution over 5 atom columns (10%, 20%, 40%, 20% and 10%) are of the highest XCCs. However, the difference among the structure models with different Indium distributions is quite similar, which means that it is insufficient to completely determine the atomic structure at the pyramidal IDBs simply from the HR phase contrast electron microscopy.

Acknowledgement

At the moment of my graduation, I would like to give many thanks to all those people who support and help me with the accomplishment of my education and this PhD thesis in Rheinischen Friedrich-Wilheims-Universität Bonn.

First of all, my deepest thanks to Prof. Dr. W. Mader, as supervisor and mentor, who offers me the opportunity to study and finish projects in his work group of Institute of Inorganic Chemistry. I sincerely appreciate him for the direct and indirect guidance, encouragement and patience throughout my work, especially for insightful and innovative discussions.

Special thanks go to Prof. K. Maier, as my second supervisor, for his kindness and recommendation and advice of getting in touch with TEM for the material analysis.

Thanks to the BIPP (Bonn International Physics Program) and BIGS (Bonn International Graduate School) for offering me the opportunity of studying diplom in physics, and especially to Dr. D. Thrun and Mrs. P. Weiss for helping me with studying and living in Bonn for my first year (2004) in Germany.

I would like to show my gratitude to Mr. Jürgen Simon for his guidance and explanation of TEM and the related TEM specimen preparation at the beginning of my work and to Mr. Matthias Svete for the discussions on BF-TEM imaging and image simulations.

Special thanks to Dr. L. Houben, Dr. K. Tillmann and Dr. M. Luysberg at the Ernst Ruska-Centre of Forschungszentrum Jülich for the help of operating FEI TITAN80-300 electron microscopes and to Dr. C. Jia and Dr. S. Mi for sharing their knowledge of materials.

Special thanks to Dr. C. Koch for sharing his wisdom on HAADF imaging and image simulations, especially his kindness for providing me with self-made ‘qSTEM’ source code for HAADF image simulations. Thanks to Prof. A. Rosenauer and Dr. M. Schowalter for sharing the ‘DALI’ algorithm, which can be used for the displacement and the strain measurement directly from atomically resolved TEM images.

Many thanks to Dr. H. Schmidt, Dr. K. Kelm, Dr. E. Pesch, Dr. T. Walther and all the other colleagues and former colleagues for their valuable and invaluable comments and for the harmonious atmosphere during work.

I am appreciated for the friendship of Dr. H. Cui, Dr. K. Sun, Dr. Z. Jian, Mr. X. Cao and all my Chinese friends and special thanks to Dr. M. Miller and Mrs. N. Chen for taking care of me at times.

At last, special thanks to my family for their understandings and selfless concerns, which encourage me greatly for my studying and living alone in Germany for nearly six years.

Bonn, July 2009

Curriculum Vitae

Personal information

Name: Yu, Wentao
Citizenship: Chinese
Date of Birth: 27-Sep-1980, Hangzhou (P. R. China)
Email: wentaoyu@msn.com

Education

9/2004 – now: Institute of Inorganic Chemistry, Rheinischen Friedrich-Wilhelms-Universität, Bonn, Germany

- Ph.D. Candidate, Physics (inorganic materials research)
- Thesis: Atomic resolution studies of In_2O_3–ZnO compounds on *aberration*-corrected electron microscopes
- Supervisor: Prof. Dr. Werner Mader
  Prof. Dr. K. Maier

9/2003 – 9/2004: Bonn International Physics Program (BIPP), Rheinischen Friedrich-Wilhelms-Universität, Bonn, Germany

- Diplom equivalent, physics

9/1999 – 7/2003: Institute of Astrophysics, School of Physics, Peking University, Beijing, P. R. China

- B.S., Astrophysics
- GPA: A(85-100)

9/1996 – 7/1999: Hangzhou No.2 Middle school, Hangzhou, P.R. China

- High School Certificate Examination (equivalent to A levels): 4/4
- Enrolled by Peking University (P. R. China) without taking the National College Entrance Examination (NCEE)